UNIVERSITY OF ALBERTA

# Exploring Design and Detection Issues for Automated Multichannel Microfluidic Immunoassay System

By

**Siew Bang Cheng**

A thesis submitted to
The Faculty of Graduate Studies and Research
in partial fulfillment of the requirements for the degree of

**Doctor of Philosophy**

**Department of Chemistry**

Edmonton, Alberta
Spring, 2001

National Library of Canada
Acquisitions and Bibliographic Services
395 Wellington Street
Ottawa ON K1A 0N4
Canada

Bibliothèque nationale du Canada
Acquisitions et services bibliographiques
395, rue Wellington
Ottawa ON K1A 0N4
Canada

*Your file Votre référence*

*Our file Notre référence*

The author has granted a non-exclusive licence allowing the National Library of Canada to reproduce, loan, distribute or sell copies of this thesis in microform, paper or electronic formats.

The author retains ownership of the copyright in this thesis. Neither the thesis nor substantial extracts from it may be printed or otherwise reproduced without the author's permission.

L'auteur a accordé une licence non exclusive permettant à la Bibliothèque nationale du Canada de reproduire, prêter, distribuer ou vendre des copies de cette thèse sous la forme de microfiche/film, de reproduction sur papier ou sur format électronique.

L'auteur conserve la propriété du droit d'auteur qui protège cette thèse. Ni la thèse ni des extraits substantiels de celle-ci ne doivent être imprimés ou autrement reproduits sans son autorisation.

0-612-60283-4

Canada

UNIVERSITY OF ALBERTA

LIBRARY RELEASE FORM

**Name of Author:** Siew Bang Cheng

**Title of Thesis:** Exploring Design and Detection Issues for Automated Multichannel Microfluidic Immunoassay System

**Degree:** Doctor of Philosophy

**Year this Degree Granted:** 2001

Permission is hereby granted to the University of Alberta Library to reproduce single copies of this thesis and to lend or sell such copies for private, scholarly or scientific research purposes only.

The author reserves all other publication and other rights in association with the copyright in the thesis, and except as herein before provided, neither the thesis nor any substantial portion thereof may be printed or otherwise reproduced in any material form whatever without the author's prior written permission

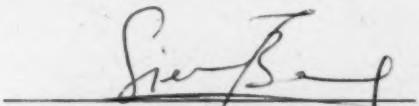

1006 VH Michener Park
Edmonton, Alberta
Canada T6H 4N1

April 17, 2001

UNIVERSITY OF ALBERTA

FACULTY OF GRADUATE STUDIES AND RESEARCH

The undersigned certify that they have read, and recommend to the Faculty of Graduate Studies and Research for acceptance, a thesis entitled **Exploring Design and Detection Issues for Automated Multichannel Microfluidic Immunoassay System** submitted by **Siew Bang Cheng** in partial fulfillment of the requirements for the degree of **Doctor of Philosophy**.

Supervisor:

Dr. D. Jed Harrison

Dr. Frederick F. Cantwell

Dr. Mark T. McDermott

Dr. Arthur Mar

Dr. James N. McMullin

External Examiner:

Dr. Fred K. Forster

Apr. 17, 2001

*Dedicated to*

*my parents*
*Seng Lee Cheng & Gim Gim Khoo*

*my brother*
*Yee Siau Cheng*

*and*

*my husband*
*Jey Arul*

*for their unconditional love and support*

# Abstract

The development of miniaturized, microfabricated devices for chemical and biochemical analysis is a new and exciting application of micromachining technology. The ultimate goal of such micro systems is an automated, portable, and high throughput instrument capable of performing analysis on a routine basis. High throughput microfluidic devices have practical issues such as device layout and detector design. A microfluidic device with integrated waveguides was fabricated and evaluated. The basic ion exchange waveguides were demonstrated to couple laser light to a fluidic channel and excite the sample. The amount of light coupled into the detection cell afforded a detection limit of ~10 nM for standard Cy-5 dye. A high throughput microfluidic chip inevitably will require corners or serpentine channels to be introduced in the long separation channels in order to increase the device density per chip. A simple model based on Taylor dispersion was proposed and evaluated. The model predicted corner induced band broadening of 0.04, 0.09 and 15 μm/corner compared to experimental value of 0.03, 0.07 and 16 μm/corner respectively for different devices and samples. A six-channel microfluidic immunoassay device with a scanned fluorescence detection system was developed. A detection limit of 30 pM was obtained for fluorescein with a galvano-scanning detector, using a 7.1 Hz sampling rate for each of the separation channels (57 Hz overall sampling rate for 6 channels). Simultaneous direct immunoassays for ovalbumin and for anti-estradiol were performed within the multichannel device. Mixing, reaction, and separation could be achieved within 60 s. Simultaneous calibration and analysis could be achieved within 2 min. Careful chip conditioning resulted in peak height RSD values of 3-8 % (n = 5 or 6). Various serial dilution devices were designed and evaluated. Geometry was used to control the dilution factor, as each device was designed to use only one power supply. A dilution factor up to 900 was achieved with 11 % deviation from the nominal value and 4 % RSD (n = 3). SPICE lumped element and sheet resistance models and FlumeCAD finite element simulations were utilized to understand the flow behaviour within the diluters.

# Acknowledgements

I am extremely grateful for many people who have helped me during my studies at University of Alberta. The multidisciplinary nature of this work allowed me to work with many people and the valuable lessons learned are greatly appreciated.

I extend special gratitude to my boss and research advisor, Prof. D. Jed Harrison, for introducing me to this exciting and challenging field. His guidance, tolerance, and support throughout the course of this research were the main reason for the success of the work. Sincere thanks go to Cameron Skinner, a former postdoc in Harrison's group, who helped me tremendously with the work described in Chapter 4, taught me valuable instrumentation techniques and provided crucial advice for the work described in Chapter 5. My thanks also extend to former and current Prof. Harrison's group members, especially Arlene Figley, Justine Taylor, Per Anderson, Paul Li, Christa Coyler, Christie McDermott, Karl Fluri and Nghia Chiem for their professional and personal advice.

I wish to express my appreciation for Dr. Fred Cantwell, Dr. Mark McDermott, Dr. Arthur Mar, Dr. Jim McMullin and Dr. Fred Forster for being on my examining committee.

My appreciation is also extended to all the technical support stuff at the chemistry department: Ed Feschuk, Al Chilton and Kim Nguy Do at the electronic shop, Gerald Streefkerk and John Toonen at the glass shop, Hubert Hofmann, Roman Lipiecki, Paul Crothers, Kevin Rolston, Henry Stolk, Stan Luxa, Dieter Starke and Randy Benson at the machine shop for their high quality items. In addition, I would like to thank Paul Wagner and Lang Shi at the Electron Microprobe Laboratory and George Braybrook at the Scanning Electron Microscope Laboratory for performing the Energy Dispersive X-ray Analysis and Backscattered Electron Imaging shown in Chapter 2. I'm grateful to Graham McKinnon, Glen Fitzpatrick, Jim Broughton and Yuebin Ning at Micralyne (formerly Alberta Microelectronic Corporation, AMC) for their cooperation in various projects and the use of their facilities. Lianne Lester (AMC) and Fahima Ouchen are acknowledged for micromachining training and device fabrication.

Thanks are also extended to Bill Lee at Defence Research Establishment at Suffield (DRES) and Murray Paulson at Dycor for their collaborative effort in the multichannel work described in Chapter 4.

I acknowledge the National Science and Engineering Research Council of Canada (NSERC), DRES and Defense Advanced Research Projects Agency (Microflume) for financial support of the studies presented in this thesis. I would also like to thank Micralyne for a one-year graduate studentship, Graduate Student Association for a travel award and financial assistance to foreign student and the Department of Chemistry for financial support.

I am greatly indebted to my parents and brother for their constant support and confidence in my ability. I also thank my brother for enhancing my knowledge of the "outside world" through his camera lenses and travel diary. Lastly, I appreciate Jey's support through the good and the bad times.

# Table of Contents


**Chapter 1: Introduction**

**1.1. Historical Development of Miniaturized Total Analysis System** **1**
1.1.1. Total Analysis System 1
1.1.2. Miniaturized Total Analysis System 1
**1.2. Motivation of this work** **2**
**1.3. Introduction to Affinity Capillary Electrophoresis based Immunoassay** **3**
1.3.1. Capillary Electrophoresis 3
*1.3.1.1. Pumping and Separation Mechanism* *4*
1.3.2. Affinity Capillary Electrophoresis 5
1.3.3. CE based Immunoassay 6
**1.4. Towards Automation of μTAS** **6**
1.4.1. Multiplexing 6
1.4.2. Building Blocks for μTAS 7
**1.5. Introduction to Waveguides** **8**
1.5.1. Thermal Ion Exchange Waveguide 10
*1.5.1.1. Driving Mechanism* *10*
*1.5.1.2. Characterization Technique* *11*
1.5.1.2.1. Effective Refractive Index by Prism Coupling Technique 12
**1.6. Scope of This Thesis** **14**
**1.7. References** **15**

**Chapter 2: Integrating Ion Exchange Waveguides onto Microfluidic Chips**

**2.1. Introduction** **19**
**2.2. Experimental Section** **20**
2.2.1. Materials and Reagents 20
2.2.2. Fabrication Procedure 21
*2.2.2.1. Waveguide Fabrication* *21*
*2.2.2.2. Device Fabrication* *21*
2.2.3. Waveguide Characterization Methods 22
2.2.4. Instrumentation 23
**2.3. Results and Discussion** **23**
2.3.1. Addressing Device and Waveguide Fabrication Issues 23
*2.3.1.1. Longevity of Metal Masks* *23*
*2.3.1.2. Swollen Waveguide* *24*
*2.3.1.3. Ion Exchange Duration Optimization* *25*
*2.3.1.4. Device Bonding* *28*
*2.3.1.5. Waveguide Layout* *28*
*2.3.1.6. Final Device Layout* *29*
2.3.2. Device Evaluation 29
2.3.2.1. Fluorescence Detection 30
2.3.2.2. Waveguide Losses 31
**2.4. Conclusion** **32**
**2.5. References** **33**

**Chapter 3: Analysis of Dispersion Caused by Corners in glass-based Microchip Capillary Electrophoresis System**

**3.1. Introduction** 35
**3.2. Theory and Simulation** 36
3.2.1. Taylor Dispersion in a Corner 37
3.2.2. Finite Element Simulation 39
**3.3. Experimental Section** 43
**3.4. Results and Discussion** 44
**3.5. Conclusion** 48
**3.6. References** 48

**Chapter 4: Development of a Multi-channel Microfluidic Analysis System Employing Affinity Capillary Electrophoresis for Immunoassay**

**4.1. Introduction** 50
**4.2. Experimental Section** 51
4.2.1. Device Design 51
4.2.2. Materials and Reagents 53
4.2.3. Detection and Control System 53
4.2.4. Operating Procedure 55
**4.3. Results and Discussion** 57
4.3.1. Detector Design 57
4.3.2. Multi-channel Layout 59
4.3.3. Electrical Interface 61
4.3.4. Qualitative Analysis 63
4.3.5. Factors Required for Uniform Analytical Behaviour 65
4.3.6. Quantitative Analysis 69
**4.4. Conclusion** 73
**4.5. References** 74

**Chapter 5: Design and Evaluation of Serial Dilution Component for Microfluidic Devices**

**5.1. Introduction** 76
**5.2. Theory of multi-step dilution** 76
**5.3. Experimental Section** 79
**5.4. Results and Discussion** 82
5.4.1. D32 Device Evaluation with Relative Method 84
5.4.2. SPICE Modeling and Simulation 86
5.4.3. Evaluation of Device D1024 with Relative Method 88
5.4.4. Evaluating D1024 with Absolute Method 90
5.4.5. Effects of Different Ionic Strength on Dilution 91
5.4.6. D32S – A Different Method of Reservoir Sharing 93
5.4.7. Preliminary Study of Varying Cross Section to Vary Dilution Factor 97
*5.4.7.1. Device Design* 97
*5.4.7.2. Evaluation of D64* 98
**5.5. Conclusion** 103
**5.6. References** 103

**Chapter 6: Conclusion and Suggestions for Future Work** 104

# List of Tables


| Table | | Page |
|---|---|---|
| 1.1 | Combinations of components integrated into microanalytical systems | 8 |
| 3.1 | Parameters used in FlumeCAD finite element simulation | 40 |
| 3.2 | Experimental parameters for corner experiment | 44 |
| 4.1 | Measured impedance of channel segments within SPIDY | 66 |
| 5.1 | Comparison of average signal obtained for each diluting stage | 85 |
| 5.2 | List of SPIE simulated voltages | 87 |
| 5.3 | List of current flowing through each channel segments of D1024 | 87 |
| 5.4 | List of average dilution factor obtained using D1024 as a 32X diluter | 88 |
| 5.5 | List of samples used in the test of ionic strength on dilution | 92 |
| 5.6 | AFU ratios for device D64 | 102 |
| 5.7 | Comparison of theoretical and experimental dilution factor for D64 | 102 |

# List of Figures


| Figure | | Page |
|---|---|---|
| 1.1 | Simplistic view of electroosmotic flow and electrophoretic migration | 5 |
| 1.2 | Basic structure and refractive index profile of the optical waveguide | 9 |
| 1.3 | Diagram of salt melt and glass interface during thermal ion exchange process | 11 |
| 1.4 | Principle of prism coupling | 12 |
| 1.5 | Experimental setup for measuring coupling angle in a prism coupling method | 13 |
| 2.1 | Device layout showing fluid channels and curve waveguides | 22 |
| 2.2 | Profilometer trace showing the swelling of waveguide due to stress | 24 |
| 2.3 | Plot of waveguide depth and refractive index versus duration of ion exchange | 25 |
| 2.4 | Energy dispersive spectrum of ion exchanged region compared to substrate | 26 |
| 2.5 | Plot of width of waveguide versus duration of ion exchange | 27 |
| 2.6 | Backscattered electron image of a silver ion exchange channel waveguide | 27 |
| 2.7 | Laser induced fluorescence setup | 30 |
| 2.8 | Fluorescence calibration curve for Cy-5 standards | 31 |
| 3.1 | An "L" channel used in the FlumeCAD finite element simulation | 39 |
| 3.2 | FlumeCAD simulation results for small molecule | 41 |
| 3.3 | FlumeCAD simulation results for large molecules | 42 |
| 3.4 | Device with 33 corners used in the study | 43 |
| 3.5 | Image of a typical corner obtained using electron microscopy | 45 |
| 4.1 | The overall layout of the flow channel manifold in SPIDY device | 52 |
| 4.2 | A cartoon of the laser induced fluorescence detection scheme for SPIDY | 54 |
| 4.3 | Illustration of the Labview programmed timing and data acquisition process. | 57 |
| 4.4 | Signal detected from a 100 pM fluorescein sample | 58 |
| 4.5 | Photograph of the PC board electrical interface for SPIDY | 60 |
| 4.6 | Photograph of an acrylic plate electrical interface for SPIDY | 62 |
| 4.7 | Illustration of the simultaneous collection of electrophoregrams from SPIDY using Cy-5 standard dye | 63 |
| 4.8 | Electrophorograms of five consecutive runs of a hydrolyzed bifunctional Cy-5 dye from a single channel | 64 |
| 4.9 | Six electropherograms obtained simultaneously in SPIDY for a qualitative immunoassay of ovalbumin | 65 |
| 4.10 | Comparison of injection performance of reaction cells 2 and 7 in an old SPIDY device | 67 |

| | | |
|---|---|---|
| 4.11 | Comparison of the difference in migration time between reaction cells 2 and 7 | 68 |
| 4.12 | Calibration curves for fluorescein obtained simultaneously in SPIDY | 70 |
| 4.13 | Electrophoregrams of six on-chip mixing, reaction and separation of anti-estradiol assay | 70 |
| 4.14 | Calibration curves for anti-estradiol assay | 71 |
| 4.15 | Six channels electrophoregrams of different anti-estradiol concentration showing on-chip calibration of the assay | 72 |
| 4.16 | Cross-channel calibration curve for anti-estradiol assay | 73 |
| 5.1 | Schematic drawing of a Y mixing intersection | 77 |
| 5.2 | Layout of diluter D32 and D1024 | 80 |
| 5.3 | Layout of diluter D64 | 80 |
| 5.4 | Layout of diluter D32S | 81 |
| 5.5 | A typical "staircase buffer run" performed on D32 | 83 |
| 5.6 | Plot of 1/AFU versus nominal dilution factor for D32 | 84 |
| 5.7 | An SPICE equivalent circuit of D1024 | 87 |
| 5.8 | Plot of AFU versus original fluorescein concentration for various dilution obtained using top half of D1024 | 89 |
| 5.9 | Bar chart comparing the effect of ionic strength on dilution | 92 |
| 5.10 | A sheet resistance circuit used to model device D32S | 94 |
| 5.11 | FlumeCAD simulation result for D32S | 96 |
| 5.12 | Equivalent circuit for diluter D64 with different mixing sequence | 97 |
| 5.13 | Equivalent circuit for the final design of D64 | 99 |
| 5.14 | Plot of diluted fluorescein concentration versus the original concentration | 100 |
| 5.15 | Plot of AFU versus 1/Dilution factor for D64 | 101 |
| 5.16 | Typical "staircase sample run" and "staircase buffer run" performed in D64 | 102 |

# List of Abbreviations

| | |
|---|---|
| Ab | Antibody |
| ACE | Affinity capillary electrophoresis |
| AFU | Arbitrary fluorescence unit |
| Ag | Antigen |
| BSE | Backscattered electron imaging |
| CE | Capillary electrophoresis |
| CEIA | CE based IA |
| DL | Detection limit |
| EDS | Energy dispersive spectrometry |
| EOF | Electroosmotic flow |
| EP | Electrophoretic migration |
| FIA | Flow injection analysis |
| Fl | Fluorescein |
| GND | Ground potential |
| HV | High voltage |
| IA | Immunoassay |
| LIF | Laser induced fluorescence |
| LOD | Limit of detection |
| MEKC | Micellar electrokinetic chromatography |
| PCB | Printed circuit board |
| POD | Point of detection |
| PMT | Photomultiplier tube |
| RIE | Reactive ion etching |
| RSD | Relative standard deviation |
| TAS | Total analysis system |
| μTAS | Miniaturized total analysis system |

# Chapter 1

# Introduction

## 1.1 Historical Development of Miniaturized Total Analysis System

### 1.1.1 Total Analysis System (TAS)

A chemical analysis typically includes several steps: sampling, transfer of samples to laboratory, sample pretreatment such as dilution, preconcentration, interference removal, labeling etc, followed by separation, sample post-treatment such as washing, labeling etc, and then detection and finally data interpretation and result reporting. An automated system with all the necessary steps in an analytical analysis integrated into a single unit would significantly reduce human involvement in this labour intensive process. This translates into a reduction of total analysis time and lower cost per analysis, while increasing reproducibility and accuracy due to less human intervention. Thus the concept of a "Total Chemical Analysis System" (TAS), as suggested and demonstrated by H.M. Widmer and coworkers for a gas phase analysis system,[1-5] was born. TAS for liquid based analysis were subsequently developed by integration of sample preparation procedures into flow injection analysis (FIA) for monitoring glucose in a fermentation process. The main disadvantages of TAS are slow sample transport, poor separation speed, lack of selectivity or separation efficiency and high consumption of reagents and carrier solutions.[6] A further improvement in terms of reducing reagent consumption, waste generation, and analysis time, is the miniaturization of the TAS.

### 1.1.2 Miniaturized Total Analysis System (μTAS)

Terry et al first demonstrated the miniaturization of a chemical analysis instrument using microfabrication technology.[7-8] The significance of his work in integrating a split injector, a GC column and a thermal conductivity detector on a silicon wafer 5 cm in diameter remained undeveloped until the late 1980s when Manz et al realized the advantage of performing liquid chromatography separations on

micromachined devices.[9] Manz suggested the concept of a "Miniaturized Total Chemical Analysis System" (μTAS) in which "a TAS performs all sample handling steps extremely close to the place of measurement".[10] The main reason for his proposed miniaturization of the TAS is related to an enhancement of its analytical performance, rather than a reduction of its size. Miniaturization of flow manifolds to minimize the transport distance between sampling and detection point addresses not only the problems in TAS, but also points to higher separation speed and better resolution of the analytes based on simple diffusion and hydrodynamic theory. Examples of improved performance using smaller capillary inner diameter and shorter capillary length have been shown.[11-13] The pioneering work, from the development of the first TAS to the early research work in μTAS was summarized by H. Michael Widmer at the 2nd International Symposium on Miniaturized Total Analysis Systems in Basel, Switzerland, 1996.[14] Since then, the concept of μTAS has grown to include a wide range of methods integrated into a single device. In addition, the original concept of μTAS as a chemical analysis platform has been expanded to include analysis of biological samples. Interested readers are referred to recent reviews[15-23] in this field as well as the μTAS proceedings, published biannually since 1994.[24-27]

## 1.2 Motivation of this work

This thesis examines methods to multiplex microfluidic devices and processes to gain sample throughput advantages and increases the range of tools available on chip. The specific vehicle used was immunoassay, although the lessons learned should prove to be more general. A number of specific issues had to be addressed in the course of this effort, such as device layout and the effect of corners on separation efficiency. In designing microfluidic optical detection systems, it became apparent that the need to direct light paths in and around the chip adds complexity to their use. This thesis presents an initial attempt at a method to include integrated waveguides as light pipes along with fluidic pipes. Ion-exchange waveguide methods were employed for this purpose. The subsequent sections present background information that should be useful in evaluating the focus of this thesis.

## 1.3 Introduction to Affinity Capillary Electrophoresis based Immunoassay

Electrophoresis[28] is a viable method for the separation of antibody and antigen from the corresponding antibody-antigen complex, since the complex will in general have a different electrophoretic mobility than the free reagents.[29-31] The advantages of performing affinity capillary electrophoresis[32-33] (ACE) based immunoassay[34] (IA) for clinical applications on microfluidic chips are improved analysis speed, high sample throughput and small sample volumes. The high sample throughputs, either in a parallel or sequential way, will possibly circumvent the need of conventional robotics for immunoassays, which is state of the art in clinical laboratories.

### 1.3.1 Capillary Electrophoresis

Capillary electrophoresis (CE) is a separation technique for charged molecules based on their mobility in an applied electric field. In 1930 Tiselius[35-36] introduced an analytical technique based on electrophoresis. His work described the separation of blood plasma proteins, namely albumin from α-, β- and γ-globulin using electrophoresis. This pioneering work was awarded the Nobel Prize in 1948. Paper and gel electrophoresis were introduced later.[37-39] In 1967, Hjertén[40] demonstrated what was called "free zone electrophoresis" in which he performed the electrophoretic separations in a 300 μm glass tube. The potential of this method was not realized until Jorgensen and Lukacs[41] published their work in 1981, which demonstrated the high resolving power of capillary zone electrophoresis. This was followed by the introduction of micellar electrokinetic chromatography (MEKC) for the separation of neutral compounds in 1984 by Terabe et al.[42] The first commercial instrument was marketed in 1988 and since then, many advances and applications have taken place. Many reviews and books present the historical development and recent advancement of capillary electrophoresis,[43-44] to which the interested reader is referred.

Since the early 1990s when Manz and Harrison[45] introduced the concept of μTAS, CE has been the major component of many μTAS devices.[46-47] In addition to being a powerful separation technique, CE offers a much more important "driving force", namely the pumping force known as electroosmosis, for μTAS devices. Electroosmosis

was used as a convenient and simple method to transport analytes within the μTAS devices, offering a valveless way of controlling fluid flow. In addition, these microchip based CE devices have heralded a new area that has become known as planar microfluidics. The planar format of most TAS devices creates unconventional design issues related to the inherent two-dimensionality of these devices. Issues such as packing a long CE column onto a planar device ultimately requires bending of the column to form corners, a subject that will be reviewed in Chapter 3.

#### *1.3.1.1 Pumping and Separation Mechanism*

Typically CE separations are performed in buffer filled capillaries in which a sample is injected as a narrow plug either hydrodynamically via a pressure difference, or electrokinetically via a voltage difference. A conductive path is established when both ends of the capillary are inserted into two buffer vials to which high voltage is applied to one vial with respect to ground at the other vial. The application of electric field through the capillary results in two ion transport phenomena: electroosmotic flow (EOF) and electrophoretic migration (EP). The EOF is usually greater in magnitude than is EP, thus resulting in the ions travelling in the direction of the EOF. The direction of EOF depends on the net charge on the surface of the capillary wall. In an uncoated glass capillary, the wall is typically negatively charged due to $-Si-O^-$ group. With no electric field applied, these wall charges attract cations from the buffer solution that fill the capillary, as illustrated in Figure 1.1. When an electric field is applied, the electrostatic attraction between the cations lining the wall and the wall surface charge is overcome and the cathodic layer moves toward the cathode, dragging the bulk of the fluid in the capillary with it.

Analytes introduced into the electric field will migrate at different speeds, based on their charge to size ratio. Smaller, positively charged species will move toward the cathode, in the direction of the EOF, followed by the larger, positively charged species. The negatively charged species will be attracted toward the anode. However, the usually larger magnitude of EOF versus EP will cause the negatively charged molecules to have an overall net flow in the direction of the EOF, at a speed lower than the EOF. Neutral species will move at the same speed as the EOF, thus appearing at the detector after the

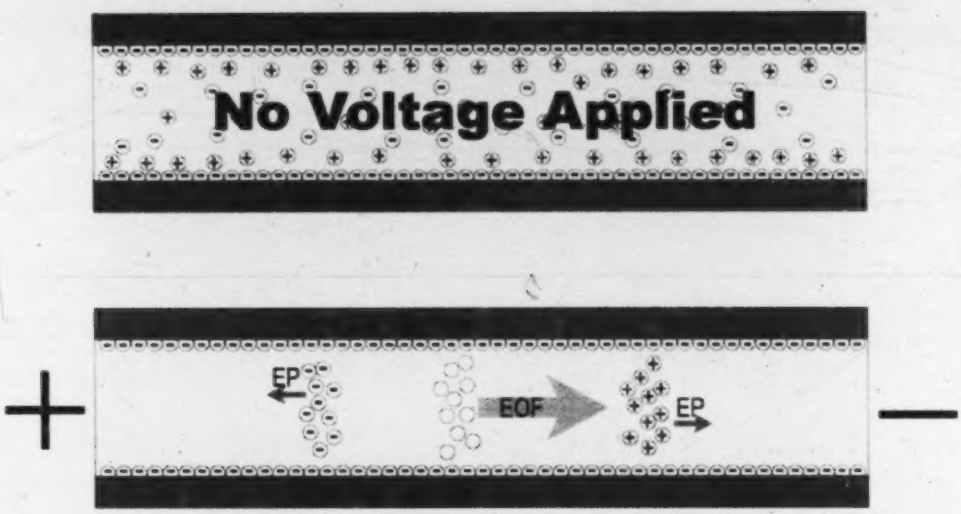


Figure 1.1 Simplistic view of electroosmotic flow (EOF) and electrophoretic migration (EP). The top view shows the negatively charged glass surface and hydrated cations accumulating near the surface. The bottom view shows the solvent flow towards the cathode upon application of electric field and the differential solute migration superimposed on the EOF.

cations and before the anions. The differences in EP for charged analytes forms the basis of CE separation, while the EOF becomes the basis of fluid transport mechanism in microfluidic devices.

### 1.3.2 Affinity Capillary Electrophoresis

Affinity electrophoresis[48] is an analytical approach for the quantitation and identification of specific binding events and of binding constants by recording the migration patterns of interacting molecules in an electric field.[32-33] Many electrophoresis techniques, such as paper, polyacrylamide, starch, and agarose gel electrophoresis, have been used for affinity electrophoresis. The introduction of CE has made it a popular technique for affinity electrophoresis due to its high-resolution separation. In addition, because affinity capillary electrophoresis (ACE) is generally performed in a homogeneous medium without stabilizing agents under more or less physiological conditions, it is well suited for the study of biological interactions. A variety of interactants including detergents, cyclodextrins, crown ethers, antibiotics, peptides, proteins, and formally, all MEKC and chiral separations can be considered to be ACE methods. Recent advances of ACE can be found in references.[32-33, 49] Microchip based

ACE has been demonstrated for a variety of enzyme assay,[50] immunoassay,[51] MEKC[52] and chiral separations.[53]

### 1.3.3 CE based Immunoassay

Immunoassay (IA) has become a popular method for a number of clinical, pharmaceutical, and chemical analyses due to its ability to quantitate minute amounts of analyte in complex mixture of potential interferences at high concentrations.[34, 54-57] The high selectivity of IA is achieved by the use of antibodies with high discriminatory power and binding affinity for the analyte of interest. The primary drawback of common IA formats is the slow and manually or robotically intensive procedure, typically taking several hours to complete. When high throughput is necessary, a rapid and automated system is preferred. CE based IA (CEIA) was introduced as a method to achieve this goal.[58-59] The initial work in CEIA proved to have little speed improvement, as CE was merely used at the end of an IA as a separation method. Further improvement was made by performing IA in homogeneous solution phase using the ACE format first demonstrated by Grossman in 1989.[60] The first microchip based CEIA was presented at Tranducers '95 by Harrison et al[61] in which BSA and anti-BSA were mixed and reacted off-chip and then the complex was separated from the reagents within a microfluidic chip. Koutny et al[62] later demonstrated IA for cortisol in serum in which the IA was performed in a small vial and a microchip based CE was used to separate the free labeled antigen from the antigen-antibody complex. Chiem and Harrison[51] reported the first microchip based competitive CEIA using ACE format for theophylline in human serum. In this work the IA reagents were mixed, reacted and the products separated on a microchip. Their work demonstrated a tremendous increase in analysis speed over the conventional format. In addition, the integration of several analysis steps into a single device represented a major step towards a true μTAS.

## 1.4 Towards Automation of μTAS

### 1.4.1 Multiplexing

In the context of this study, multiplexing is defined as the performance of multiple chemical/biochemical analyses simultaneously on a single microchip based device, along

with the issues related to achieving this goal. Utilizing multiplexing in an automated μTAS has been envisioned since the beginning.[9] Multiplexing increases analysis throughput, and with automation can reduce the cost per analysis. The first working example was demonstrated by Mathies and coworkers for DNA separation in 12 parallel capillary electrophoresis channels.[63] The detection method was based on a single point detector with a moving translation stage that his research group had previously developed for capillary array electrophoresis.[64] In 1999 they reported a 96-channel separation microchip which can be coupled to a 96-well microplate, thus moving towards automation.[65] The 96-channel design used a radial translation technique to scan all channels, as opposed to the rectilinear method in previous studies.[63] This design allows all separation channels to be laid out without corners, thus reducing the band broadening due to the corners. The corner-induced band broadening effect will be reviewed in Chapter 3. In the same year, Landers[66] suggested an alternative detection scheme for a multichannel electrophoretic microchip. In his work, a laser beam scanning system driven by an acousto-optical deflector was demonstrated. Frequency dependent acoustic waves are used to deflect the laser beam in order to scan a multichannel device. The system provided high scanning speed and had no moving parts, which could offer a big advantage for a portable system. Another multichannel detection scheme based on a diffractive optical element known as a Dammann grating with microfabricated microlenses has also been suggested.[67] All of the currently reported detection systems for multichannel have been based on laser induced fluorescence (LIF), as it is the most common detection method used in microchip based devices.

### 1.4.2 Building blocks for μTAS

The main concept of TAS and μTAS was to integrate all the time consuming and labour intensive sample preparation/processing steps in the vicinity of where detection occurs (note that Manz[9] considered separation as a special sample processing step). There has been much research in the area of integrating sample processing steps other than the injection and separation as first demonstrated in 1992.[45] Some of the sample manipulation components include a mixer, valves, cell sorters, immobilization reactors, coulter particle sizers, dialysis membranes, polymerase chain reactors (PCR), flow

switch, inlet filter, and micropumps.[68-70] Monitoring elements such as various types of flow sensors have been reported.[68-69] Table 1.1 is adapted from Kricka's review,[70] and shows a list of various combinations of integrated components that have been demonstrated. It is not the goal of this section to review all the reported components, but rather to give the reader a sense of what is available and to point out that these components will eventually serve as building blocks for a μTAS unit, just like resistors, amplifiers, capacitors, etc serve as building blocks in an integrated circuit.

| Components | Combinations of components | | | | | | | | | | | | |
|---|---|---|---|---|---|---|---|---|---|---|---|---|---|
| Microvalve | | | | | | | ✓ | ✓ | ✓ | | | | |
| Micropump | | | ✓ | ✓ | | | ✓ | | ✓ | ✓ | | | |
| Heater | | ✓ | | | | | | | | | | | |
| Electronic Control Circuitry | | | | | | | | | ✓ | | | | |
| Detector | | | | | ✓ | | ✓ | ✓ | ✓ | | | | ✓ |
| Reaction Chamber | ✓ | ✓ | ✓ | ✓ | ✓ | ✓ | ✓ | ✓ | ✓ | ✓ | ✓ | ✓ | ✓ |
| DNA Isolation | | | | | | | | | | | ✓ | | |
| Microdialysis | | | | | | | | | | | | | ✓ |
| Cell Isolation | ✓ | | | | | ✓ | | | | ✓ | | | |
| Cell Lysis | ✓ | | | | | | | | | | | ✓ | |
| Fertilization | | | | | | ✓ | | | | | | | |
| PCR | ✓ | ✓ | | | | | | | | | | ✓ | |
| Capillary Electrophoresis | | | ✓ | ✓ | | | | | | | | ✓ | |
| Enzymatic Reaction | | | ✓ | | | | | | | | | | |
| Immunoassay | | | | ✓ | | | | | | | | | |
| Microarray | | | | | ✓ | | | | | | | | |
| Reference | 71 | 72 | 73 | 74, 51 | 75 | 76 | 77 | 78 | 79 | 80 | 81, 82 | 83 | 84 |

Table 1.1 Combinations of components integrated into microanalytical systems. Adapted from reference # 70.

## 1.5 Introduction to Waveguides

The initial motivation for μTAS was the need for industrial process and environmental monitoring.[14] It was therefore natural in the early development of μTAS to attempt to combine the microfluidic component of μTAS with fiber optic or integrated optical sensors routinely used for monitoring purposes. The fact that most μTAS devices were fabricated on glass makes integrated optic sensing an attractive addition to a μTAS.

The first generally accepted study of guided waves on and within a conducting structure appeared in 1910.[85] However, little further study was performed until the development of high frequency microwave sources shortly before World War II when

research was conducted using microwave radiation. In early 1960 Osterberg and Smith[86] demonstrated the first optical guided wave apparatus, using glass sheets and prisms. The set-up provided optical guidance by coupling a light beam into a planar film. Although waveguiding research has been primarily motivated by applications in communications, it has also found tremendous application in sensor technology. Optical fiber sensors and integrated optic sensors have been the subject of many books, to which interested readers are referred.[87-89]

The structure of a waveguide consists of a core, in which light is confined, and a cladding, or substrate surrounding the core, as shown in Figure 1.2. The basic principle of waveguiding is the fact that the refractive index of the core, $n_1$, is higher than that of the cladding, $n_0$. The light beam coupled into the waveguide is confined in the core by total internal reflection. The condition for total internal reflection at the core-cladding interface is given as

$$n_1 \sin\left(\frac{\pi}{2} - \phi\right) \geq n_0 \tag{1}$$

Since the angle $\phi$ is related to the incident light angle $\theta$ by the equation

$$\sin\theta = n_1 \sin\phi \leq \sqrt{n_1^2 - n_0^2} \tag{2}$$

we can obtain the critical condition for total internal reflection as

$$\theta \leq \sin^{-1}\sqrt{n_1^2 - n_0^2} \equiv \theta_{max} \tag{3}$$

where $\theta_{max}$ denotes the maximum light acceptance angle of the waveguide and $\sin\theta_{max}$ is commonly known as the numerical aperture (NA). The fundamentals of optical waveguides are the subject of many books to which interested readers are referred.[90-98]

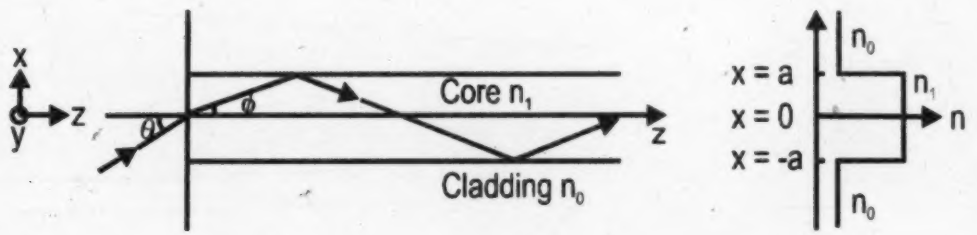


Figure 1.2 Basic structure and refractive-index profile of the optical waveguide.

Glass has been a favourite choice in waveguide fabrication because of its relatively low cost, excellent transparency, high threshold to optical damage and availability in various sizes. The usual methods employed to make glass waveguides include sputtering, chemical vapor deposition, sol gel coating, ion implantation and ion exchange. The ion exchange technique, which was first demonstrated in 1972,[99] is by far the most popular method, due to its simplicity and flexibility in customizing the numerical aperture and dimensions.

## 1.5.1 Thermal Ion Exchange Waveguide

An ion exchange waveguide is formed by exchanging ions in the glass (usually $Na^+$) with ions of larger size or higher polarizability, such as $Ag^+$, $K^+$, $Cs^+$, or $Tl^+$. The refractive index of the exchanged region increases, thus giving rise to a waveguide. Ion exchange can be a purely thermal process, or may be assisted by an electric field to accelerate the process. Typically, ions are introduced into the glass from a molten salt bath, but in the case of an electric field driven ion exchange, a thin metallic film can be used as the ion source. The following sections will outline the subjects relevant to the understanding of this study. A broader introduction to ion exchange waveguides can be found in several reviews and books.[98, 100-101]

### *1.5.1.1 Driving Mechanism*

The various constituents in a multicomponent oxide glass can be classified according to the bond strength between their cations and the oxygen atoms. Oxides with strong bonds are the *network formers*, which include $SiO_2$, $B_2O_3$, $GeO_2$, $P_2O_5$ and $As_2O_3$. *Network intermediates*, such as ZnO and PbO, contribute to the strength of the network but cannot form glasses by themselves. Finally, *network modifiers*, which are loosely bonded to the network, are typically added to give the glass a certain property such as lower softening point or a greater resistance to bubble formation during melting. Common additives in this class are $Na_2O$, CaO and $K_2O$.

In the thermal ion exchange process, loosely bound ions in the glass (typically $Na^+$) are exchanged with ions in a molten salt, assisted by high temperature. For example, a glass substrate containing $A^+$ is immersed in a molten salt containing

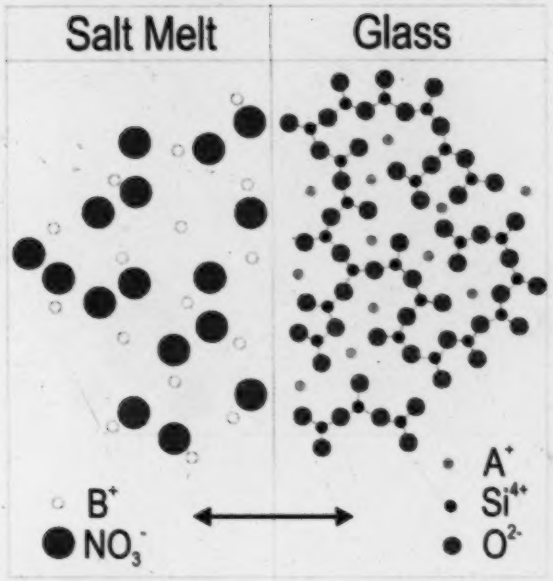


Figure 1.3 Diagram of melt-glass interface. When thermal agitation is applied, the cations $A^+$ are exchanged by cations in the salt melt, $B^+$. (Adapted from reference 98)

chemically similar ions, $B^+$, which are interchangeable with $A^+$ in the glass. At the glass-molten salt interface, both ion concentrations suddenly drop from a finite value to zero, as illustrated in Figure 1.3. When enough thermal energy is provided to this non-equilibrium situation, one $A^+$ is replaced by one $B^+$ and the ions gradually diffuse away from the interface. At high temperatures, the thermal energy makes the glass matrix less rigid and allows the exchange process and ion transport to be accelerated.

### *1.5.1.2 Characterization Techniques*

Knowledge of the optical characteristics of a waveguide is important, and is often necessary for device design or specification. Parameters such as effective refractive index, mode profile, refractive index profile, transmission spectrum, and propagation losses must be measured in order to provide information on the characteristics of a particular waveguide. While only the effective refractive index measurement will be introduced, a more complete list of characterization techniques for optical waveguide is provided in the references.[98]

### 1.5.1.2.1 Effective Refractive Index by Prism Coupling Technique

The principle of the prism coupling method is shown schematically in Figure 1.4. An incident light beam enters the prism at an angle θ. The light beam forms an angle ϕ to the normal of the prism base. The phase velocity in the z-direction in the prism and in the gap between the prism and the waveguide is determined by angle ϕ,

$$v_i = \frac{c}{n_p \sin\phi} \tag{4}$$

where $n_p$ is the refractive index of the prism and c is the speed of light in vacuum. Efficient coupling of light into the waveguide occurs only when $v_i$ is equal to the phase velocity, $v_m$, of one of the guided modes of the waveguide (m = 0, 1,2,...). When $v_i = v_m$ of any mode, light is coupled into the substrate and the reflected light from the waveguide surface decreases. The propagation constant of the mode can be determined from the angle of incidence of the laser light, the wavelength and the index of refraction of the prism. Information about the refractive index profile of the planar waveguide follows from knowledge of the propagation constant of the mode.

To measure the effective refractive index of a waveguide, a two-prism setup as illustrated in Figure 1.5 is typically used. The waveguide is mounted with the two prisms pressed against it. Laser light is coupled into the waveguide through the first prism and

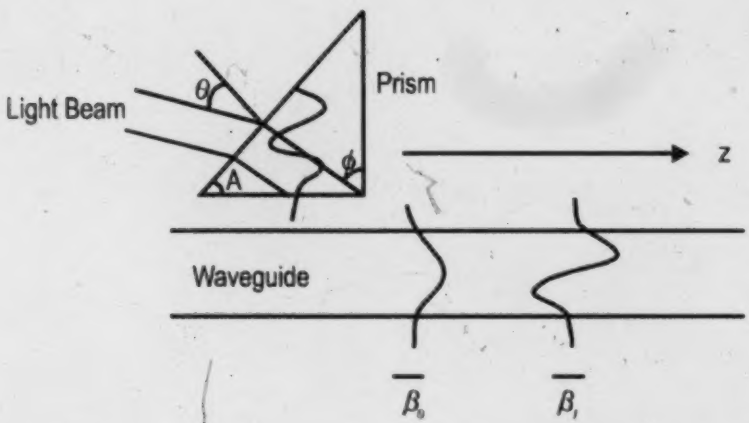


Figure 1.4 Principle of prism coupling. θ, ϕ, and A are angles as indicated in the figure. $\overline{\beta}_0$ and $\overline{\beta}_1$ are examples of two different modes propagating in the waveguide. (Adapted from reference 98)

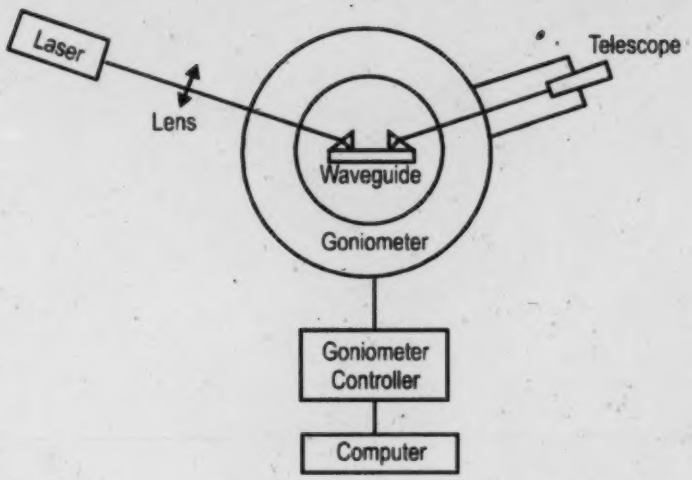


Figure 1.5 A typical experimental setup for measuring coupling angles in the prism-coupling method. (Adapted from reference 98)

coupled out through the second prism. The intensity of the output light is measured as a function of the incident light angle θ. The prism coupling method provides a simple, fast and accurate way of measuring the effective refractive index of a planar waveguide.

## 1.6 Scope of This Thesis

The development of μTAS for many chemical or biochemical analyses demonstrated its potential for routine use in clinical diagnostics, drug discovery, environmental monitoring and more. The focus of this study is on the ultimate goal of μTAS, namely automation with minimal human involvement.

Chapter 2 explores the use of an ion exchange waveguide to integrate optical components onto a microfluidic device. The difficulties involving such an undertaking were determined and partially resolved. However, more work is needed beyond this preliminary study to further refine the fabrication and integration of the waveguide.

Chapter 3 provides a theoretical explanation of the effect of corners on sample band broadening. When more and more sample processing components are added and more channels are packed into the small area a microchip offers, the layout of the separation channel will eventually need to become serpentine in order to maximize the

number of devices per wafer. The knowledge learned about corner effects was applied to the design of the device used in Chapter 4.

Chapter 4 reports on the development of a detection method for multichannel analysis and the use of a system built to explore ACE based IA in a 6-channel format. The chapter explains in detail all the required considerations for such a system and the difficulties involved. A number of solutions to those difficulties are presented. The usefulness of the system was demonstrated for the quantification of an anti-estradiol assay using both single channel calibration and cross-channel calibration methods.

Chapter 5 presents a general dilution method for construction of an n-times diluter for any type of analysis. Dilution can be viewed as an important pretreatment step for IA and other analyses. The serial dilution method was proposed and demonstrated to be superior compared to single step dilution method. A dilution factor of up to 1000 was demonstrated and various design issues were explored.

Finally Chapter 6 briefly summarizes each of the preceeding chapters, with some discussion and suggestions for future work.

## 1.7 References


1 Widmer, H.M. *Trends Anal. Chem.* **1983**, *2*, VIII

2 Widmer, H.M.; Erard, J.F.; Grass, G. *Intern. J. Environ. Anal. Chem.* **1994**, *18*, 1

3 Widmer, H.M.; Grolimund, K. *ACS Symposium Series 250* **1984**, pp. 13

4 Graber, N.; Lüdi, H.; Widmer, H.M. *Sens. Actuators B* **1990**, *1*, 239

5 Staehelin, J.; Graber, N.; Widmer, H.M. *Intern. J. Environ. Anal. Chem.* **1991**, *43*, 197

6 Manz. A; Verpoorte, E.; Raymond, D.E.; Effenhauser, C.S.; Burggraf, N.; Widmer, H.M. *Proc. MicroTAS* Anal. Methods Instrum. **1996** *Spec. Ed.*, 5-27

7 Terry, S.C. *Ph.D. Dissertation* Stanford University, 1975

8 Terry, S.C.; Jerman, J.H.; Angell, J.B. *IEEE Trans. Electron Devices* **1979**, *ED-26*, 1880-1886

9 Manz, A.; Miyahara, Y.; Miura, J.; Watanabe, Y.; Miyagi, K.; Sato, K. *Sens. Actuators B* **1990**, *1*, 249-255

10 Manz, A.; Graber, N.; Widmer, H.M. *Sens. Actuators B* **1990**, *1*, 244-248

11 Knox, J.H.; Gilbert, M.T. *J. Chromatogr.* **1979**, *186*, 405

12 Müller, S.; Scheidegger, D.; Haber, C.; Simon, W. *J. High Resolution Chromatogr.* **1991**, *14*, 174

13 Monning, C.A.; Jorgenson, J.W. *Anal. Chem.* **1991**, *63*, 802

14 Widmer, H.M. *Proc. μTAS Anal. Methods. Instrum.* **1996**, *Spec. Ed.*, 3-8

15 Effenhauser, C.S.; Bruin, G.J.M.; Paulus, A. *Electrophoresis* **1997**, *18*, 2203-2213

16 Blankenstein, G.; Larsen, U.D. *Biosensors & Bioelectronics* **1998**, *13(3-4)*, 427-438

17 Van Den Berg, A.; Lammerink, T.S.J. *Topics in Current Chemistry* **1998**, *194*, 21-49

18 Kricka, L.J. *Clin. Chem.* **1998**, *44:9*, 2008-2014

19 Dolník, V.; Liu, S.; Jovanovich, S. *Electrophoresis* **2000**, *21*, 41-54

20 Becker, H; Gärtner, C. *Electrophoresis* **2000**, *21*, 12-26

21 McDonald, J.C.; Duffy, D.C.; Anderson, J.R.; Chiu, D.T.; Wu, H.; Schueller, O.J.A.; Whitesides, G.M. *Electrophoresis* **2000**, *21*, 27-40

22 Carrilho, E. *Electrophoresis* **2000**, *21*, 55-65

23 Oleschuk, R.D.; Harrison, D.J. *Trac-Trend Anal. Chem.* **2000**, *19(6)*, 379-388

24 *Proc. μTAS '94 Workshop*, Van den Berg, A.; Bergveld, P. (Eds.), Kluwer Academic Pub., Dordrecht 1995

25 *Proc. μTAS '96* Anal. Methods Instrum. **1996** *Spec. Ed.*, Widmer, H.M.; Verpoorte, E.; Barnard, S. (Eds.)

26 *Proc. μTAS '98 Workshop*, Harrison, D.J.; Van den Berg. A. (Eds.), Kluwer Academic Pub., Dordrecht 1998

27 *Proc. μTAS ' 2000 Symposium*, Van den Berg, A.; Olthuis, W.; Bergveld, P. (Eds), Kluwer Academic Pub., Dordrecht 2000

28 Kohlrausch, F. *Ann. Phys. (Leipzig)* **1897**, *62*, 209

29 Schmalzing, D.; Nashabeh, W. *Electrophoresis* **1997**, *18*, 2184-2193

30 Bao, J.J. *J. Chromatogr. B* **1997**, *699*, 463-480

31 Schmalzing, D.; Buonocore, S.; Piggee, C. *Electrophoresis* **2000**, *21*, 3919-3930

32 Rippel, G.; Corstjens, H.; Billiet, H.A.H.; Frank, J. *Electrophoresis* **1997**, *18*, 2175-2183

33 Guijt-van Duijn, R.M.; Frank, J.; van Dedem, G.W.K.; Baltussen, E. *Electrophoresis* **2000**, *21*, 3905-3918

34 *Immunoassay*, Christopoulos, T.K.; Diamandis, E.P. (Eds), Academic Press, San Diego 1996

35 Tiselius, A. *Thesis: Nova Acta Tegiae Sociates Scientiarum Upsaliensis* **1930**, Ser. IV, *7*, Number 4

36 Tiselius, A. *Trans. Faraday Soc.* **1937**, *33*, 524

37 Consden, R.; Gordon, A.H.; Martin, A.J.P. *Biochem. J.* **1944**, *38*, 224

38 Consden, R.; Gordon, A.H.; Martin, A.J.P. *Biochem. J.* **1946**, *40*, 33

39 Raymond, S.; Weintraub, L. *Science* **1955**, *130*, 711

40 Hjertén, S. *Chromatogr. Rev.* **1967**, *9*, 122-219

41 Jorgenson, J.; Lukacs, K.D. *Anal. Chem.* **1981**, *53*, 1298-1302

42 Terabe, S.; Otsuka, K.; Ichikawa, K.; Tsuchuya, A.; Ando, T. *Anal. Chem.* **1984**, *56*, 111-113

43 *Handbook of Capillary Electrophoresis*, Landers, J.P. (Ed.), CRC Press, Boca Raton 1996

44 *Capillary Electrophoresis, Theory and Practice*, Camilleri, P. (Ed.), CRC Press, Boca Raton 1997

45 Harrison, D.J.; Manz, A.; Fan, Z.; Lüdi, H.; Widmer, H.M. *Anal. Chem.* **1992**, *64*, 1926-1932

46 Effenhauser, C.S.; Bruin, G.J.M., Paulus, A. *Electrophoresis* **1997**, *18*, 2203-2213

47 Dolník, V.; Liu, S.; Jovanovich, S. *Electrophoresis* **2000**, *21*, 41-54

48 Bøg-Hansen, T.C. *Anal. Biochem.* **1973**, *56*, 480-488

49 Heegaard, N.H.H; Kennedy, R.T. *Electrophoresis* **1999**, *20*, 3122-3133

50 Hadd, A.G.; Jacobson, S.J.; Ramsey, J.M. *Anal. Chem.* **1999**, *71*, 5206-5212

51 Chiem, N.H.; Harrison, D.J. *Clin. Chem.* **1998**, *44*, 591-598

52 Von Heeren, F.; Verpoorte, E.; Manz, A.; Thormann, W. *Anal. Chem.* **1996**, *68*, 2044-2053

53 Rodríguez, I.; Jin, L.J.; Li, S.F.Y. *Electrophoresis* **2000**, *21*, 211-219

54 Gosling, J.P. *Clin. Chem.* **1990**, *36*, 1408-1427

55 *Principles and Practive of Immunoassay*, Price, C.P.; Newman, D.J. (Eds.), Stockton Press, New York 1991

56 *Practical Immunoassay*, Butt, W.R. (Ed.), Marcel Dekker, New York 1984

57 *Methods of Immunological Analysis*, Masseyeff, R.F.; Albert, W.H.; Staines, N.A. (Eds.), VCH, New York 1993

58 Schultz, N.M.; Kennedy, R.T. *Anal. Chem.* **1993**, *65*, 3161-3165

59 Shimura, K.; Karger, B.L. *Anal. Chem.* **1994**, *66*, 9-15

60 Grossman, P.D.; Colburn, J.C.; Lauer, H.H.; Nielsen, R.G.; Riggin, R.M.; Sittampalam, G.S.; Rickard, E.C. *Anal. Chem.* **1989**, *61*, 1186-1194

61 Harrison, E.J.; Fluri, K.; Chiem, N.; Tang, T.; Fan, Z. *Tranducers '95 – Eurosensors IX*, The 8th International Conference on Solid-State Sensors and Actuators, and Eurosensors IX, Stockholm, Sweden 1995, 752-755

62 Koutny, L.B.; Schmalzing, D.; Taylor, T.A.; Fuchs, M. *Anal. Chem.* **1996**, *68*, 18-22

63 Woolley, A.; Sensabaugh, G.F.; Mathies, R.A. *Anal. Chem.* **1997**, *69*, 2181-2186

64 Kheterpal, I.; Scherer, J.R.; Clark, S.M.; Radhakrishnan, A.; Ju, J.; Ginther, C.L.; Sensabaugh, G.F.; Mathies, R.A. *Electrophoresis*, **1996**, *17*, 1852-1859

65 Shi, Y.; Simpson, P.C.; Rcherer, J.R.; Wexler, D.; Skibola, C.; Smith, M.T.; Mathies, R.A. *Anal. Chem.* **1999**, *71*, 5354-5361

66 Huang, Z.; Munro, N.; Hühmer, A.F.R.; Landers, J.P. *Anal. Chem.* **1999**, *71*, 5309-5314

67 Bruno, A.E.; Baer, E.; Völkel, R.; Effenhauser, C.S. *Proc. μTAS Workshop*, Kluwer Academic Publishers, **1998**, 281-285

68 Blankenstein, G.; Larsen, U.L. *Biosensors & Bioelectronics* **1998**, *13(3-4)*, 427-438

69 van den Berg, A.; Lammerink, T.S.J. *Topics Curr. Chem.* **1998**, *194*, 21-49

70 Kricka, L.J. *Clin. Chem.* **1998**, *44:9*, 2008-2014

71 Wilding, P.; Kricka, L.J.; Cheng, J.; Hvichia, G.E.; Shoffner, M.A.; Fortina, P. *Anal. Biochem.* **1998**, *257*, 95-100

72 Northrup, M.A.; Gonzalez, C.; Lehew, S.; Hills, R. *Proc. μTAS Workshop*, Kluwer Academic Publishers, **1995**, 139

73 Jacobson, S.C.; Ramsey, J.M. *Anal. Chem.* **1996**, *68*, 720-723

74 Chiem, N.; Harrison, D.J. *Anal. Chem.* **1997**, 1691, 373-378

75 Eggers, M.; Hogan, M.; Reich, R.K.; Lamture, J.; Ehrlich, D.; Hollis, M.; et al *Biotechniques*, **1994**, *17*, 516-525

76 Kricka, L.J.; Faro, I.; Heyner, S.; Garside, W.T.; Fitzpartick, G.; McKinnon, G.; et al *Biologie Prospective: 9e Colloque de Pont-á-Mousson*, Montrouge: J Libbey, **1997**, 42-46

77 Nakagawa, S.; Shoji, S.; Esashi, M. *Proc. IEEE-MEMS Workshop*, **1990**, 89-94

78 Shoji, S.; Esashi, M.; Matsuo, T. *Sens. Actuators* **1988**, *14*, 101-107

79 Walther, I.; van der Schoot, B.H.; Jeannert, S.; Arquint, P.; de Rooij, N.F.; Gass, V.; et al *J. Biotechnol.* **1994**, *38*, 21-32

80 Li, P.C.H.; Harrison, D.J. *Anal. Chem.* **1997**, *69*, 1564-1568

81 Cheng, J.; Kricka, L.J.; Wilding, P. *Topics Curr. Chem.* **1998**, *194*, 215-231

82 Sosnowski, R.G.; Tu, E.; Butler, W.F.; O'Connell, J.P.; Heller, M.J. *Proc. Natl. Acad. Sci. USA* **1997**, *94*, 1119-1123

83 Waters, L.C.; Jacobson, S.C.; Kroutchinina, N.; Khandurina, J.; Foote, R.S.; Ramsey, J.M. *Anal. Chem.* **1998**, *70*, 158-162

84 Freaney, R.; McShane, A.; Keaveny, T.V.; McKenna, M.; Rabenstein, K.; Scheller, F.W.; et al *Ann. Clin. Biochem.* **1997**, *34*, 291-302

85 Hondros, D.; Debye, P. *Ann. Phys.* **1910**, *32*, 465

86 Osterberg, H.; Smith, L.W. *J. Opt. Soc. Amer.* **1964**, *54*, 1078

87 *Fiber Optic Sensors: An Introduction for Engineers and Scientists*, Udd, E. (Ed.), Wiley-Interscience Publication, New York 1991

88 *Optical Fiber Sensors: Systems and Applications, Volume II*, Culshaw, B.; Dakin, J. (Eds), Artech House, Norwood, MA 1989

89 *Optical Fiber Sensors: Components and Subsystems, Volume III*, Culshaw, B.; Darkin, J. (Eds.), Artech House, Boston 1996

90 *An Introduction to Optical Waveguides*, Adams, M.J., John Wiley & Sons Ltd., New York 1981

91 *Optical Waveguides*, Kapany, N.S.; Burke, J.J., Academic Press, New York 1972

92 *Introduction to Integrated Optics*, Barnoski, M.K. (Ed.), Plenum Press, New York 1974

93 *Planar Optical Waveguides and Fibres*, Unger, H.G., Clarendon Press, Oxford 1977

94 *Optical Waveguide Theory*, Snyder, A.W.; Love J.D., Chapman and Hall, New York 1983

95 *Optical Waveguide Concepts*, Vassallo, C., Elsevier Science Publisher, New York 1991

96 *Foundations of Optical Waveguides*, Owyang, G.H., Elsevier, New York 1981

97 *Fundamentals of Optical Waveguides*, Okamoto, K., Academic Press, San Diego 2000

98 *Introduction to Glass Integrated Optics*, Najafi, S.I. (Ed.), Artech House, Boston 1992

99 Izawa, T.; Nakagome, H. *App., Phys. Lett.* **1972**, *21*, 584-586

100 Findakly, T. *Opt. Eng.* **1985**, *24(2)*, 244-250

101 Ramaswamy, R.V. *J. Lightwave Technol.* **1988**, *6(6)*, 984-1001

# Chapter 2

# Integrating ion-exchange waveguides onto microfluidic chips

## 2.1 Introduction

Many detection methods have been demonstrated for microchip based devices.[1-11] Optical detection methods,[2-4, 8] especially fluorescence detection,[2] have been the principal method used to date. Although absorbance detection remains the more generally accepted method for conventional flow systems due to its wide applicability, fluorescence detection is favored in microchip based systems because of its sensitivity and ease of implementation. A typical single point fluorescence detection system includes a light source to excite the samples, lenses to collimate and focus the light source, mirrors to bring the light source to the microchip, filters to eliminate unwanted scattered light, and a microscope and photomultiplier tube (PMT) to collect the fluorescence emission. Similar in concept to the use of microfabricated channels to deliver fluid within a microchip, integrated optics (IO) can be used to deliver photons within a chip. Integrating optical components within a microchip can provide a way to reduce the bulk of the detection system, simplifying the overall system and eventually minimizing the manual alignment and assembly of optical components.

Often the utilization of a waveguide for detection on a chip is based on evanescent wave detection for the purpose of chemical or biochemical sensing.[12-13] This has the disadvantage of only detecting components within a few microns of the wall of the flow channels. The idea of integrating optical components with microfluidic components for the purpose of reducing the bulk optical equipment has been around since the early years of μTAS.[14-19] One of the simpler approaches involved integrating fiber optics into microfluidic chips, as demonstrated by Liang et al[3] for a glass device and Soper and coworkers[20-21] for plastic devices. Alternatively, waveguides could be fabricated onto microfluidic devices utilizing microfabrication techniques such as reactive ion etching (RIE), flame hydrolysis deposition[22] and chemical vapour deposition.[23] These approaches typically start with deposition of a glass layer on top of an oxidized Si wafer. A layer of glass with ions such as Ge(IV) is then formed to give a region with higher

refractive index. RIE may then be used to etch away unwanted regions of the doped glass, leaving a channel waveguide. Another layer of pure glass may then be deposited to bury the waveguide, followed by RIE to carve out fluidic channels. In this chapter, we describe an alternative method for the fabrication of integrated channel waveguides.

This study represents an attempt to simplify the fabrication of the waveguide detector described by Liang et al[3] That device involved the microfabrication of an absorbance and/or fluorescence detection U-cell and included the challenging process of inserting optical fibers within channels etched in a microfluidic chip to bring the optical fibers into proximity with the flow path of the U-cell. In the current work thermal ion-exchange was used to fabricate the waveguides in order to replace the optical fibers. The simplicity and flexibility of this fabrication procedure appeared to offer advantages. Waveguides are readily formed in glass substrates by ion exchange techniques.[24-26] Thermally or electrically assisted diffusion can be used to drive $K^+$, $Cs^+$, or $Ag^+$ ions into silicate glasses, forming regions within the glass with a different refractive index than the substrate material. Such waveguides are known to have higher losses than optical fibers, but we hoped the losses would be acceptable over the short distances required on the microchip. The design used in this work was intended to perform both fluorescence and absorbance detection.

## 2.2 Experimental

### 2.2.1 Materials and Reagents

$AgNO_3$ used for ion exchange was from Caledon Laboratories Std. (Georgetown, ON) and standard cyanine 5 (Cy-5) was from Beckman (Fullerton, CA). A pH 10.5, 15 mM boric acid buffer, adjusted with 1 M NaOH, prepared using ultra pure water (Millipore Canada, Mississauga, ON), was used to dilute the Cy-5 standards. All solutions were filtered with 0.2 μm Nylon-66 membrane filters (Fisher, Edmonton, AB). Photomask glass was from Agfa-Gevaert (made in Belgium, obtained from Precision Photoglass Inc, Mountain View, CA)

### 2.2.2 Fabrication Procedure

#### *2.2.2.1 Waveguide Fabrication*

A glass petri dish was loaded with $AgNO_3$ (~ 5 g) and then heated in a Thermolyne 10500 Furnace (Syborn Corporation) until the $AgNO_3$ melted. Once the oven reached the desired temperature the substrate was placed into the petri dish, with the surface intended for ion-exchange face down. No air bubbles were trapped between the substrate and the molten $AgNO_3$. The oven temperature was monitored every 1-2 hours with a thermocouple (DiGi-Sense from Cole Parmer). After the desired number of hours of ion exchange, the substrate was removed from the molten $AgNO_3$ and allowed to cool on an Al metal block before being washed with distilled water.

#### *2.2.2.2 Device Fabrication*

The device, shown in Figure 2.1, was fabricated on 3 x 3 inch square, 1.6 mm thick photomask glass using a three mask process. The exploded view of the U-cell region shows the three masks being used in the process. Mask 1 was used to etch a channel 0.2 μm deep, using conventional photolithography techniques.[2] After the shallow channels were etched, the substrate was sputtered with a layer of Al and Mask 2 was used to develop the openings needed to fabricate ion-exchange waveguides. The substrate was then placed into the molten $AgNO_3$. After the waveguides were formed, the Al metal mask was stripped using an etching solution of $H_3PO_4/HNO_3/H_2O$ with a 20/2/5 volume ratio. The final Mask 3 was used to etch the 10 μm deep microfluidic channels. The etched and ion-exchanged substrate was then scored and fractured at the end of the waveguide, as indicated by the broken line in Figure 2.1. The substrate and cover plate in which 2 mm access holes were drilled were vigorously cleaned[27] and bonded. A low temperature bonding process[28] was used to ensure that the waveguide was not destroyed by high temperature. The temperature was ramped up to 230 °C at a rate of 4 °C/minute, and held at 230 °C for two hours before allowing the oven to cool back to room temperature.

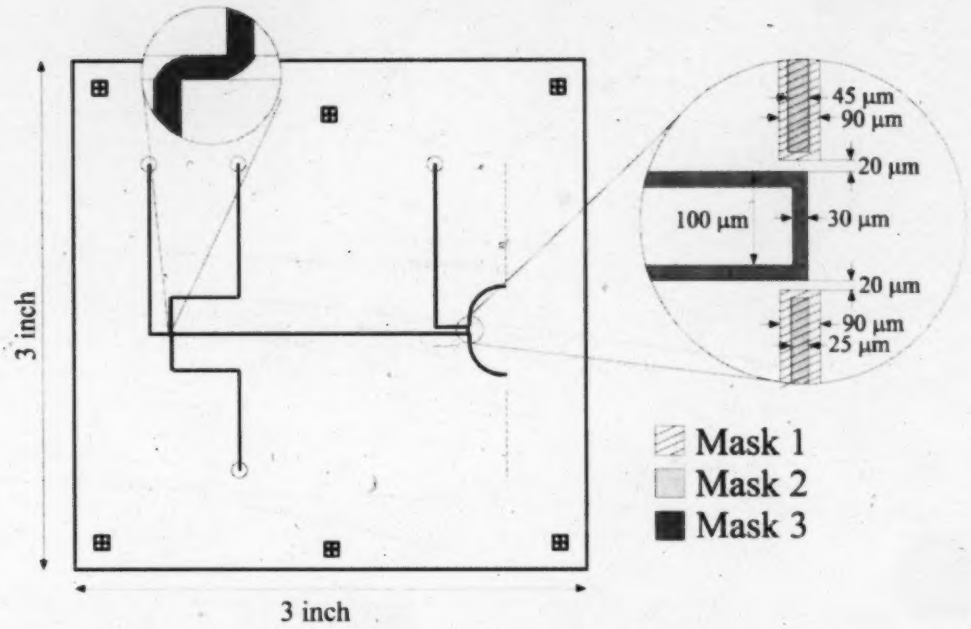


Figure 2.1 Device layout used in this work. Expanded view shows the U-cell region and the three masks used for the fabrication process. Circles represent reservoirs for sample and buffer. The dashed lines near the curved waveguides indicate the position of the fracture made to expose the waveguide. Small squares around the device were used for alignment purposes during the fabrication process. The double-T injector offset is 100 µm. Mask 1 was used to perform a shallow etch of channels containing the waveguides while Mask 2 was used to fabricate the channel waveguides and finally Mask 3 was used to form the fluid channels. The dimensions shown in the expanded view are the feature widths on the mask.

### 2.2.3 Waveguide Characterization Methods

A profilometer (Alphastep 200, Tencor Instruments, KLA-Tencor Corp., San Jose, CA) was used to measure the swelling of the waveguide. Energy Dispersive Spectrometry (EDS), Backscattered Electron Imaging (BSE), and X-ray maps were obtained at the University of Alberta Electron Microprobe Laboratory using a JOEL 8900 microprobe equipped with five wavelength dispersive spectrometers and an energy dispersive spectrometer. The waveguide depth and index were obtained using a Metricon PC1200 Prism Coupler (Metricon Corp., Pennington, NJ).

### 2.2.4 Instrumentation

The 633 nm He-Ne laser (5 mW, Melles Griot) was used as the light source. The laser beam was initially focused through a 15 cm focal length, 1" diameter quartz lens (Newport) and then through a 0.5" diameter, LightPath™ LCX045 GRIN lens (Newport) onto the waveguide. Fluorescence emission was collected with a 25x Leitz Wetzlar (Germany) microscope objective (numerical aperture 0.35, working distance 15 mm), and focussed through an Omega 682DF22 bandpass filter (Omega, Brattelboro, VT) and a 800 μm pinhole onto a Hamamatsu R1477 photomultiplier tube (PMT). A homebuilt $10^7$ gain transimpedance amplifier with a 360 Hz bandwidth was used for PMT amplification. The PMT signal was filtered through a six-pole Butterworth filter (Krohn-Hite Model 3342) with a 50 Hz low-pass cutoff frequency. House vacuum was used as the negative pressure source to pull sample through the U-cell with a flow rate in the range of ~2 cm/s.

## 2.3 Results and Discussion

### 2.3.1 Addressing Device and Waveguide Fabrication Issues

Figure 2.1 shows the device layout used in this work, consisting of a typical double-T injector design[29] with a 100 μm offset, and a 9.7 cm long separation channel that included a 100 μm long U-cell for optical detection. All fluidic channels were 10 μm deep and 50 μm wide. The device also included a pair of curved launching and collection waveguides located within a shallow channel 90 μm wide. The launch waveguide mask feature width was 25 μm, and the collection waveguide feature width was 45 μm. The following discussion describes the tests that ultimately led to the device design shown in Figure 2.1. Issues such as the longevity of various metal masks in the molten $AgNO_3$ bath during the ion-exchange process, the amount of glass substrate swelling due to stress arising from $Na^+$ ion being exchanged by $Ag^+$ ion, and the optimal number of hours required for the ion-exchange process are addressed.

#### *2.3.1.1 Longevity of Metal Masks*

Since this project was intended to replace the inserted fiber optics approach used by Liang et al[3] with ion-exchanged waveguides, two channel waveguides had to be

fabricated at either end of the U-cell. A mask with the desired pattern of waveguides was thus required to survive the process of ion-exchange. Three metal masks, Au/Cr, Ti and Al were tested, and Al was found to be the best mask, as it survived 24 hours in molten $AgNO_3$ bath at ~275 °C. However, we later found literature suggesting that a nonmetallic mask might be preferred in the case of $Ag^+$ ion exchange as the silver ions tend to reduce to metallic silver at the boundaries of a metallic mask, increasing the absorption losses of the waveguides.[26]

### *2.3.1.2 Swollen Waveguide*

It is known that stress caused by exchanging two ions with dissimilar radii will result in swelling of the glass surface at the region of exchange.[25-26, 30] To evaluate this effect, two channel waveguides were fabricated at 275 °C for 15 hours with 25 μm and 210 μm feature widths. The swelling profile was measured by a profilometer, as shown in Figure 2.2. We observed approximately 0.15 μm and 0.2 μm swelling normal to the surface for the 25 and 210 μm feature widths, respectively. The widths of the swollen region were approximately 50 μm and 250 μm for the two mask openings. The depth of the $Ag^+$ diffusion into the substrate can be approximated from measurements with the

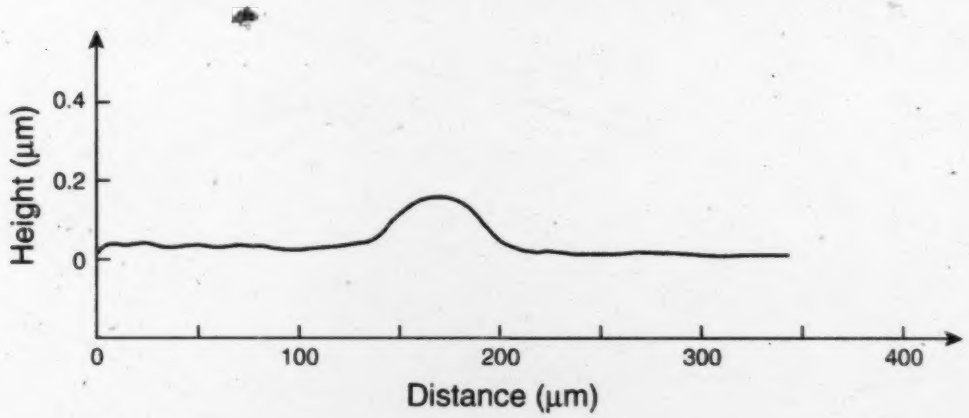


Figure 2.2 Profilometer trace showing the swelling of the photomask glass surface due to stress upon forming a channel waveguide. The profile resulted from 15 hours of ion-exchange at 275 °C for mask feature width of 25 μm.

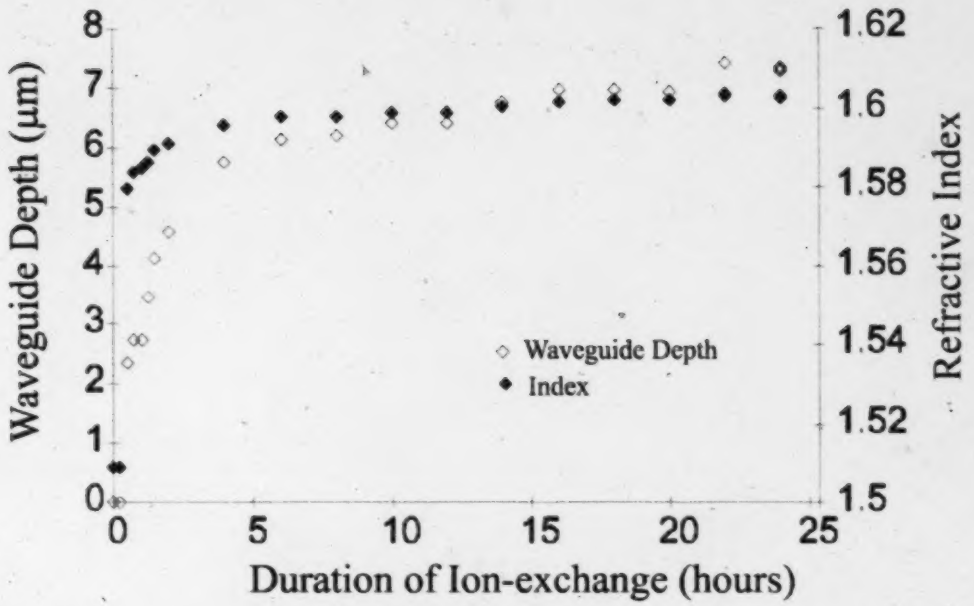


Figure 2.3 Plot of waveguide depth on the left axis and refractive index on the right axis versus hours of $Ag^+$ ion-exchange into photomask glass at 275 °C.

prism coupler. As shown in Figure 2.3, the maximum depth of the waveguide fabricated in this study was 7.5 µm. These observations showed that the $Ag^+$ ions have a much larger lateral diffusion distance compared to the depth they penetrate into the glass. This offset arises since the stress in the glass eventually stops the diffusion into the substrate, while there was less stress in the lateral direction to limit the width of the waveguide. Although the swelling was minimal, it was enough to impair bonding of a glass cover plate, due to the air gap between the two glass plates. This problem was addressed by the use of a shallow etch channel, fabricated deep and wide enough to contain the swollen waveguide, so that normal bonding could occur.

### *2.3.1.3 Ion-exchange Duration Optimization*

In order to optimize the ion-exchange duration, waveguides were first prepared for various exchange times. The depth and index change measured using a prism coupler is plotted versus hours of exchange in Figure 2.3. The results clearly demonstrate that at 275 °C, approximately five hours was required to obtain a maximum change of index for

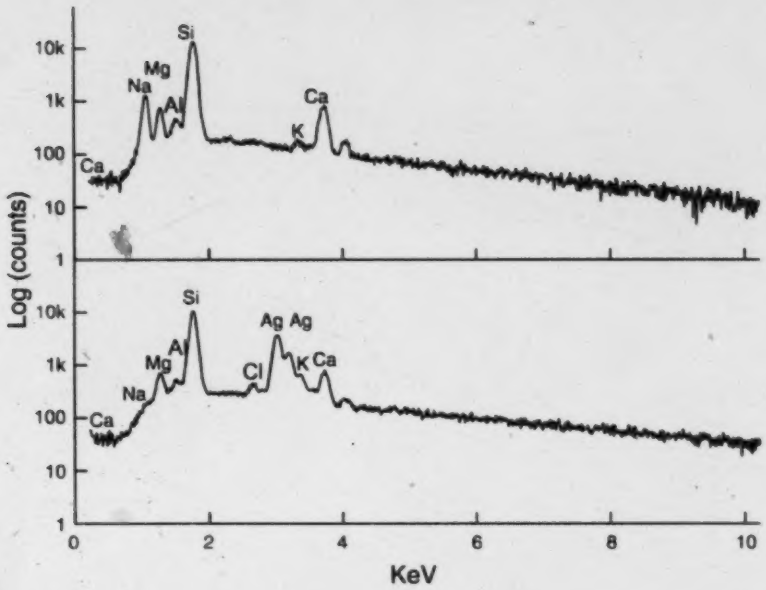


Figure 2.4 Energy Dispersive Spectrum of a photomask glass substrate with $Ag^+$ channel waveguide. The bottom spectrum shows the ion-exchanged region, indicating the presence of Ag and the depletion of Na. The ion composition of the substrate is shown in the top spectrum; a Na peak is seen and there is no Ag peak.

the waveguide. In addition, energy dispersive X-ray analysis, shown in Figure 2.4, was used to confirm that $Na^+$ in the glass had been exchanged by $Ag^+$. Backscattered electron imaging distinguishes between heavy and light elements, and was used to measure the lateral diffusion of the ion-exchange process. An X-ray mapping technique was also used to confirm that the lighter element shown in the backscattered electron images was in fact mainly composed of Na, while the heavier element region consisted mainly of Ag. Figure 2.5 shows the width of a channel waveguide prepared with a 25 μm feature width as a function of the hours of exchange at ~275 °C. Profilometer measurements of swelling showed a 50 μm wide swollen zone for 15 hours exchange study as demonstrated in Figure 2.2. This width is consistent with the 45 μm measured for a 12 hour exchange by backscattered electron imaging. These data were used to determine the width of the shallow channel etch that would be required to contain a particular size of waveguide. Backscattered electron images such as that shown in Figure 2.6 also revealed that the edges of the waveguide fabricated were very rough. Such roughness can be expected to lead to high losses due to scattering during light propagation.

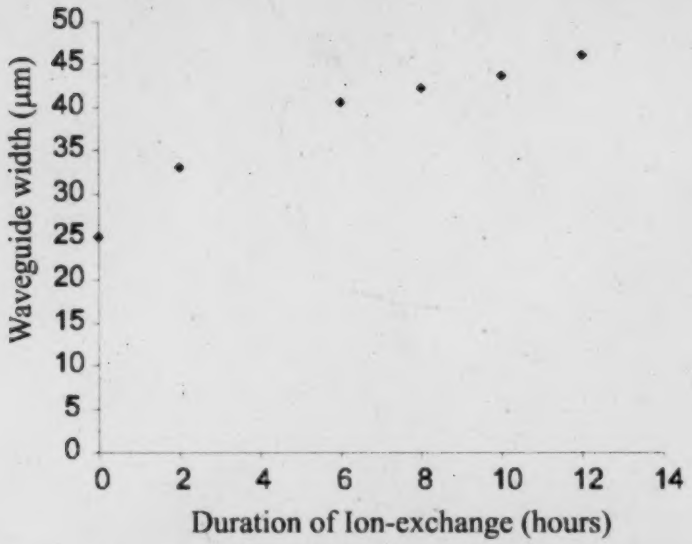


Figure 2.5 Plot of width of $Ag^+$ waveguide versus the hours of ion-exchange at ~275 °C for a channel formed via a 25 μm mask opening.

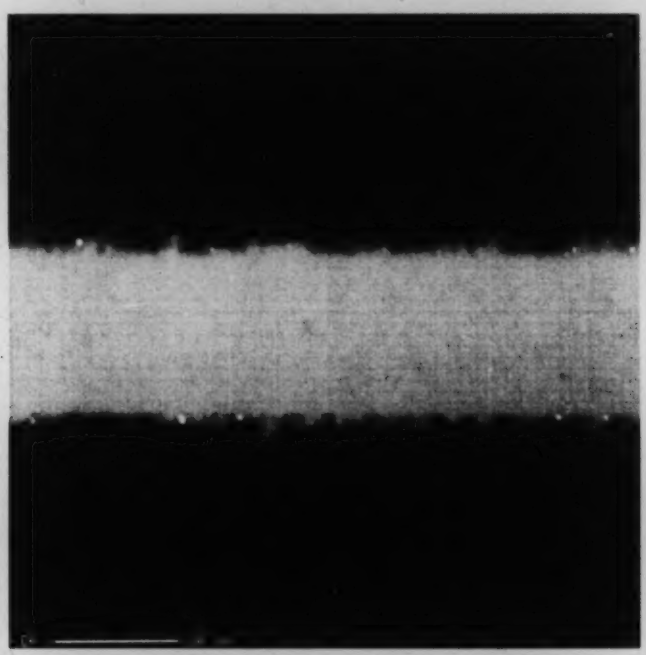

Figure 2.6 Backscattered electron image of a $Ag^+$ channel waveguide fabricated via a 25 μm mask opening, using two hours of ion-exchange at ~275 °C. The dark region corresponds to the glass substrate, while the lighter region represents the channel waveguide. The image indicates a rough wall for the waveguide, which likely contributes to scattering losses.

### 2.3.1.4 *Device Bonding*

A bonding temperature lower than that used during the ion-exchange process was required to perform adequate bonding without destroying the waveguide. A temperature ramp program, as described in the Experimental Section of this chapter, was tested on planar and channel waveguides. The resulting planar waveguide was then analyzed with the prism coupler. The depth of the waveguide increased slightly from ~7.4 μm to ~7.6 μm and the index of refraction was essentially unchanged within experimental error (1.6028 ± 0.0005 to 1.6020 ± 0.0004). The channel waveguides were visually inspected after going through the bonding cycle. We observed a slight increase of the waveguide width and staining with a yellowish color. The stain might be due to the reduction of $Ag^+$ to form metallic Ag, which is known to often be present and causes high losses in $Ag^+$ ion exchange waveguides.[26, 31-32]

### 2.3.1.5 *Waveguide Layout*

For convenience we decided to use the coupling method illustrated in Figure 2.7 to launch the laser beam into the waveguide. A curved waveguide design was used to ensure the light illuminating the U-cell was delivered by the launch waveguide, eliminating stray light not coupled into the waveguide. A curved waveguide was used on the collection side to prevent stray light from reaching the detector. Several curved waveguides ranging from a 1 mm to 5 mm radius of curvature were fabricated and tested to determine which radius of curvature would give acceptable transmission of the laser beam. The waveguide with a 5 mm radius was found to propagate enough light to be observed at the exit, and thus was used in this work. A larger radius of curvature will surely have lower losses due to the curve; however, as we increase the radius of curvature we must also increase the length of the waveguide. We later found that in studies by Nafaji et al on S-shape potassium ion-exchange waveguides, approximately 11 dB of excess losses (compared to the equivalent straight waveguide) were observed for a 20 mm radii S-shape waveguide.[26] Based on that study, the curved waveguide fabricated in this work probably incurred a substantial amount of loss.

The addition of shallow etch channels to contain the swollen waveguides meant that two walls were required to keep the shallow channels physically separated from the

U-cell, as illustrated in the exploded view of Figure 2.1. A wall ~10 μm wide after etching was judged to be adequate for proper bonding, and prevention of leakage of sample into the waveguide channels. The inclusion of a wall between the launch waveguide and the U-cell meant that there is a gap between the end of the waveguide and the U-cell, so that some loss of light throughput was expected. Similarly the wall between the U-cell and the collection waveguide was expected to reduce the collection efficiency.

#### *2.3.1.6 Final Device Layout*

Based on the analysis outlined above, the final design of the device shown in Figure 2.1 was selected. The exploded view in Figure 2.1 shows the U-cell region and the three masks used in fabrication, with all the mask dimensions indicated. The first mask was used to perform a 0.2 μm deep etch of two 90 μm wide curved channels used to contain the launching and collecting waveguides. The second mask, made by depositing an Al mask, provided the pattern for the 25 μm and 45 μm lines for the ion-exchanged launching and collecting waveguides, respectively. Finally, the third mask layer consists of the pattern desired for the fluidic channels, which included a U-cell for absorbance detection.

### 2.3.2 Device Evaluation

The design of the device was intended to allow both absorbance and fluorescence detection to be performed separately or simultaneously. In the absorbance detection mode, a light source would be focused and coupled into the launching waveguide. Transmitted light, after passing through the U-cell, would propagate through the collection waveguide onto detection optics located at the exit of the collection waveguide. In the fluorescence detection mode, light would be delivered to the U-cell by the launch waveguide, and detection would be performed by placing the optical axis of a microscope and PMT normal to the plane of the device above the U-cell. The fluorescence performance was tested, but the losses proved too large for the absorbance design to be evaluated.

### 2.3.2.1 Fluorescence Detection

We first evaluated the performance of the waveguide by using the instrument setup illustrated in Figure 2.7. A laser beam was coupled to the launch waveguide as described in Section 2.2.4, to deliver the excitation beam to the U-cell. The device was mounted on translation stages, allowing movement in XYZ directions. In addition, a rotational stage was used to allow a "tilting" motion along the laser beam axis. These translation and rotation motions allow manipulation of the device, such that the excitation beam can be coupled into the launching waveguide. A detector located above the U-cell was used to detect any fluorescence emission. A sample of Cy-5 dye was placed in reservoir D, while a negative pressure was applied at reservoir C to draw the sample to the U-cell. The calibration curve in Figure 2.8 shows linearity between fluorescence signal and concentration, but there is a slight non-zero intercept. The slope and intercept of the linear regression line are 0.00189 ± 0.00005 and 0.009 ± 0.003, respectively. However, the detection limit (DL) of approximately 10 nM was rather high for

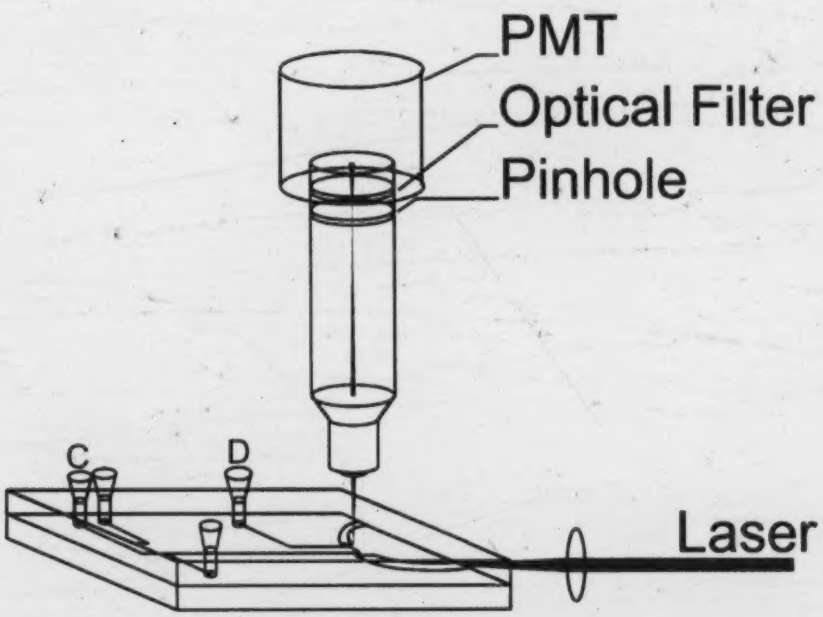


Figure 2.7 Laser induced fluorescence (LIF) setup showing coupling of the laser to the waveguide using a focussing lens. The sample of Cy-5 was sucked continuously through the flow channel with a negative pressure source.

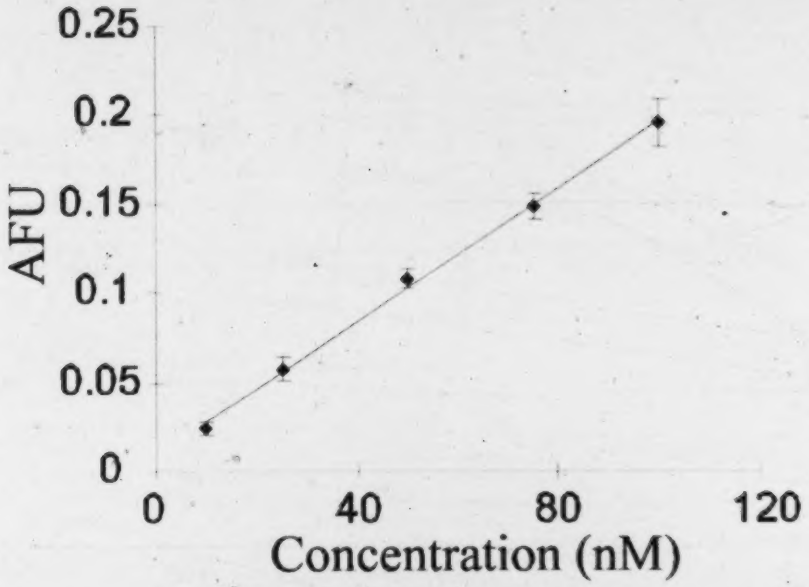


Figure 2.8 Fluorescence calibration curve (plot of arbitrary fluorescence unit vs. concentration) for continuously flowing Cy-5. Limit of detection is 10 nM. The excitation and emission wavelengths are 633 nm and 682 nm, respectively. The line represents linear regression line with $R^2 = 0.998$. Error bars shown indicate the standard deviation (n=6).

fluorescence detection on a microchip, which can be as low as 9 pM for this dye.[33] Liang et al[3] reported a DL of 3 nM for fluorescein at 488 nm excitation using the same U-cell design, but with inserted fibers as the waveguides. In contrast, Chiem et al[34] achieved 30 pM DL for fluorescein using the conventional two lens fluorescence detection setup. Liang et al[3] concluded their observed DL was high because of poor coupling of light into the optical fiber. Given our similar DL, we have also concluded that the high DL was due to the low power level transmitted through the waveguide to the U-cell.

### *2.3.2.2 Waveguide Losses*

It appeared that the major limitation to obtaining a lower DL was the high loss associated with the ion-exchanged waveguide, which greatly decreased the excitation power. Losses could occur in many places, such as at the point of coupling into the launching waveguide, during propagation through the waveguide[35-36] and at the entrance and exit walls between the shallow channel and the U-cell. It was estimated that the losses at the coupling step were the greatest, as only a very small fraction of the laser

beam was coupled into the launching waveguide. This was evident by the glow of scattered and reflected light at the entrance to the waveguide and the bright exit beam at the other end of the chip, along the laser path of the input beam, indicating not much light was coupled into the waveguide. In addition the possibility of some shape mismatch between the circular laser spot and the semicircular waveguide could decreased coupling efficiency if the spot is not diffraction limited in size. The losses were compounded when the light propagated through the waveguide, as evident by the glow of the waveguide from the scattered light. While not quantified, taken together these losses indicated that an extremely low amount of laser power entered the U-cell. In fact, the extremely high losses of the waveguide prevented us from performing an absorbance experiment, as the amount of light collected by the detector through the collection waveguide was undetectable, although a faint light was observed at the exit wall of the U-cell. Also the 10 μm wall separating the fluid channel from the waveguide was probably too wide for efficient coupling of the transmitted light back into the collection waveguide.

It was clear from this work that fabrication of a low loss waveguide is crucial to the success of the device being used in the absorbance mode. More important is the need for a high efficiency coupling method so that more light may be coupled into the waveguide in the first place.

## 2.4 Conclusion

The fabrication of an ion-exchange channel waveguide within a microfluidic chip has been demonstrated. Problems associated with swelling of the substrate could be resolved. The waveguide was shown to guide the laser beam to the U-cell of the device and excite the Cy-5 dye to give a fluorescence signal. However, the waveguide created in this project was far from satisfactory. The simple thermal diffusion driven ion-exchange process resulted in a waveguide with high losses, as evident by the glow of the waveguide during waveguiding of laser beam. Furthermore, the coupling efficiency is rather poor and thus compounded the problem of low light throughput. Nevertheless, the experiment demonstrates that an ion-exchange waveguide could be fabricated and used to guide light within the microchip. Further improvement on low loss waveguide

fabrication[32, 37-38] will allow a microchip device capable of absorbance measurements at lower wavelength to be realized. The use of different doping ions such as $Cs^+$, that cause a larger refractive index change, and are known to create waveguides with less scatter is one step that could be taken to reduce losses.[39] In addition, the use of a focusing grating coupler as shown by Kunz[40] could be used to reduce the coupling losses, thus improving the light throughput of the waveguide.

## 2.5 References


1 Terry, S.C.; Jerman, J.H.; Angell, J.B. *IEEE Trans. Electron Devices* **1979**, *ED26*, 1880-1886.

2 Harrison, D.J.; Manz, A.; Fan, Z.; Lüdi, H.; Widmer, H.M. *Anal. Chem.* **1992**, *64*, 1926-1932.

3 Liang, Z.; Chiem, N.; Ocvirk, G.; Tang, T.; Fluri, K.; Harrison, D.J. *Anal. Chem.* **1996**, *68*, 1040-1046.

4 Mangru, S.; Harrison, D.J. *Electrophoresis* **1998**, *19*, 2301-2307.

5 Xue, Q.; Foret, F.; Dunayevskiy, Y.M.; Zavracky, P.M.; McGruer, N.E.; Karger, B.L. *Anal. Chem.* **1997**, *69*, 426-430.

6 Gavin, P.F.; Ewing, A.G. *J. Am. Chem. Soc.* **1996**, 118, 8932-8936.

7 Uhlig, A; Lindner, D.; Teutloff, C.; Schnakenberg, U.; Hintsche, R. *Anal. Chem.* **1997**, *69*, 4032-4038.

8 Norlin, P.; Öhman, O.; Ekström, B.; Forssén, L. *Sens. Actuators B* **1998**, *49*, 34-39.

9 Sato, K.; Kawanishi, H.; Tokeshi, M.; Kitamori, T.; Sawada, T. *Anal. Sci.* **1999**, *15*, 525-529.

10 Engel, U.; Bilgic, A.M.; Haase, O.; Voges, E.; Broekaert, J.A.C. *Anal. Chem.* **2000**, *72*, 193-197.

11 Tantra, R.; Manz, A. *Anal. Chem.* **2000**, *72*, 2875-2878.

12 Duveneck, G.L.; Verpoorte, E.; Oroszlan, P.; Pawlak, M.; Erbacher, C.; Spielmann, A.; Neuschäfer, D.; Ehrat, M. *Proc. MicroTAS*, Anal. Methods Instrum. **1996**, *Sp. Ed.*, 158-163.

13 Plowman, T.E.; Reichert, W.M.; Peters, C.R.; Wang, H.K.; Christensen, D.A.; Herron, J.N. *Biosensors & Bioelectronics* **1996**, *11*, 149-160.

14 Ache, H.J. *Proc. MicroTAS* Kluwer Academic Publishers, **1994**, 47-70.

15 Wolfbeis, O.S. *Proc. MicroTAS* Kluwer Academic Publishers, **1994**, 95-103.

16 Widmer, H.M. *Proc. MicroTAS*, Anal. Methods Instrum. **1996**, *Sp. Ed.*, 3-8.

17 Hoppe, K.; Svalgaard, M.; Kristensen, M. *Proc. MicroTAS*, Anal. Methods Instrum. **1996**, *Sp. Ed.*, 164-166.

18 Goddard, N.J.; Lenney, J.P.; Morey, J.C.; Fielden, P.R.; Snook, R.D. *Proc. MicroTAS*, Anal. Methods Instrum. **1996**, *Sp. Ed.*, 144-146.

19 Drapp, B.; Gauglitz, G.; Gottfried-Gottfried, R. *Proc. MicroTAS*, Anal. Methods Instrum. **1996**, *Sp. Ed.*, 198.

20 Waddell, D.; Stryjewski, W.J.; Soper, S.A. *Rev. Sci. Instr.* **1999**, *70(1)*, 32-37.

21 Ford, S.M.; Davies, J.; Kar, B.; Qi, S.D.; McWhorter, S.; Soper, S.A.; Malek, C.K. *J. Biomech. Eng.* **1999**, *121(1)*, 13-21.

22 Ruano, J.M.; Benoit, V.; Aitchison, J.S.; Cooper, J.M. *Anal. Chem.* **2000**, *72*, 1093-1097.

23 Hübner, J.; Mogensen, K.B.; Jorgensen, A.M.; Friis, P.; Telleman, P.; Kutter, J.P. *Rev. Sci. Instr.* **2001**, *72(1)*, 229-233.

24 Findakly, T. *Opt. Eng.* **1985**, *24(2)*, 244-250.

25 Ramaswamy, R.V. *J. Lightwave Technol.* **1988**, *6(6)*, 984-1001.

26 *Introduction to Glass Integrated Optics*, Editor, Najafi, S.I., Artech Hourse Inc., Norwood, MA, 1992.

27 Li, P.C.H., Harrison, D.J. *Anal. Chem.* **1997**, *69*, 1564-1568.

28 Chiem, N.; Shultz-Lockyear, L.; Anderson, P.; Skinner, C., Harrison, D.J. *Sens. Actuators B*, **2000**, *63*, 147-152.

29 Effenhauser, C.S.; Manz, A.; Widmer, H.M. *Anal. Chem.* **1993**, *65*, 2637-2642.

30 Garfinkel, H.M.; King, C.B. *J. Amer. Ceram. Soc.* **1970**, *53*, 686-691.

31 Rindone, G.E.; Weyl, W.A. *J. Amer. Ceram. Soc.* **1950**, *33*, 91-95.

32 Stewart, G.; Laybourn, P.J.R. *IEEE J. Quantum Electron.* **1978**, *QE-14*, 930-934.

33 Jiang, G.; Harrison, D.J. *Analyst* **2000**, *125*, 2176-2179.

34 Chiem, N.; Harrison, D.J. *Anal. Chem.* **1997**, *69*, 373-378.

35 Imai, M.; Haneda, N.; Ohtsuka, Y. *J. Lightwave Technol.* **1983**, *LT-1*, 611-615.

36 Stewart, G.; Millar, C.A.; Laybourn, P.J.R.; Wilkinson, C.D.W.; DeLaRue, R.M. *IEEE J. Quantum Electron.* **1977**, *QE-13*, 192-200.

37 Ingenhoff, J.; Lefebvre, P.; Zhang, W.G.; Li, C.Y.; Roβ, L.; Najafi, S.I. *Proc. SPIE* **1994**, *2401*, 188-196.

38 Findakly, T.; Garmire, E. *Appl. Phys. Lett.* **1980**, *37(10)*, 855-856.

39 Galechyan, M.G.; Dianov, E.M.; Lyndin, N.M.; Tishchenko, A.V. *Sov. Phys. Tech. Phys.* **1991**, *36(6)*, 641-645.

40 Kunz, R.E. *Sens. Actuators B* **1997**, *38-39*, 13-28.

# Chapter 3

# Analysis of Dispersion Caused by Corners in Microchip Capillary Electrophoresis System

## 3.1 Introduction

It has been recognized that excess dispersion can result from coiling gas chromatography columns,[1] capillary electrophoresis columns[2-4] and serpentine separation channels on microchips.[5-8] A 90 degree corner in a separation channel can be considered a special case of a coiled or serpentine separation channel and is a unique feature of microchip based capillary electrophoresis (CE) devices. The dispersion that occurs in a microchip CE system can mostly be represented by the same theoretical expressions used in conventional CE system. An exception to this is the influence of corners in the separation channel, for which there is no conventional equivalent. It has been commonly assumed and demonstrated by Ramsey,[5-6] Mathies[7] and Griffiths[8] that corners in a separation channel will contribute to the overall band broadening and should be avoided or corrected. Currently, most devices used in our group were designed with a straight, long separation channel and detection was performed before any corner. However, shrinking the devices into a more compact format for manufacturing purposes or packing more devices on a single wafer for high throughput purposes will inevitably demand that corners be introduced in order to create these long separation channels. It is therefore important to be able to estimate the corner-induced dispersion in microchip CE devices. This chapter attempts to study the extent of corner induced band-broadening effects by finite element simulation, Taylor dispersion modeling and experimentation using fluorescein as a sample.

Ramsey et al[6] suggested a race track model to described corner effects, which accounts for migration differences, field strength differences and transverse diffusion effects to predict excess dispersion induced by turns in microchip channels. Mathies and coworkers[7] demonstrated the use of that model to suggest a geometric correction for the turn-induced band broadening. Recently Griffiths and Nilson[8] presented the use of numerical methods to automatically vary and optimize turn geometry with the

assumption that the turn radius is much greater than the channel widths. All those studies showed that a sample plug flowing through a turn will be grossly skewed and broaden. These conclusions do not agree well with the experimental data obtained by Karl Fluri in Harrison's lab, in which he observed little band broadening for fluorescein (Fl) due to corners. In this chapter we present a qualitative calculation of corner induced band-broadening, based on finite-element simulations to demonstrate the effect of the diffusion coefficient on dispersion. Two simulations were performed, using parameters representative of small molecules such as Fl, and large molecules such as DNA. A more generic model based on Taylor Dispersion to estimate the dispersion caused by corners is also presented and the predictions are correlated with the experimental and simulation data.

## 3.2 Theory and Simulations

The flow profile in a sharp corner has certain dominant characteristics. In the absence of electroosmotic flow, flow along the vertical direction, the channel depth, will exhibit a plug shaped velocity profile for electrophoretic motion of ions. However, across the width of the channel the path lengths and the electric field vary substantially, creating a significant velocity difference for ions following different stream lines. The dispersion caused by this situation may be treated by a two dimensional model, in which advection arises from the velocity gradient across the channel width at a corner. The vertical dimension should not play a significant role since the concentration is invariant in this dimension. In the presence of electroosmosis, the eletroosmotic flow (EOF) profile in the vertical direction would remain plug like, while a significant variation in EOF would occur across the width. This treatment of EOF neglects any secondary flow term across the width induced by the path length difference in the corner.[9] We note that such an effect is known to reduce the apparent diffusivity of a solute, but inclusion of this effect would require 3-D modeling of flow (vide infra).

The effect of a non-uniform flow profile in at least one dimension was treated by Taylor[10,11] for a Poisseulle flow. This model has since been extended by others,[12-15] such as Aris,[15] to include a large range of non-uniform velocity profiles.[16] We will employ the Taylor-Aris approach to estimate band broadening induced within a sharp corner. The

non-uniform electroosmotic and electrophoretic flow of ions across the width of the channel results in a Taylor-Aris diffusivity contribution in one dimension, that contributes to the band broadening induced by a corner.

In order to evaluate the corner induced band broadening, a geometric factor related to the corner shape must be evaluated. We have used a commercial finite element solver, FlumeCAD, from Coventor, to evaluate this parameter. The software was used to describe pure electrophoretic flow in two dimensions. As discuss above, a 2-D calculation should be quite accurate for pure electrophoretic flow; in which no secondary flow should occur. We have then made the approximation that the geometric factor obtained may be used within the Taylor-Aris model for the combination both of electrophoresis and EOF.

### 3.2.1 Taylor Dispersion in a Corner

This section proposes a model to approximate corner induced band broadening based on Taylor dispersion. The model described was proposed and derived in collaboration with Luc Bousse of Caliper Technologies. The theory for dispersion of a component in a solution flowing along a tube was first presented by Taylor.[10,11] In the case of a circular tube, the flow velocity is parabolic in the absence of diffusion. This would cause a very large dispersion since the materials at the edges does not move while the materials at the center moves at a velocity $2\bar{u}$, where $\bar{u}$ is the average velocity. After time t, this causes dispersion equal to $2\bar{u}t$. In practice, however, diffusion is able to counteract this parabolic dispersion by moving materials from the center to the edges. Taylor's theory states that in the case where longitudinal velocity is slow compared to the rate of lateral diffusion, the dispersion is characterized by an effective diffusion coefficient given by

$$k = \frac{1}{48}\frac{\bar{u}^2 r^2}{D} \qquad (1)$$

where r is the radius of the tube and D is the molecular diffusion coefficient. This equation has been extended to other geometries and flow profile by other authors.[12-15] Van den Broeck[16] summarized the various results, stating that in general

$$k \propto \frac{\bar{u}^2 r^2}{D} \tag{2}$$

where the numerical coefficient of proportionality depends on the geometry. For a rectangular channel with one dimension much greater than the others, the coefficient is 8/945.[15,17]

Assume we can treat a corner-induced dispersion in a similar way by writing:

$$k = \alpha \frac{\bar{u}^2 W^2}{D} \tag{3}$$

where $\alpha$ is an unknown coefficient which is expected to be about $10^{-2}$, $\bar{u}$ is the average velocity in the channel before the corner and $W$ is the width of the channel. More generally, the transit time around a corner is a multiple of the time needed to move one channel width:

$$t_c = \gamma \frac{W}{\bar{u}} \tag{4}$$

where $\gamma$ is a proportionality constant. As a result, the dispersion $\sigma^2$ due to a single corner is given by:

$$\sigma^2 = 2kt_c = 2\gamma\alpha \frac{\bar{u} W^3}{D} \tag{5}$$

or

$$\sigma^2 = 2\beta \frac{\bar{u} W^3}{D} \tag{6}$$

where we expect $\beta$ to be in the range of $10^{-1}$ to $10^{-2}$.

For a separation channel of length $L$ with $n$ 90 degree angle corners, the overall corner induced dispersion will be the sum of each corner's contribution and the contribution from molecular diffusion:

$$\sigma^2 = n(2kt_c) + 2Dt_s \tag{7}$$

where $t_s$ is the time a component spent in the straight section of the separation channel. Another way of writing equation 7 is:

$$\sigma^2 = 2n(k - D)t_c + 2Dt_m \tag{8}$$

where the total migration time $t_m = t_c + t_s$. Equation 8 can be rewritten in terms of experimental parameters and approximated as equation 9 below, since k is typically much greater than D:

$$\sigma^2 = 2n\beta\frac{\bar{u}W^3}{D} + 2\frac{DL}{\bar{u}} \tag{9}$$

The dispersion can be used to determine the theoretical plate number, or more usefully, the plate height given by:

$$H = \frac{\sigma^2}{L} = 2n\beta\frac{\bar{u}W^3}{DL} + 2\frac{D}{\bar{u}} \tag{10}$$

Equation 10 has the advantage that other contributions to the plate height, such as the effects of injection and detection length can be added in the usual fashion.

### 3.2.2 Finite Element Simulations

Simulations were performed using FlumeCAD from Coventor (Cambridge, MA). A 90 degree L shaped channel was constructed with the dimensions indicated in Figure 3.1. Two simulations were performed using the sample species parameters listed in Table 3.1. The simulations represent a small molecule with a large diffusion coefficient, such as Fl, and a relatively large molecule such as DNA with a small diffusion coefficient. The mobility of both species was assumed to be the same, so that the effect

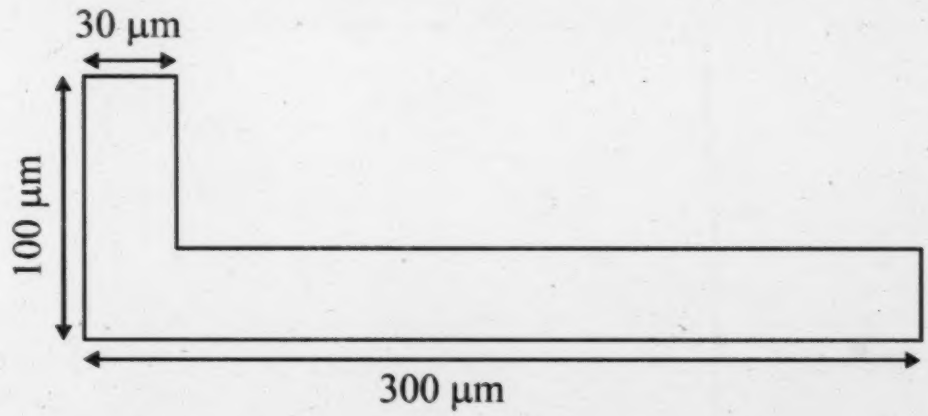


Figure 3.1 An "L" channel 30 µm wide used in the finite element simulation using FlumeCAD. The lengths are as indicated. Sample plug was placed at the shorter arm of the L channel and moved downstream with 2 V of applied voltage. The corresponding electric field is 54 V/cm.

| Simulation Parameters | Run 1 | Run 2 |
|---|---|---|
| Voltage applied (V) | 2 | 2 |
| Diffusion coefficient ($cm^2/s$) | $3.2 \times 10^{-6}$ | $3.2 \times 10^{-8}$ |
| Molecular Weight (Dalton) | 376.3 | 500,000 |
| Mobility ($cm^2/V \cdot s$) | $3 \times 10^{-4}$ | $3 \times 10^{-4}$ |

Table 3.1 Parameters used in finite element simulation using FlumeCAD.

of diffusion could be isolated and compared. Electroosmotic flow was not included. Figures 3.2 and 3.3 show the results of such simulations for an initial 50 μm long sample plug for small or large molecules, respectively. The higher diffusion coefficient in the case of the small molecule reduced the distortion of the sample plug and helped it recover a plug shape quickly, as demonstrated in Figure 3.2. Recovery required a length of approximately eight channel widths. The much more significant distortion expected for a large molecule is shown in Figure 3.3.

In order to estimate the value of β for equation 10, a straight channel 30 μm wide and 370 μm long was constructed in a similar fashion, using FlumeCAD software. A sample plug 50 μm long was moved downstream with the same simulation parameters as that for small molecule in the L corner. The diffused and dispersed plug was measured 2 s after injection and was compared to the plug size measured in the case where the sample plug moved through the L corner. The extra plug size was thus attributed to the band broadening induced by corner. Inputting the simulation parameters into equation 6 gave a value of $9.7 \times 10^{-3}$ for β. This result, although quasi-empirical, allows us to approximate the corner induced band broadening based on the Taylor theory presented and compared to the experimental data.

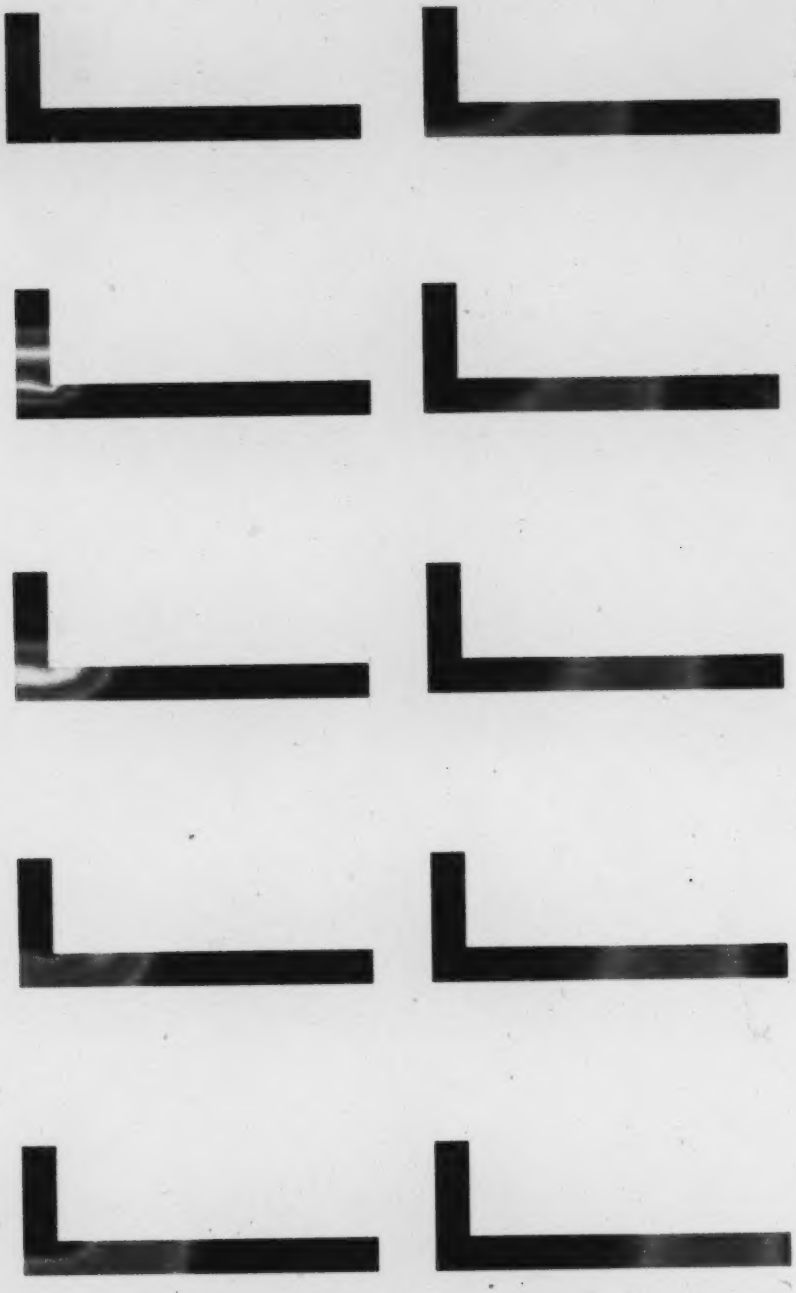

Figure 3.2 FlumeCAD simulation results using parameters listed in Run 1 column of Table 3.1. The initial sample plug is 50 μm long. Each frame is taken at 0.2 s interval. The sequence of frames indicated that the sample plug was uniformly distributed across the channel width after a distance of approximately 8 channel widths.

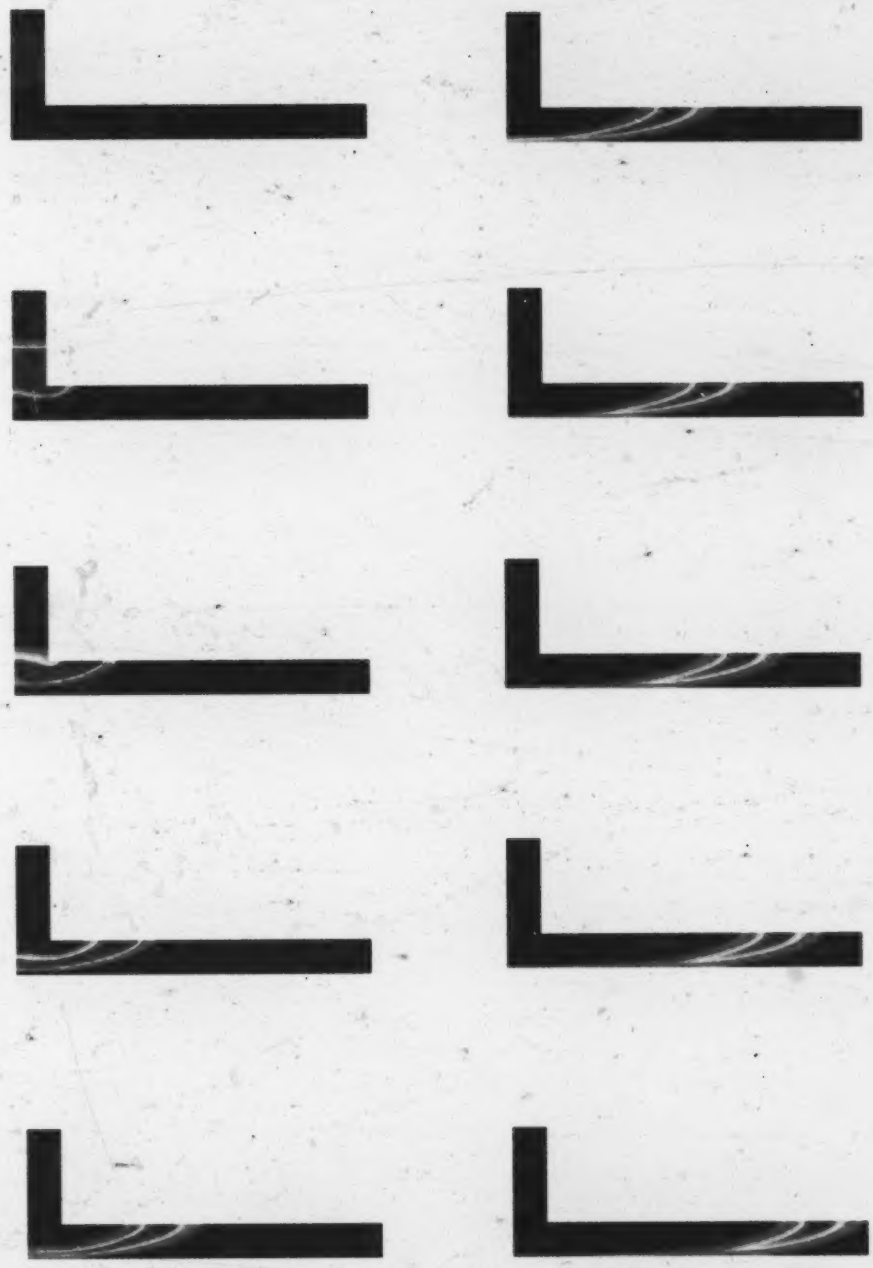

Figure 3.3 FlumeCAD simulation results for a large molecule with low diffusion coefficient. The simulation parameters were listed in column Run 2 of Table 3.1. Each frame is obtained at 0.2 s interval. The results indicated that corner induced band broadening is substantial for low diffusing molecules.

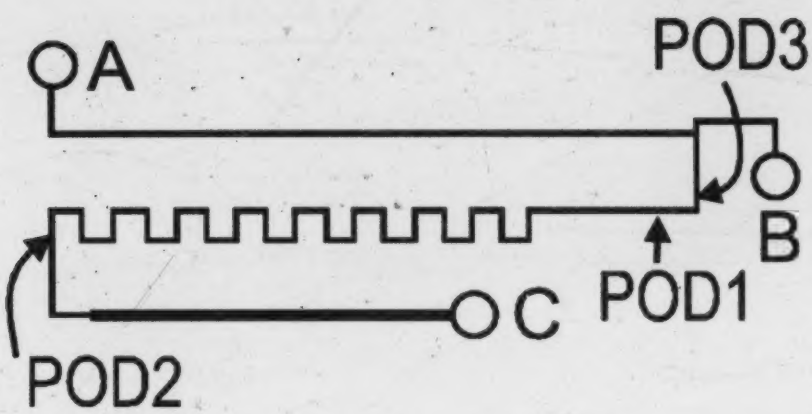


Figure 3.4 Diagram of the device used in this work. The device was either 30 μm wide, 9.9 μm deep or 46 μm wide, 17.9 μm deep. The circles and letters beside them indicate the location of reservoirs. During a typical experiment, the fluorescein sample was placed in reservoir A and buffer was placed in reservoirs B and C. Voltages were then applied between reservoirs A and B to inject a sample plug at the T injector. Separation then followed by application of voltages between reservoir B and C. Detection was performed at POD1, POD2 and POD3 and their relative distances from the injector are listed in Table 3.2.

## 3.3 Experimental Section

All experiments were performed by Karl Fluri with fluorescein (Sigma, Mississauga, ON) at a concentration of 5 μM. A pH 9.2 carbonate buffer, with 12 mM total carbonate was used for all experiments.

Devices were fabricated in Pyrex using methods previously described.[18] Figure 3.4 shows the layout of the device. Measured from the intersection, the channel lengths of sample, buffer and separation are 4.3 cm, 0.80 cm and 10.13 cm, respectively. The separation channel length is the effective lengths adjusted for the difference in width of the channel at the end.

Data acquisition was at either 20 or 100 points/seconds, with no appreciable difference noted. A Krohn-Hite filter was used, with two 4-pole 50 Hz low pass filters cascaded to give a time constant of 1/50 second.

A 20 mW 488 nm Ar ion laser operated at 4 mW was used as the source. The collection optics comprised a 10X lens and a 100 μm slit was used in all experiments. The diffusion coefficient for fluorescein is from Fan et al[18] and the mobility of fluorescein was measured to be $-3 \times 10^{-4}$ cm$^2$/V·s. Velocities are calculated from data presented in Table 3.2.

| Experimental Parameters | Device 1 | Device 2 |
|---|---|---|
| Channel width (μm) | 46 | 30 |
| Channel depth (μm) | 17.9 | 9.9 |
| Diffusion coefficient ($cm^2/s$) | $3.2 \times 10^{-6}$ | $3.2 \times 10^{-6}$ |
| Mobility ($cm^2/V \cdot s$) | $3 \times 10^{-4}$ | $3 \times 10^{-4}$ |
| Injector to POD1 distance (cm) | 1.25 | 0.55 |
| Injector to POD2 distance (cm) | 8.65 | 8.70 |
| Injector to POD3 distance (cm) | - | 0.48 |
| Injection voltages (V) | -300 at B<br>ground at A | -400 at B<br>ground at A |
| Separation voltages (V) | -4500 at C<br>+175 at B | -3000 V at C<br>+150 V at B |
| Injection time (ms) | 200 | 200 |
| Observed velocity (cm/s) | 0.167 | 0.213 |

Table 3.2 Experimental parameters for two devices of different channel widths and depths.

The experiment was performed with Fl placed in reservoir A, buffer in reservoirs B and C. Voltages of –300 V (46 μm channel width device) or –400 V (30 μm channel width device) were applied for 200 ms at reservoir B while reservoir A was held at ground and reservoir C was left floating to inject a small sample plug. The relay was then switched to apply 175 V (46 μm channel width device) or 150 V (30 μm channel width device) at reservoir B and –4500 V or –3000 V, respectively, at reservoir C. Detection was performed at POD1 and POD2 as indicated in Figure 3.4. In addition, detection was also performed at POD3 and compared to results obtained for detection at POD1 to determine whether the first corner contributed significant band broadening to the injected sample plug. The distances between injector to POD1, POD2 and POD3 are listed in Table 3.2.

## 3.4 Results and Discussions

A device shown in Figure 3.4 with a series of 33 corners was fabricated in Pyrex glass in order to study their influence on band-broadening in microchip CE devices. The corners are a right angle design, which is about the worst possible case as demonstrated by Mathies,[7] and so serve to test the magnitude to their effects. Figure 3.5 shows an image of a typical corner after the etching process. The outer corner is slightly rounded due to the isotropic etch process. Two different channel sizes were tested, one set of

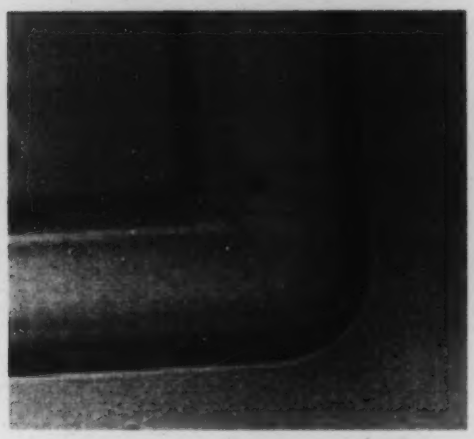

Figure 3.5 An image of a typical corner in the device shown in Figure 3.4 obtained using electron microscopy. The width of the channel is 30 µm wide. The inner corner makes a sharp 90 degree turn while the outer corner is slightly rounded due to the isotropic etch process used to fabricate the device.

devices were 17.9 µm deep and 46 µm wide, while the other set of devices were 9.9 µm deep and 30 µm wide.

Detection was performed both before and after the series of corners, in order to determine the contributions of other effects to band broadening and isolate the amount due to the corners. The location before and after the series of corners is designated as POD1 and POD2, respectively. The location of POD1 was after the first corner illustrated in Figure 3.4, owing to the greater convenience of setting up the optics. However, we also made measurements before the first corner (POD3) to verify that it had contributed no more band broadening effect than any other corner. Short plug lengths of about 80 µm were injected. The sequence of voltages applied is described in the experimental section, and various experimental parameters are identified in Table 3.2. Calculation of the plug size based on the time of injection and the voltage applied predicted about 65 µm lengths, while visual observation indicated the plugs were about 80 µm in length when originally formed. The absolute band broadening attributed to each corner is extremely small, at 0.067 ± 0.007 (n=30) and 0.032 ± 0.001 (n=21) µm/corner in the 46 and 30 µm wide channels, respectively.

The velocity of the fluorescein in the separation channel was 2.1 mm/s in the 30 µm device and 1.7 mm/s in the 46 µm device. At this rate it would take about 1s to travel from one corner to the next, which were 2 mm apart. Taking a diffusion coefficient of $3.2 \times 10^{-6}$ $cm^2/s$, this time period would correspond to diffusing a distance of 320 microns. Consequently, the fluid on one side of the channel is able to fully mix in the transit time between corners. The result is that the band broadening contribution at one corner would be unaffected by the next, since material is randomly distributed before it reaches the next corner.

Finite element simulations were used to provide a qualitative description of the effect of diffusion coefficient on the band broadening contribution from a single corner. The simulation results show that in the case of small molecules with a large diffusion coefficient, the effect is not as bad as in the case of large molecules with a small diffusion coefficient. The simulation also provided a quasi-empirical value of $\beta$ of $9.7 \times 10^{-3}$ be used in the model proposed in the theory section.

Using the model based on Taylor dispersion, the band broadening contributions of each corner for the 46 μm and the 30 μm channel width devices are predicted to be 0.14 and 0.052 μm/corner, respectively. One of the major reasons for the discrepancy between the model's prediction and the experimental data lies in the sensitivity of the model towards channel width, as shown in equation 10. The sensitivity decreases as the channel width reduces. This is partly due to the reduced distance the molecule must diffuse to return to a uniform concentration. Also the time spent travelling around the outside track of the wider corner would be larger, leading to more dispersion. In addition, the model assumes a rectangularly shaped channel while in practice, isotropic etching of the glass devices made the channel shape closer to a trapezoidal. The difference can be offset by substituting the actual channel width of the devices by a reduced channel width, corrected for the difference in the channel shapes. This was done by calculating the width required for a rectangle to give the same cross-sectional area as a trapezoid of the same height. The corrected widths were 38 and 26 μm for the 46 and 30 μm wide devices, respectively. The resulting band broadening contributions predicted were 0.086 and 0.037 μm/corner for the 46 and 30 μm wide devices, respectively. These results compared well to the experimental results of 0.07 and 0.03 μm/corner.

For molecules with small diffusion coefficient, the FlumeCAD simulation results for a large molecule, shown in Figure 3.3, were used to estimate the corner induced band broadening. The result gave a plate height value of ~64-70 μm/corner. The Taylor model was then used to estimate the corner induced band broadening based on the simulation parameters used in FlumeCAD as listed in Table 3.1. The model predicts a plate height of ~72 μm/corner. This value is similar to that obtained from the finite element simulation, indicating the results are self-consistent.

We further explored the applicability of the Taylor model to experimental results from Mathies and coworkers.[7] The electropherograms in Figure 3A of their publication were expanded 200 % using a photocopier, and the peak widths and retention times were measured using a ruler. Although this method is not very precise, it gave a general indication of how well the Taylor model can describe experimental results. For the 603 base pair peak, the plate number, N, after two corners was estimated to be 4702 when the tailing was ignored. However, the simulation in Figure 3.3 clearly shows that significant tailing will be caused by a sharp corner. Consequently, we treated the observed tailing in Figure 3A of reference 7 a real effect of the corner dispersion, reducing N to 1180. The corresponding plate height of ~16 μm/corner, was estimated using equation 11

$$H_y = \frac{L_x^2}{N_x L_y} + \frac{2D\Delta t}{L_y} \qquad (11)$$

where $H_y$ is the plate height at downstream position y, $N_x$ is the number of plates at upstream position x, $L_x$ and $L_y$ are the injector to detector distances at x and y, respectively, $D = 1 \times 10^{-7}$ cm$^2$/s is the molecular diffusion coefficient of DNA[7] and $\Delta t$ is the time required for the sample plug to travel from x to y. Values obtained from reference 7 were 2.75 and 3.82 cm for $L_x$ and $L_y$, respectively, with $\Delta t$ = 10 s. These estimates of observed corner dispersion agree favourably with a value of 15 μm/corner estimated by the Taylor dispersion model for an average channel width of 124 μm, $\beta = 9.7 \times 10^{-3}$, and $D = 1 \times 10^{-7}$ cm$^2$/s.

The agreement between experimental values and the Taylor dispersion model is very good, indicating the usefulness of the model as a predictive tool for corners. It is important to recognize that no arbitrary fitting parameters were used in obtaining the match. A numerical solver, in the form of FlumeCAD, was required in order to obtain the geometric factor β for the complex geometry of a right angle corner. However, β was obtained by comparison of two calculated results, not by fitting to experimental data.

An interesting effect of equation 10 is that smaller diffusion constants cause greater dispersion. If the diffusion is very small, such as in the case of DNA samples, dispersion will become rather large. On the other hand, for lower diffusion coefficients, one can reduce the flow rate ū to allow the sample enough time to diffuse across the channel and thus reduce the corners induced dispersion. However, this could only be

done if corners cause the dominant band broadening effect, since reducing the flow rate will increase the dispersion in the regular straight section of the separation channel.

## 3.5 Conclusions

This study has demonstrated the extent of corner induced dispersion for fluorescein in devices with different channel width. Calculations based on the finite element simulations in a 90 degree corner indicated that diffusion is an important factor to reduce the band broadening effect caused by corners. These calculations could be useful for systems with samples of extremely small diffusion coefficient, such as proteins and DNA. A newly developed model based on the theory of Taylor dispersion is demonstrated to be quite good in predicting the corner induced dispersion. In addition, the formula used in the model is expressed as a plate height and thus has the advantage of being able to simply add to plate height contributed by injection, detection and other band broadening effects. In view of the model's sensitivity to channel width, it could be further improved by correcting for the extra width due to shape differences between the actual device and the model's assumption. The model presented in this chapter will be useful for future design considerations of microchip CE devices. For small molecules such as fluorescein, plate height contributed by each corner is negligibly small. However, for big molecules with extremely small diffusion coefficient, reducing the channel width serves as a good way to reduce corners induced dispersions as demonstrated by Mathies and coworkers.[7] In addition, the model provided a tool for future design of microchip CE devices based on the diffusion coefficient of the sample of interest. It is worth pointing out that most authors have focused on corner induced dispersion effect for slowly diffusing molecules like DNA, or for much larger radius turn in a single 90 degree corner. The present study establishes that Taylor dispersion is not a very serious concern for rapidly diffusing molecules in tight corner.

## 3.6 Reference


1. Giddings, J.C. *J. Chromatogr.* **1960**, *3*, 520-523
2. Kasicka, V.; Prusik, Z.; Gas, B.; Stedry, M. *Electrophoresis* **1995**, *16*, 2034-2038
3. Srichaiyo, T.; Hjerten, S. *J. Chromatogr.* **1992**, *604*, 85-89

4. Wicar, S.; Vilenchik, M.; Belenkii, A.; Cohen, A.S.; Karger, B.L. *J. Microcolumn Sep.* **1992**, *4*, 339-348
5. Jacobson, S.C.; Hergenröder, R.; Koutny, L.B.; Warmack, R.J.; Ramsey, J.M. *Anal. Chem.* **1994**, *66*, 1107-1113
6. Culbertson, C.T.; Jacobson, S.C.; Ramsey, J.M. *Anal. Chem.* **1998**, *70*, 3781-3789
7. Paegel, B.M.; Hutt, L.D.; Simpson, P.C.; Mathies, R.A. *Anal. Chem.* **2000**, *72*, 3030-3037
8. Griffiths, S.K.; Nilson, R.H. *Anal. Chem.* **2000**, *72*, 5473-5482
9. Erdogan, M.E.; Chatwin, P.C. *J. Fluid Mech.* **1967**, *20*, 465-484
10. Taylor, G.I. *Proc. Roy. Soc. (London)* **1953**, *219A*, 186
11. Taylor, G.I. *Proc. Roy. Soc. (London)* **1954**, *223A*, 446
12. Smith, R. *Phil. Trans. Roy. Soc. Lond.* **1980**, *A219*, 467
13. Smith, R. *J. Fluid Mech.* **1981**, *108*, 43
14. Nunge, R.J.; Gill, W.H. *Ind. Engng. Chem.* **1969**, *61*, 33
15. Aris, R. *Proc. Roy. Soc. (London)* **1959**, *252A*, 538
16. Van Den Broeck, C. *Physica A* **1990**, *168*, 677-696
17. Doshi, M.R.; Daiya, P.M.; Gill, W.N. *Chem. Engng. Sci.* **1978**, *33*, 795-804
18. Fan, Z.H.; Harrison, D.J. *Anal. Chem.* **1994**, *66*, 177-184

# Chapter 4

# Development of a Multi-channel Microfluidic Analysis System Employing Affinity Capillary Electrophoresis for Immunoassay

## 4.1 Introduction

The ability to fabricate multiple fluid manifolds on a planar substrate provides the first necessary step towards the realization of simultaneous, multi-channel analysis systems.[1-5] A spectacular example of the development of a multi-channel separation system has been reported by Mathies and co-workers for DNA analysis.[6,7] Their efforts demonstrate the large quantity of data that can be obtained by multiplexing the number of separation channels per chip. The multiplexing of combined reaction and separation techniques[8,9] would further extend the utility of microfluidic devices for high rates of sample processing and analysis. However, multi-channel devices with integrated reaction and separation systems have yet to receive much attention. In this chapter, we explore the development of a 6-channel device for the performance of reagent and sample mixing, immunological reaction and affinity capillary electrophoresis (ACE)[10-14] separation. ACE has captured considerable attention as a developing immunoassay method, in large part due to the high speed it affords as compared to conventional immunoabsorbent techniques. ACE also offers reduced sensitivity to non-specific adsorption, reduced reagent consumption, and a much easier method of measuring affinity constants.[13,14] Sequential performance of ACE with conventional capillary electrophoresis (CE) instrumentation means the throughput of this method is lower than conventional immunoassay methods. Multiplexed systems for performing ACE will address this current drawback. Such systems may be used to evaluate a sample and several standards simultaneously, so that an entire calibration and immunoassay may be performed in a minute or less in an automated format.

The implementation of a multi-channel ACE device with integrated immunological reactions[9] involves a number of significant design issues. The layout and design of the flow channel manifolds within a multi-channel device is a significant challenge.[6,7] One must achieve uniform behavior between channels, and provide ready access for sample

delivery and for an optical detector. The device design, and choice of substrate materials, should permit convenient fabrication and reproduction. An interface to the chip must provide electrical contact and fluid reservoirs, and a scheme must be devised for the use of voltage to control the flow within the manifolds.[15,16] A multi-channel detection apparatus must also be designed and assembled.[5-7] This chapter will focus on each of these design issues, and the performance we have achieved with the designs selected. An anti-estradiol immunoassay,[17] and a direct immunoassay for ovalbumin[16] were used to characterize the multi-channel system.

A multi-channel immunoreactor designed for performing assays may be operated in several different modes. In a "cross-channel" mode some channels may be used for calibration, while others are used for samples, providing simultaneous calibration and assay with each run. This mode of operation will provide the shortest "time-to-result" per sample, but demands a high degree of uniform analytical behavior and reproducibility between channels. An "independent channel" mode on the other hand would see each channel run both samples and standards, providing increased sample throughput, but a longer "time-to-result" for a given sample. This mode of operation requires reproducibility within a channel, but is not so demanding of cross-channel reproducibility. Clearly, for either mode of operation, the reproducibility of mixing, reaction and injection within a multi-channel system requires careful evaluation and so has been the subject of this study.

## 4.2 Experimental Section

### 4.2.1 Device Design

Figure 4.1 illustrates the layout of the SPIDY device which was designed by Cameron Skinner, with assistance by this author. It consists of six independent mixer, reactor, injector and separation manifolds. We will refer to each of these independent manifolds with numbers 2 to 7, clockwise from the bottom left, for the purpose of identification. Channels 1 and 8 on either side of the six separation channels were included to run a constant stream of dye for optical alignment and optimization, as indicated by the expanded view in the top right of Figure 4.1. Access holes to the channels were laid out on a 16 x 16 mm grid. The serpentine reactors were 39 mm long.

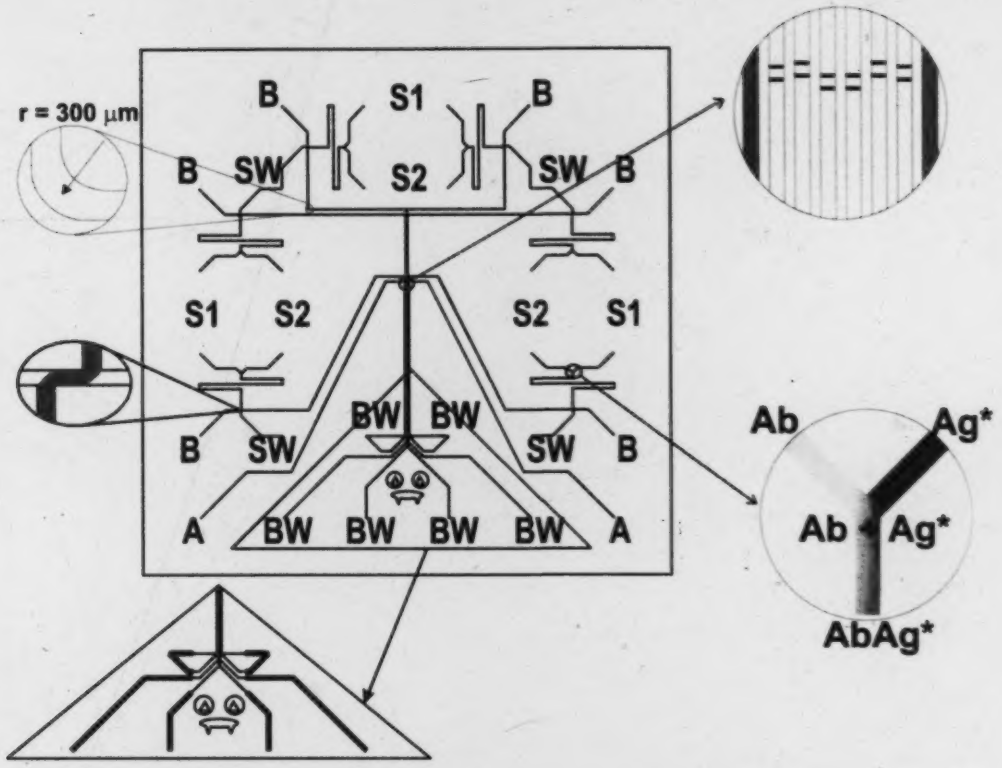


Figure 4.1. The overall layout of the flow channel manifolds in the SPIDY device is illustrated. Each reaction cell has reservoirs for sample (S1), antibody (S2), sample injection waste (SW) and running buffer (B). Six reaction cells are replicated around the outside of the wafer. The expansion on the left illustrates the double-T injector design for loading sample from the reactor into the separation column. In the bottom right expansion, the antibody (Ab) and antigen (Ag) mixer in the reaction cell is illustrated. An expansion in the lower left illustrates the pattern of channels at the buffer waste (BW) reservoirs used during separations. The thicker lines identify channel segments that are 300 μm wide, while the thinner lines represent 50 μm wide segments. The expansion in the upper right of the detection zone, across which a laser beam is swept, illustrates a separation of two components in the six separation channels. Two optical alignment channels (A) filled with fluorescent dye sandwich the separation channels.

The double-T injector offset[18,19] was 100 μm. The electrical resistances of all separation channels were made equal by varying the width and length of the channel near the buffer waste (BW),[15] as suggested at the bottom left of Figure 4.1. Each separation channel of 9.3 cm equivalent length meandered around 2-3 corners in order to fit onto the substrate. The corners in the separation channels were rounded, with a 300 μm radius of curvature to minimize sample plug distortion, as illustrated by the expanded view in the top left of Figure 4.1.[20] The detector was located either 5.0 or 7.5 cm downstream of the injector. The distance between the buffer reservoir and the injector was 0.7 cm. Channels were 50

μm wide (300 μm near BW) and 10 μm deep. The center to center distance between channels was 100 μm in the detection zone. Devices were fabricated in 4 x 4 inch square, 600 μm thick, Corning 0211 glass by the Alberta Microelectronic Corp., as previously described.[21,22] Top plates into which 2 mm access holes were drilled, were vigorously cleaned[9] then thermally bonded to the etched plate at 600° C for 6 hours, using the temperature ramp described previously.[22]

### 4.2.2 Materials and Reagents

Three buffer systems, namely tris(hydroxymethyl)aminomethane (Tris), tricine, and borate buffers, were used for the variety of experiments performed on SPIDY. All solutions were prepared using ultra pure water (Millipore Canada, Mississauga, ON), and were filtered with 0.2 μm Nylon-66 membrane filters (Fisher, Edmonton, AB). Protein solutions were not filtered. The Tris/Boric buffer, made up of 50 mM Tris and 50 mM boric acid, adjusted to pH 8.0 or pH 8.5 with NaOH was used in the fluorescein studies. For the measurement of channel resistance 10 mM KCl was added to the 50 mM Tris/Boric buffer. A buffer of 50 mM tricine with 0.01% v/v Tween 20 (Aldrich, Mississauga, ON) adjusted to pH 8.0 with 1 M NaOH[9] was used for the ovalbumin (Ov) assay, while the estradiol assay utilized a 10 mM, pH 8.2 borate buffer with 0.01% v/v Tween 20. Fluorescein, Ov and monoclonal anti-Ov were from Sigma (Mississauga, ON), while the bifunctional Cy-5 dye used to label the anti-Ov was from Amersham (Pittsburgh, PA). Non-reactive Cy-5 was from a Beckman (Fullerton, CA) calibration kit. Fluorescein labeled estradiol and its antibody were prepared at bioMérieux. PDMS or poly(dimethylsiloxane) (Sylgard 184 silicone elastomer kit) was from Dow Corning Corporation (Midland, MI). The printed circuit board used for the voltage interface to the chip was prepared using a Model 416-K Student PC Board kit (M.G. Chemicals, Etobicoke, ON).

### 4.2.3 Detection and Control System

The laser induced fluorescence (LIF) detection scheme, illustrated in Figure 4.2 was designed by Cameron Skinner. It utilized a galvano-scanner (Model 6810P Galvanometer Optical Scanner and Series 650X Mirror Positioning System, Cambridge

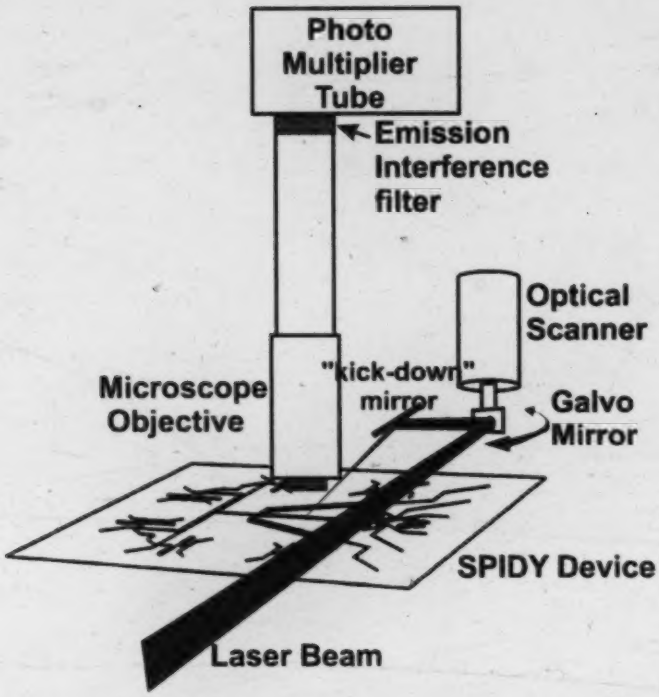


Figure 4.2 A schematic of the laser induced fluorescence detection scheme for SPIDY is shown. Signal was observed with a single point PMT detector, and the laser beam was rastered across the chip channels with a mirror mounted on a galvano-scanner. The rotation of the galvo mirror to create the raster is indicated by the curved arrow. The rastered detection zone is indicated by the upper right inset to Figure 4.1. A kickdown mirror directed the beam onto the channel at an angle of 50-65°.

Technology, Inc.) to step a mirror from channel to channel, collecting and summing 10 data points at 800 Hz before stepping to the next channel. The laser beam was expanded with a two lens telescope in order to fill the aperture of the 20 cm focal length, 1" diam. quartz lens (Newport) used to focus the beam to a 30 μm by 80-100 μm elliptical spot within the channels. The elliptical shape was generated by the use of a "kickdown" mirror mounted after the scanning mirror to create a 50-65° angle of incidence of the beam from the chip's surface normal. The beam was aligned so that the long axis of the spot ran parallel to the separation channel, in order to minimize scattered light from the channel edges. The fluorescence was collected with a 10X Rolyn Optics microscope objective (numerical aperture 0.3, working distance 7 mm), and focussed onto a Hamamatsu R1477 photomultiplier tube (PMT). A homebuilt $10^7$ gain transimpedance amplifier with a 360 Hz bandwidth was used for PMT amplification. A 633 nm He-Ne

laser (5 mW, Melles Griot) was used for the Ov assay and Cy-5 study, with an Omega 682DF22 bandpass filter. For the estradiol and fluorescein studies, a 10 mW Uniphase-Cyonics, 488 nm, air cooled Ar ion laser (Model 2214-10SL from Newport, Mississauga, ON) was operated at 4 mW output and a neutral density filter delivered 30% of the power to the excitation system. With this laser two Omega 530DF30 bandpass filters (Omega, Brattelboro, VT) were used to eliminate the scattered laser line.

A LabVIEW program, written by Cameron Skinner, running on a Pentium 166 IBM compatible computer with two laboratory interface boards (Model PC-1200 and PC-AO-2DC, National Instrument) was used to control the power supplies, relays and galvano-scanner system. The power supplies and relays have been described elsewhere.[19,23] The system is constructed to permit the simultaneous control of the laser beam position, an Iotech control 488/16 (Cleveland, OH) interface for control of the high voltage relays, the output of the power supplies, and acquisition of data from a PMT. While the Iotech and relays are controlled by the digital I/O on the PC-1200, the PC-AO-2DC digital I/O controlled the galvano-scanner (galvo). The galvo drive board accepts a 16 bit word and converts this word into a voltage with an on-board DAC which gives the galvo 64000 possible positions. To maintain a constant temperature (manufacturer recommends below 50°C), and to provide a solid mount, the galvo was mounted in an aluminum block attached to a 1" diam. stainless steel rod. A temperature sensor placed in the block sent back temperature measurements to the A/D input on the PC1200. In practice, the temperature rise was about 1-3 °C. The PC-1200 board provided two D/A converters for computer control of a +15 and a +3 kV high voltage power supplies. Caution: high voltages systems can be lethal. Care must be taken to avoid touching any live leads. Limiting the power supply current to 100 µA range also reduces the dangers.

### 4.2.4 Operating Procedures

During mixing and double-T injector loading a positive, high voltage (+HV) supply was applied to sample 1 (S1) and sample 2 (S2) reservoirs, while sample waste (SW) was at ground.[9] During this step plug shaping was occasionally utilized by applying 300 V on the buffer (B) and buffer waste (BW).[19] Larger injection plugs were formed in some cases, using a single-T loading mode, with +HV on S1 and S2, and BW at ground. In all

cases, separation was performed with +HV on B and ground on BW. BW was kept below 300 V to avoid arcing to the kickdown mirror and the galvo, which sat close to BW.

For the study of non-reactive Cy-5 standards, +HV was set to 3 kV during the 10 s double-T injector loading and 7 kV during separation. A 50 mM tricine buffer was used and Cy-5 was placed in both S1 and S2. The total current in the 8 channels was about 50 μA during separation. For the Ov assay a 5 s double-T loading sequence with +HV set to 2 kV was followed by a 1 s single-T loading with +HV set to 4 kV. Separation was performed in 50 mM Tricine buffer, with +HV set to 5 kV, giving 50 μA of total current. The fluorescein measurements were performed using a 5 s double-T loading with +HV set to 3 kV, fluorescein in both S1 and S2, and a plug shaping voltage of 300 V. Separation was performed with +HV set to 8 kV, giving a total current of 10 μA when using the 50 mM Tris/borate buffer. The anti-estradiol assay used a 10 s double-T loading step with +HV set to 3 kV, and 300 V for plug shaping. Separation was performed as for the fluorescein study.

SPIDY was flushed with 0.1 M NaOH prior to each sequence of experiments. Initially, NaOH was loaded into each channel and allowed to sit for 5-60 min, then water and running buffer were used to flush the channels. In order to optimize the quantitative performance of the device the following procedure was ultimately developed. With NaOH loaded into all reservoirs, vacuum was applied to the BW reservoir of each channel sequentially, and then to S1 of each manifold. All channels were then rinsed with buffer in the same fashion. Typical NaOH flushing times for the BW reservoirs were 30 min, with 10 min at S1. The buffer flushing time was 10 min. at BW and 5 min. at S1. Upon completion of a sequence of experiments, SPIDY was flushed with $H_2O$ for 10 min. at BW and 5 min at S1, followed by 0.1 M NaOH for 30–60 min. at BW and 20 min at S1. The device was stored in a high humidity environment (a sealed box with a pool of water inside) to prevent the channels from drying out.

The resistance of the channels was measured with a Fluke 87 III true-rms multimeter. Data was recorded as conductivity, and was averaged over 2 min for each point.

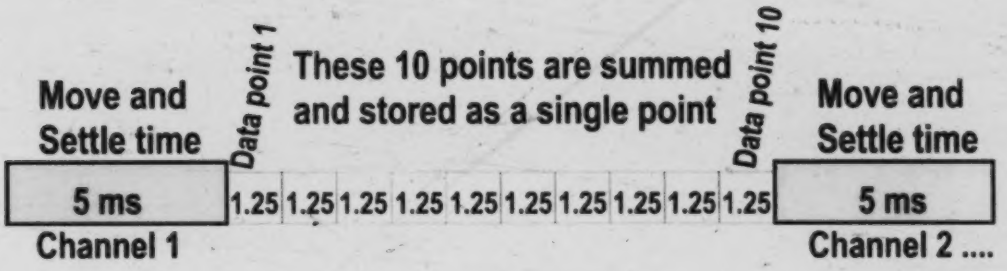
Move and Settle time
Data point 1
These 10 points are summed and stored as a single point
Data point 10
Move and Settle time
5 ms
1.25 1.25 1.25 1.25 1.25 1.25 1.25 1.25 1.25 1.25
5 ms
Channel 1
Channel 2 ....

Figure 4.3 The LabVIEW programmed timing and data acquisition process for one channel is illustrated. A software settling time of about 5 ms is followed by ten data points acquisition of 1.25 ms each. The data were summed and recorded as a single data point. The galvo mirror was then moved to the next channel and the process is repeated.

## 4.3 Results and Discussion

### 4.3.1 Detector Design

Mathies,[6,7,24] and more recently Landers,[5] have selected a single point detector design for multi-channel CE devices. Such a scheme is simpler to implement than a multi-point detector, since it minimizes many of the alignment issues that arise if one uses multiple beams[25] and multiple detectors. However, this scheme does force the fluid channel layout to bring all the separation channels to a common location.[5,6,24] For simplicity, our first design also utilized a single point detector, as shown in the scheme in Figure 4.2. A galvano-scanner was selected to raster the laser beam across the detection channels,[24] because the alternative of translating the chip back and forth under a fixed beam would not have allowed a sufficiently rapid sampling rate per channel.[5,6] A two-lens arrangement was selected,[21,23] rather than epiluminescent optics, due to the decreased complexity of rastering the beam in the two lens design.

The galvano-scanner hardware operates in a feedback loop that minimizes the difference between the actual scanner position and the user defined position. To the user, the scanner behaves very much like a stepper motor, allowing rapid transitions between positions (channels) with long dwell times within each channel. The LabVIEW software overhead resulted in a settling time of about 5 ms for each step between channels, although the hardware limitation was only 0.5 ms. An integration period of 12.5 ms per channel was selected (a 71% duty cycle) with 10 data points measured and summed at a frequency of 800 Hz (i.e. the A/D conversion frequency) for each channel. Figure 4.3 illustrates this timing and data acquisition process. Stepping the beam between channels

every 17.5 ms (57 Hz cross-channel read frequency for an 8-channel scan) meant that the 25 Hz low pass filter we employed previously for single channel detection was unacceptable, because it caused cross talk between channel readings. Consequently, summing was performed to reduce high frequency noise, given the 360 Hz bandwidth employed with the transimpedance amplifier. The data stream was saved in a 9 x n matrix, with 8 columns for n-data points per channel, and a ninth column to store the time of acquisition of channel 1. Each channel's data was further smoothed with an 11-point Savitzky-Golay smoothing function.

The 57 Hz cross-channel read frequency meant each of the 8 channels was read at a rate of 7.1 Hz, which was adequate for the relatively wide peaks (~1 s) observed in ACE. With the use of more efficient software, the hardware limitation would dictate a minimum time per channel reading frame of about 1 ms with a 50% duty cycle. (Continuing to sum 10 readings per data point would then require 10 kHz A/D conversion). This dwell time means a maximum read rate per channel of 125 Hz would be possible for the 8-channel SPIDY device. Alternatively, at a read rate of 7.1 Hz for each channel, a total of 140 channels could conceivably be measured. Thus, considering the relatively broad peaks observed in protein separations, the galvano-scanner appears to provide adequate measurement speed for chips with large channel multiplicity, allowing a duty cycle of at least 50%. The field of view of the objective lens and the PMT limit our current design to about 16 channels. However, reducing the spacing between channels to 25 µm would increase this to 32, and lenses with larger fields of view are available.[24]

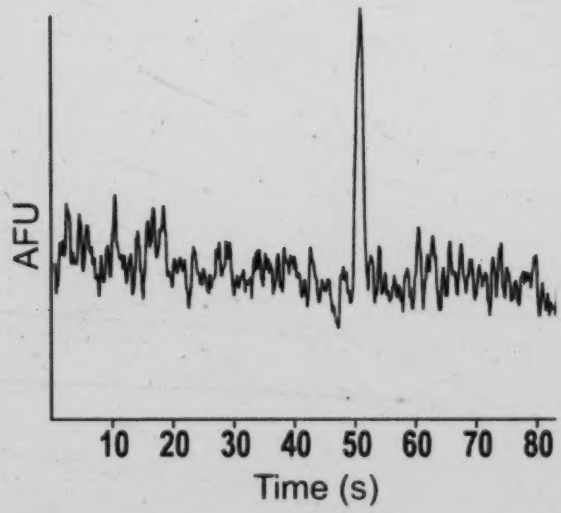


Figure 4.4 The signal observed with the scanning detector design is shown for injection of a 100 pM fluorescein sample in 50 mM Tris/Boric buffer. A double-T injection was performed at 2 kV for 8 s, followed by 3 s of single-T injection at 2 kV and separation at 5 kV over an 8 cm injector to detector distance.

Scattered light from the laser constitutes the largest source of background for LIF detection. The use of two 530 nm bandpass filters helped to reduce the background. A 0.5 mm slit was also used to reduce scatter for the detection limit study. Figure 4.4 shows the detector performance for fluorescein at 100 pM (data were collected by Cameron Skinner). The multi-channel detector afforded a 30 pM detection limit for fluorescein, which compares favorably with the 10 pM detection limit we reported for a single channel detector design based on similar excitation and emission optics.[9] When using only a single filter, without the slit, the detection limit of the multi-channel system was in the range of 200-300 pM. The stepping function of the galvano-scanner proved quite stable. Once aligned to channel 1 and channel 8, no further adjustment of the step size or positioning was required during 8-12 h of use.

### 4.3.2 Multi-Channel Layout

We decided to create six independent assay manifolds, so that the device could be used to perform either 6 independent assays on one sample, or one assay on 6 samples. The SPIDY layout eventually selected, shown in Figure 4.1, is the result of the considerations outlined below.

To simplify the layout of the reaction cells, which contained the mixer, reactor and injector functions, they were drafted as a single unit cell that was then replicated six times. It was decided to arrange all of the access reservoirs in a unit cell of 4, which was replicated around the outside of the layout. The access pattern was arranged to leave the central region of the layout clear for optical access, as indicated in Figure 4.5. The reaction cell was organized so that the potentials applied to adjacent reservoirs in the reservoir unit cells would not differ by more than 3 kV. In order to meet these requirements some of the access reservoirs contacted more than one assay manifold. Within the reaction cell the mixer was designed to bring two flow channels together at a 45 degree angle.[26] The downstream channel width of 50 μm was set equal to the upstream width, in order to maintain a short diffusion distance across the channel for rapid mixing.[9] The mixer length of 39 mm was long enough to allow complete diffusion of a small molecule ($D > 1 \times 10^{6}$ $cm^2/s$) across the channel under continuous flow conditions (assuming a linear velocity of 1-3 mm/s).[9] However, we anticipated stopping

Figure 4.5 A photograph of the printed circuit board (PCB) electrical interface is shown mounted on top of a SPIDY device. A PDMS coating was applied over the top of the PCB. The reservoirs, mounted on the chip over the access holes, pass through ports in the PCB into which the Pt wire contacts are seen hanging. The central region of the chip is exposed through the cut out in the center of the PCB. The cut out was formed to allow optical access to the detection zone on the wafer.

the flow after mixing to allow the reaction to proceed, so the channel length was simply made long enough to ensure there was enough volume (~16 nL) for injection of replicate reacted samples for separation. This stopped flow regime occurs naturally since reactants are allowed to mix and react during the separation of the preceding sample.[16] The double-T injector was based on the previous design,[9] which we knew to be effective.[19] Since some rotation of the design was required around the wafer, we ensured that the channels intersected at 90° and were straight for at least 1 mm (> 10 channel widths) before the intersection. Because the ends of each channel were widened to 300 µm, the challenge of aligning with the access holes in the cover plate was reduced.

The choice of a scanned detector implies that the separation channels run parallel in the detector zone, but the large size selected for the reactor manifolds prevents a close packed arrangement. Thus the separation channels could be neither identical in length nor straight. However, obtaining uniform performance between channels requires that they each have the same electrical impedance,[27] and that the distance from injector to detector be the same. Consequently, the lengths of the 300 µm wide channel segments at

the entrance and exit of the separation channels were adjusted to ensure the total impedance from the buffer to the separation waste reservoirs would be equal.[27] In retrospect, it would have been preferable to adjust both the length and width of those segments so that the potential drop along the narrow segment of the separation channel was equal between all channels. In the present design the impedance of the total lengths were matched, but the impedance of the narrow separation channel segments differed slightly. The separation channels were brought together in the detection zone. The walls between the channels were 50 µm thick at the surface of the wafer. This width was selected in order to minimize the distance the laser was scanned, while ensuring that small defects in the channel walls formed during fabrication would not short the channels together.

Since sharp corners in the separation path can cause considerable band broadening due to the non-uniform path length and non-uniform electric field lines, the number of corners was minimized.[20] Large electric field gradients at corners were reduced by designing the corner as a series of segments, making an arc, rather than an abrupt single turn. Eleven segments, each about 47 µm in length, were formed to create a 90° turn, giving a 300 µm turning radius while the 70° turn in the layout used 8 segments of about the same length. The constraints of the L-Edit design software made it difficult to use identical lengths and angles for each segment, but the differences between segments was less than 5%. After etching the glass, the corners look like smooth curves, as suggested by the top left insert in Figure 4.1.

### 4.3.3 Electrical Interface

Increasing the number of channels means that the commonly used electrical interface to a single manifold chip[21,23,26] becomes cumbersome.[24] In addition to the much larger number of Pt electrodes and wires required to supply voltages to the reservoirs, many more reservoirs need to remain accessible for the purpose of changing sample solutions. The first generation of electrical interface for SPIDY, as designed by Cameron Skinner and shown in Figure 4.6, utilized an acrylic plate, to which Pt electrodes and connecting wiring were glued in a 16 x 16 mm grid. This assembly was placed directly on top of the SPIDY device. All the Pt electrodes of common voltage were connected together with

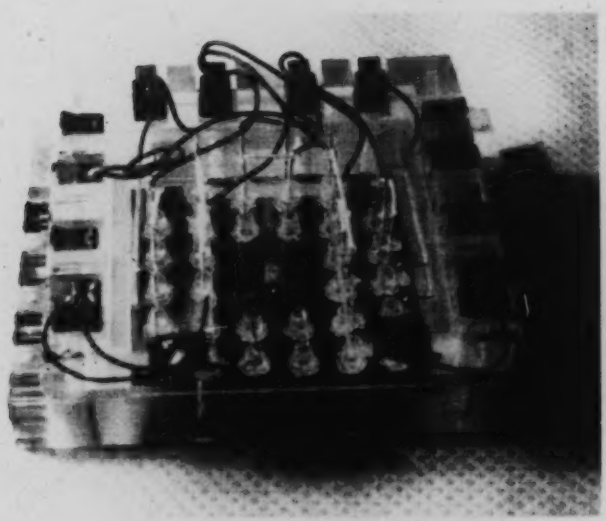

Figure 4.6 A photograph of an electrical interface for SPIDY mounted on a device holder. An acrylic plate to which 30 hanging Pt electrodes were glued in a 16 x 16 mm grid was shown. Some of the Pt electrodes can be seen making contact to the reservoirs of a SPIDY device placed in the device holder. Wire connections were made on top of the acrylic plate.

copper wires on top of the acrylic plate. This interface hinders access to the reservoirs on SPIDY, making it awkward to exchange sample solutions, since the detector must also be moved in order to remove the wiring harness. In addition, larger reservoirs were needed for ease of alignment of the 30 Pt electrodes to the reservoirs. This approach works well for a single use chip that may be loaded with sample before making electrical contact, but is poor for a multi-use chip into which new samples must repeatedly be introduced.

An alternate approach to the contact plate design described above was undertaken, in order to provide ready access to the device. After considerable trial and error with hand made wiring harnesses we selected a printed circuit board (PCB) approach to route the high voltage wiring, illustrated in Figure 4.5. Electrical circuits required to connect common voltage points were printed on a PCB, while access holes were made in the board to allow clearance of the plastic reservoirs glued onto the chip. Pt wires were then soldered onto the PCB to make electrical contact with the SPIDY device. The PCB was then coated with several layers of PDMS to prevent arcing when high voltages were applied. Besides allowing access to reservoirs, this electrical interface is reusable and very rugged, which makes up for the fact that it lacks flexibility in terms of the circuit configuration.

### 4.3.4 Qualitative Analysis

Initial trials with SPIDY showed a significant range of migration times, from 74 to 94 s, between channels for Cy-5 dye as demonstrated in Figure 4.7. Peak heights also varied significantly between channels (± 67%). However, within a given channel, migration times showed less than ± 0.5% variation, and peak heights varied by less than ± 5%. Figure 4.8 shows electropherograms for five consecutive runs of a hydrolyzed bifunctional Cy-5 dye overlaid one on top of the other, indicating little run to run variation within a channel. Despite the initial channel-to-channel variations, qualitative analysis of various solutions of Ov and Cy-5 labeled anti-Ov (Ab*) could be performed in a multi-channel mode. For example, Figure 4.9 shows results obtained simultaneously on SPIDY for a direct Ov assay, running standards and sample in parallel. Three channels were loaded with standard solutions prepared by mixing Ov and Ab* off-chip. One channel ran a Cy-5 labeled Ov standard, and two channels contained Ov and Ab* samples in separate sample reservoirs for on-chip mixing, reaction and separation. The

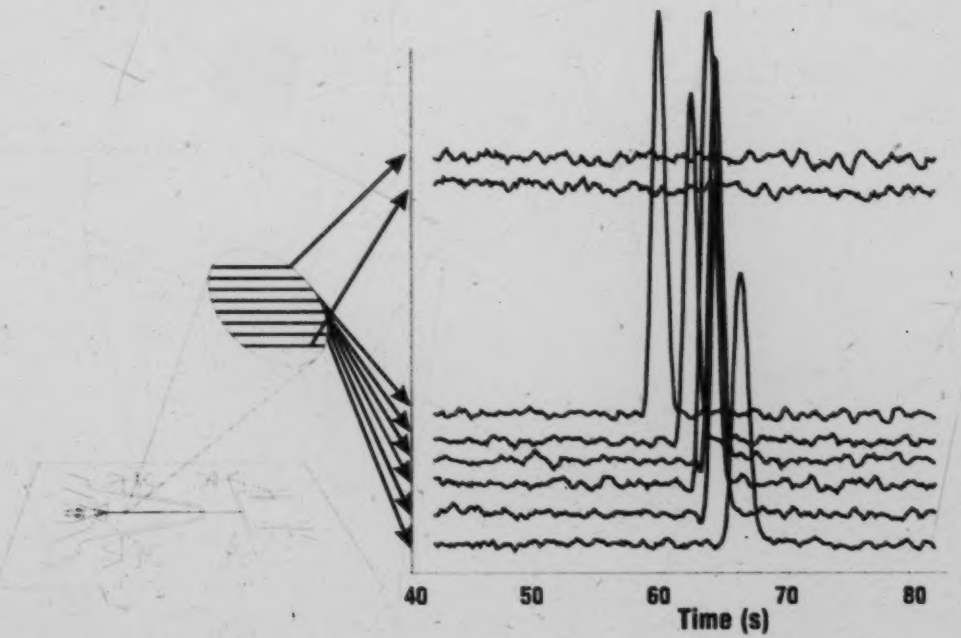


Figure 4.7 A schematic illustrates the simultaneous collection of electropherograms from SPIDY during a preliminary experiment using standard Cy-5 dye. Significant variation of migration times (60 – 67 s) and peak heights (± 67% ) were observed prior to optimizing the EOF performance.

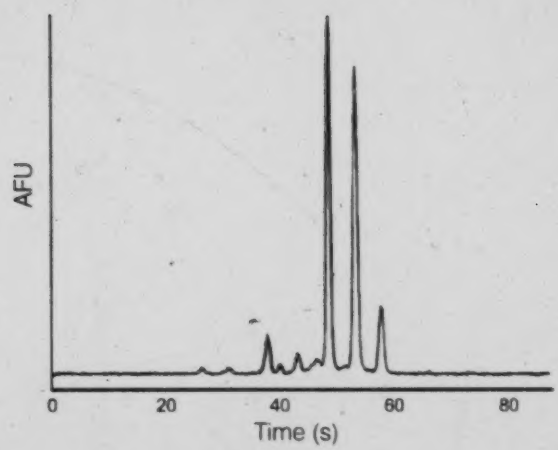


Figure 4.8 Electropherograms of five consecutive runs of a hydrolyzed bifunctional Cy-5 dye from a single channel is shown. Good reproducibility for both the migration times (± 0.5%) and peak height (± 5%) are observed.

Ab*-Ov complex could be resolved from Ab*, allowing a direct assay for Ov. The results obtained in the lower two traces in Figure 4.9 for on-chip mixing demonstrated that integration of simultaneous on-chip mixing, reaction and separation of sample and antibody is possible. The peak height reproducibility within any given channel manifold was ± 5% for the Ov assay, allowing individual channels to be calibrated separately. However, the variability between channels illustrated by the differences between the top two traces in Figure 4.9, which contained the same standard solution, meant that cross-channel calibration was not possible.

The variation between channels in SPIDY was surprising, since with proper conditioning procedures we observed migration time and peak height variations of less than ± 3% between different wafers etched with a single channel immunoassay manifold.[16] Upon reflection, we realized that the single channel chip performance was obtained by first independently optimizing the operation parameters for each chip, such as the voltages applied for injection plug shaping. In contrast, the multi-channel device was designed to be controlled with only one set of power supplies, and hence one set of operating conditions. Fine-tuning for individual channels demands a large number of individual control lines, and the time spent optimizing each channel could easily become excessive, making it preferable to make the manifolds behave more uniformly.

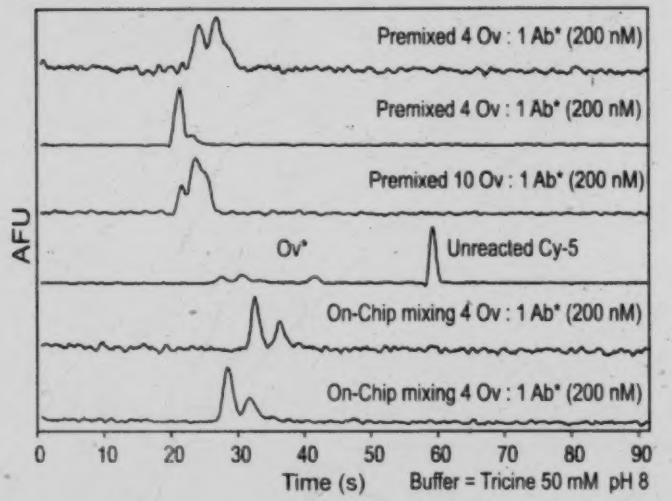
Premixed 4 Ov : 1 Ab* (200 nM)
Premixed 4 Ov : 1 Ab* (200 nM)
Premixed 10 Ov : 1 Ab* (200 nM)
Ov*
Unreacted Cy-5
On-Chip mixing 4 Ov : 1 Ab* (200 nM)
On-Chip mixing 4 Ov : 1 Ab* (200 nM)
AFU
0 10 20 30 40 50 60 70 80 90
Time (s)
Buffer = Tricine 50 mM pH 8

Figure 4.9 Six electropherograms obtained simultaneously in SPIDY are shown for several different solutions in the six immunoassay channels. The top two traces are for a mixture, prepared off-chip, of 4:1 molar ratios of ovalbumin (Ov, 800 nM) to labeled anti-Ov (Ab*, 200 nM). The third trace is for a 10:1 ratio of Ov (2 μM) to Ab* (200 nM). The fourth trace shows an external standard of hydrolyzed Cy-5 labeling agent and labeled Ov. The bottom two traces show replicate channels in which 400 nM sample Ov was mixed with 200 nM Ab* on-chip. Experiments were performed in 50 mM Tricine buffer, using a single-T injection procedure, with 633 nm fluorescence excitation, as described in the Experimental Section. Data were obtained before optimizing the electroosmotic flow performance.

### 4.3.5 Factors Required for Uniform Analytical Behavior

Variations in electrical impedance of each channel, and in the surface chemistry of each channel were thought to be the likely source of the observed variation.[27] A sequence of studies was performed to examine this hypothesis, and to establish methods to obtain uniform, reproducible surfaces. SPIDY was designed with equal electrical impedance for each of the manifolds. However, variations in channel etching across a wafer and imperfect alignment of access holes to each channel may cause individual channel impedances to differ from the nominal value. Table 4.1 provides the measured impedances of all channels. The results show a relatively minor variation across the various channels, allowing us to conclude that these differences are not the primary source of experimental variation. A more complex issue is the surface charge on the glass walls,[28] which depends in part on the history of the surface. Exposure to photoresist, solvents, and etchants during device fabrication can leave residues on a glass surface, and these may not be evenly distributed across a wafer. Protein adsorption on to

| Channel Segment[a] | Resistance (GΩ)[b] |
|---|---|
| Channel 1 B-BW | 0.96 ± 0.01 |
| Channel 2 B-BW | 0.952 ± 0.004 |
| Channel 3 B-BW | 1.00 ± 0.03 |
| Channel 4 B-BW | 1.06 ± 0.01 |
| Channel 5 B-BW | 1.05 ± 0.01 |
| Channel 6 B-BW | 1.19 ± 0.01 |
| Channel 7 B-BW | 1.046 ± 0.001 |
| Channel 8 B-BW | 1.060 ± 0.004 |
| Channel 2 S1-SW | 0.70 ± 0.09 |
| Channel 2 S2-SW | 0.68 ± 0.07 |
| Channel 7 S1-SW | 0.67 ± 0.05 |
| Channel 7 S2-SW | 0.66 ± 0.03 |

Table 4.1 Measured Impedance of Channel Segments within SPIDY
[a]Letters refer to reservoir names as identified in Figure 4.1. Numbers refer to reaction cells, counting from 2 for the reaction cell at bottom left in Figure 4.1.
[b]Resistances were measured with pH 8.5, 50 mM Tris/Boric and 10 mM KCl buffer as electrolyte. Errors are the standard deviation in 3-5 replicates.

channel walls during use also causes non-uniformity between channels. Variation in surface charge causes a variation in the electroosmotic flow (EOF) that acts as a pump for the device.[27,28] As demonstrated below, this variation was found to be significant unless careful attention was paid to preparation of the channels.

The double-T injector within the reaction cell plays an important role in determining the sample plug size and thus the overall quality of a standard calibration. Since the voltage applied to perform injection is the same for all channels, differences in surface charge in the mixer, reactor and/or injector can cause slight differences in EOF flow between channels, leading to differing amounts of sample being injected in different channels. Figure 4.10 shows the observed behavior of two channels in a device used for several months, which exhibited a large channel-to-channel variation. Using a 2.5 kV injection voltage with 300 V plug shaping for 6 s, the two channels showed drastic differences in the amount of the fluorescein labeled estradiol sample injected. When the injection time was 5 s or less, no peak was observed for manifold 7. The electrical impedances measured between S1/S2 and SW for both manifold 2 and 7 were similar, as

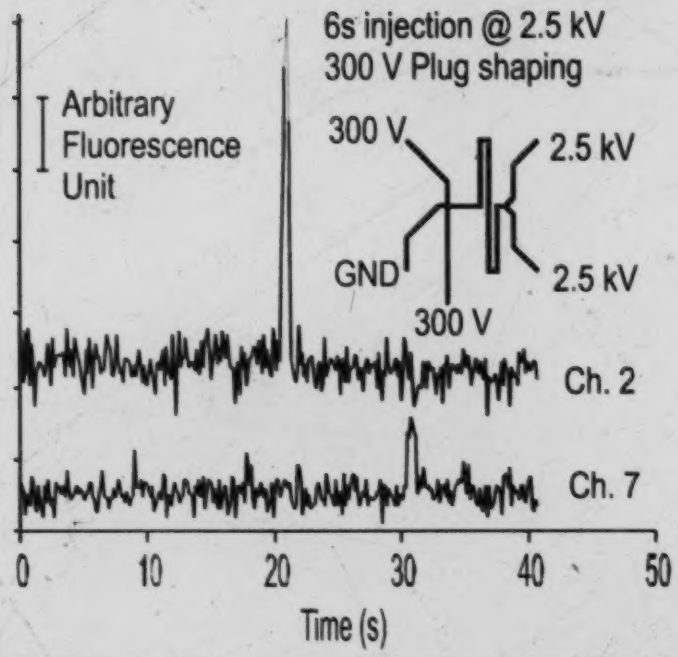


Figure 4.10 Comparison of injection performance of reaction cells 2 and 7 for labeled estradiol in a device that had been used for several months, which exhibited extreme differences in channel to channel behavior. The double-T injection used 2.5 kV for 6 s with 300 V plug shaping, followed by separation at 8 kV.

shown in Table 4.1. Thus the behavior observed must be due to differences in EOF in the two manifolds. To evaluate the EOF difference between the two channel's injection manifolds, the setup illustrated in the inset of Figure 4.11 was used. The sample reservoirs S1 and S2 were filled with labeled estradiol and buffer respectively. A voltage of 2 kV was applied between S1 and SW to create a sample plug of dye in the mixing channel, then 2 kV was applied between S2 and SW. Figure 4.11 shows the resulting migration times observed for the dye to reach the detector in reaction cells 2 and 7. The results confirm that EOF was significantly different between the two reaction cell manifolds. These observations represent an extreme example of EOF differences resulting from several months of device usage, whereas with new devices the differences are much smaller. Nevertheless, the effect of variations in the EOF between manifolds on cross manifold injection reproducibility is made obvious by this study.

Flushing with 0.1 M NaOH for at least 30 minutes per channel and working with low concentrations of protein can reduce sample and "aging" effects on EOF. The initial wetting procedures employed also proved to be key to good performance and longevity

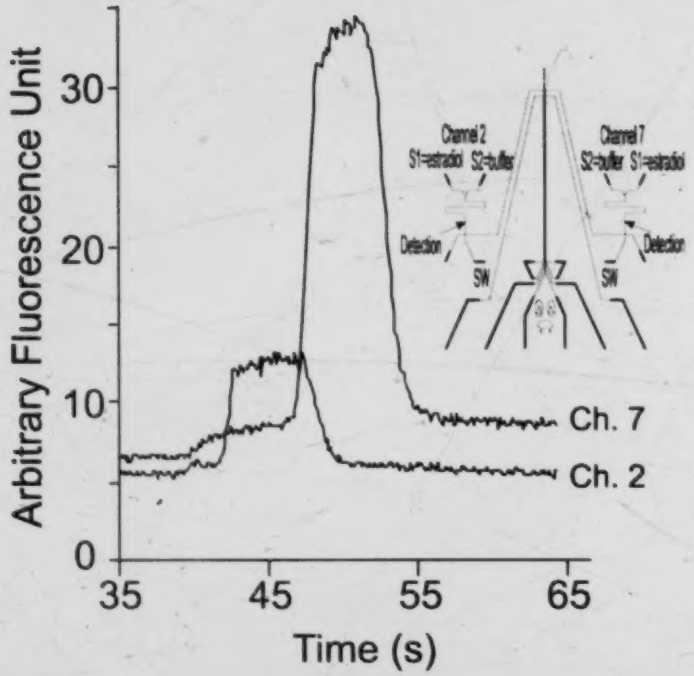


Figure 4.11 Comparison of the difference in migration time between the same two reaction cells compared in Figure 4.10. A detector was located near the intersection between the reaction and separation channels, as illustrated in the inset, in order to measure the flow rate of dye through the mixer. Flow from S1 (buffer) and S2 (fluorescein) was alternated in order to create a sample plug to allow a velocity determination.

of the device. A typical procedure for wetting a new device started with doubly distilled water (dd$H_2O$), followed by 0.1 M NaOH. However, if air bubbles were trapped, an organic solvent such as methanol or acetone was used, resulting in slightly different channel surfaces, as evidenced by a 52-72 s range in fluorescein migration times (8 cm injector-detector distance). An alternate wetting procedure that started with methanol, followed by dd $H_2O$ and 0.1 M NaOH was found to increase the uniformity among channels and decrease migration times, to a range of 27-33 s (8 cm injector-detector distance). With the present layout, flushing one channel at a time with NaOH, as described in the Section 4.2.4, proved to be tedious, since each manifold was well cleaned only when it was separately flushed. Attempts to flush several channels simultaneously using a vacuum source resulted in non-uniform flow rates, which then resulted in different surface charges and EOF in each manifold. In future designs, a

manifold that allows easy coupling of all channels to a NaOH source and that ensures similar flow rates in all channels would be beneficial.

Voltage controlled plug shaping[19] was found to be effective for improving the channel-to-channel reproducibility, once a more uniform surface treatment was established. Typically, 3 kV was applied to S1 and S2, and ground to SW, while 300 V was applied to the side channels B and BW was found to be optimal for shaping the plugs during mixing, reaction and injector loading. During optimization of plug shaping, voltages on S1 and S2 relative to SW were stepped in 100 V increments. A value of 200 V resulted in poor reproducibility between runs, while 400 V resulted in no injection in some channels. During separation, 7 or 8 kV was applied between B and BW, but a pushback voltage[8,19] to prevent leakage from the injector manifold was not used, since the background observed remained low without the use of pushback. These procedural changes in plug shaping and surface preparation allowed us to perform both independent channel and cross-channel calibration (vide infra).

### 4.3.6 Quantitative Analysis

Using the surface pretreatment and plug shaping procedures described above, we calibrated each manifold on SPIDY simultaneously using fluorescein standards. Figure 4.12 shows fluorescein calibration (3 to 200 nM) results, with $R^2$ ranging from 0.971 to 0.999 for each channel. Each channel ran the same concentration simultaneously. The results demonstrated a much better quantitative measurement than our previous attempts. For freshly prepared wafers, the plug shaping step was not required, but after 4-6 h of use the peak area reproducibility was degraded unless plug shaping was used. For simultaneous quantitative on-chip immunoassay reactions, an anti-estradiol (anti-E2) immunoassay was used as a model system. Fluorescently tagged estradiol (E2) was present in excess at 128 nM, while its antibody was varied from 20 to 50 nM, giving an assay for the antibody. Figure 4.13 shows a typical simultaneous run during the calibration, in which the same anti-E2 concentration was present in each channel. The slightly faster migration time in channels 4 and 5 was due to a slightly shorter injector to detector distance compared to other channels. (To speed the separation, the separation distance was shortened to 5.0 cm by detecting upstream from buffer waste. The small

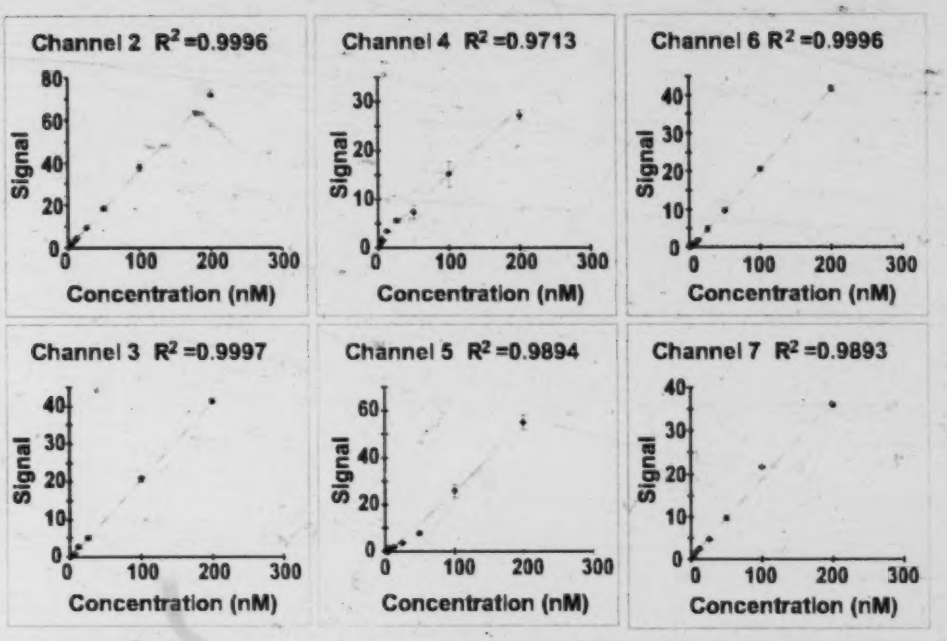


Figure 4.12 Calibration curves for 3-200 nM fluorescein in 50 mM Tris/Boric buffer, obtained in the six immunoassay channels of SPIDY after developing the optimized surface preparation protocol described in the Experimental Section. A given fluorescein sample was placed in both S1 and S2 of all six reaction cells and injected and detected simultaneously to develop the calibration curves. A double-T injection was performed with the use of plug shaping, as described in the Experimental Section.

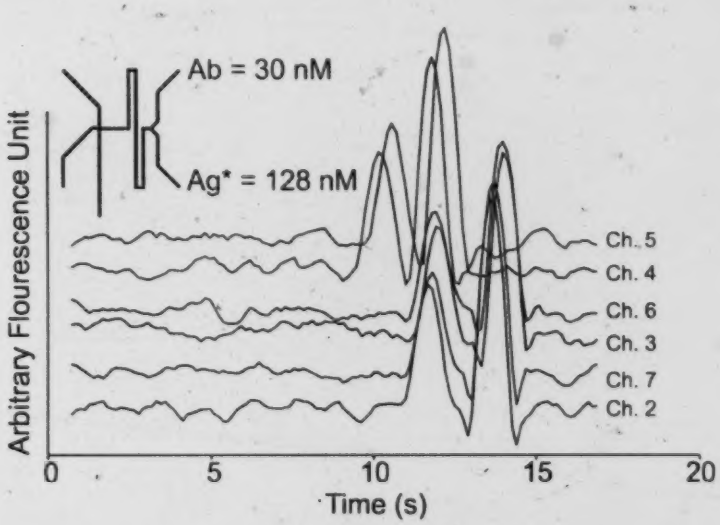


Figure 4.13 On-chip mixing, reaction and separation of 128 nM labeled estradiol (E2) and 30 nM anti-E2 performed in six channels simultaneously, obtained after developing the optimized surface preparation protocol. Channels which are mirror images in the layout are paired together for comparison. Details are given in the Experimental Section.

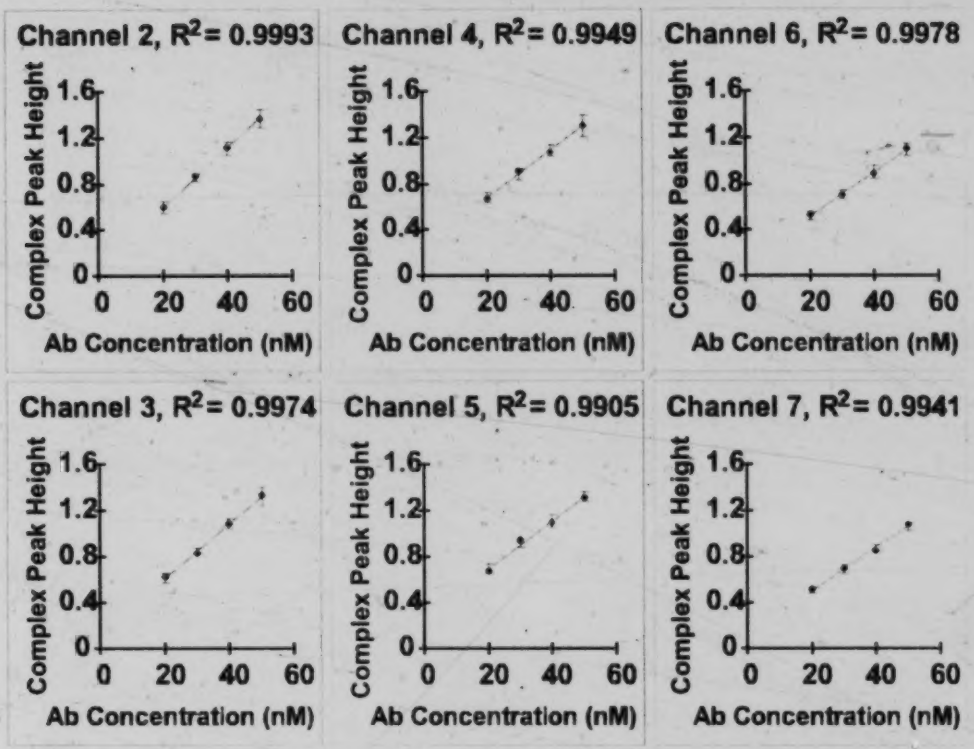


Figure 4.14 Calibration curves for 20-50 nM anti-E2 in 10 mM Borate buffer, obtained by on-chip mixing with 128 nM labeled E2 present in reservoir S2. A given anti-E2 sample was placed in reservoir S1 in all six reaction cells, then mixed, reacted, injected and detected simultaneously to develop the calibration curves. A double-T injection was performed with the use of plug shaping, as described in the text.

differences in separation channel length, and hence the electric field, were more obvious with the shorter length.) Calibration curves for the E2-Ab complex peak height versus concentration of Ab gave $R^2$ values between 0.990 and 0.999. The calibrations are shown in Figure 4.14 for each channel. The RSD for each peak height in the plots was in the range of 3-8% (n = 5). The results indicate we can quantitatively control mixing, reaction and separation in 6 channels simultaneously. The slopes of the calibration curves ranged from 0.019 to 0.025. We thus attempted to perform cross-channel calibrations. In this mode of operation, both calibration and sample measurements can be performed in a single simultaneous run, with standards and samples present at different concentrations in each channel. For the example shown in Figure 4.15, 20 nM anti-E2 was placed in reaction cells 3 and 6, 30 nM anti-E2 in cells 2 and 7, and 50 nM anti-E2

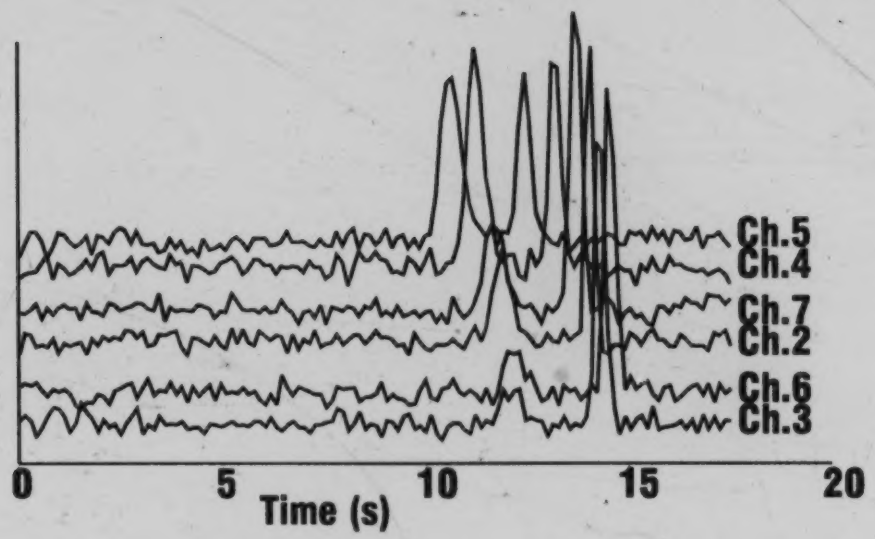


Figure 4.15 In addition to on-chip mixing, reaction and separation, an on-chip calibration of labeled estradiol (E2) and its antibody (anti-E2) is shown. 20, 30 and 50 nM of anti-E2 were reacted in channel pairs 3 and 6, 2 and 7, and 4 and 5 with 128 nM E2, respectively. Details were given in the text.

was placed in cells 4 and 5, with 128 nM E2 as the reagent in reservoirs S1 for all cells. The data from each reaction cell pair was averaged and the calibration curve obtained by averaging three replicate, simultaneous runs is shown in Figure 4.16. The RSD in peak height was 4-7% (n = 6). Since the separation for the anti-estradiol assay was completed in less than 20 s, while loading and reaction required 10 s, it is possible to obtain a calibrated data set for mixing, reaction and separation in 30 s. Three replicate measurements of sample and standards require less than 2 min for the entire analysis.

The limit of detection (LOD) obtained for anti-E2 from a calibration curve within a single channel run was 4.3 nM. For the cross-channel calibration the LOD was 6.4 nM. These results indicate the reproducibility from channel to channel could be made quite good. The slight increase in LOD caused by channel to channel variation is easily offset by the convenience and rapidity of simultaneously performing calibration and sample analysis. The absolute value of the LOD was controlled by the affinity constant for anti-E2 and the 128 nM concentration of labeled E2 we selected,[29] rather than by the instrument performance.

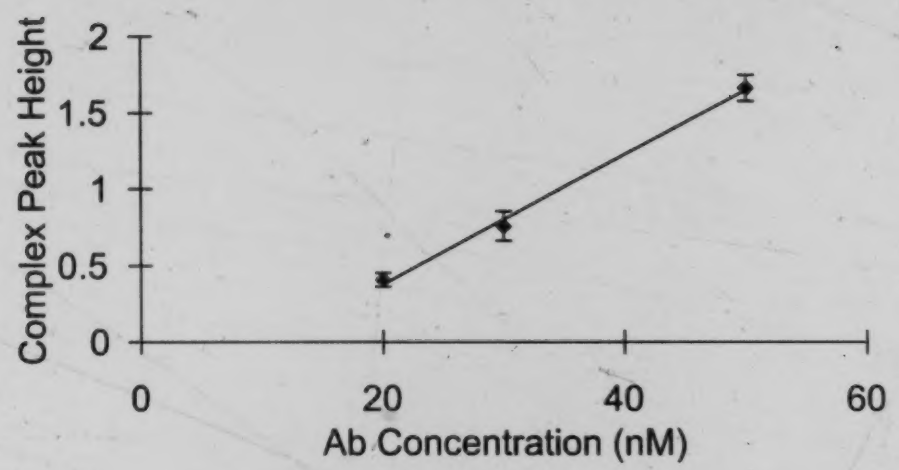


Figure 4.16 A cross-channel calibration curve for anti-E2, in which signals for three different concentrations of anti-E2 were determined simultaneously in the six channels, and the results of each pair of channels with the same concentration were averaged.

## 4.4 Conclusions

SPIDY has served as a prototype to allow us to explore the possibilities and discover the limitations of multi-channel devices. This work demonstrated the multiplexing of mixing and reaction steps in addition to injection and separation, showing that increased throughput can be achieved for more complex sample processing than DNA separations. We have also identified factors important for obtaining good quality, quantitative measurements within a multi-channel system. The demonstrated ability to obtain quantitative data by calibrating across channels is a very important step towards enhanced multiplexing and throughput, since standards can then be run simultaneously with samples. The importance of obtaining uniform electroosmotic flow behaviour between each manifold of a multi-channel device has been clearly identified as a critical element for good quantitative behaviour with cross manifold calibration procedures. However, if each manifold is separately calibrated, or quantitative analysis is not required, the demand for uniform EOF behaviour is greatly reduced. For multi-use devices our results make it clear that design of the multi-channel manifold to ensure rapid and easy interfacing to a flushing and cleaning system would be a major advantage. Nevertheless, we found that once an appropriate surface preparation procedure is applied it is possible to routinely prepare manifolds with similar EOF properties. The single point, rastered

detection scheme used here should be satisfactory for multiplexing designs up to a manifold number limited by the field of view of the detection optics, given the 1 s wide peaks typical of protein separations on chip. As the number of reaction and separation manifolds is increased beyond six, we anticipate the difficulty of obtaining uniform cross-manifold behaviour will not increase significantly. Instead, the increased complexity of the electrical and fluid interface design and the detection system will provide a more significant limitation in the ability to multiplex integrated reactor/separator designs.

## 4.5 References


1 Manz, A.; Graber, N.; Widmer, H.M. *Sensors and Actuators* **1990**, *B1*, 224-248.

2 Xue, Q.; Foret, F.; Dunayevskiy, Y.M.; Zavracky, P.M.; McGruer, N.E.; Karger, B.L. *Anal. Chem.* **1997**, *69*, 426.

3 Figeys, D.; Ning, Y.; Aebersold, R. *Anal. Chem.* **1997**, *69*, 3153-3160.

4 Figeys, D.; Aebersold, R. *Anal. Chem.* **1998**, *70*, 3721-3727.

5 Huang, Z.; Munro, N.; Hühmer, A.F.R.; Landers, J.P. *Anal. Chem.* **1999**, *71*, 5309-5314.

6 Woolley, A.T.; Sensabaugh, G.F.; Mathies, R.A. *Anal. Chem.* **1997**, *69*, 2181-2186.

7 Shi, Y.; Simpson, P.C.; Scherer, J.R.; Wexler, D.; Skibola, C.; Smith, M.T.; Mathies, R.A. *Anal. Chem.* **1999**, *71*, 5354-5361.

8 Jacobson, S.C.; Hergenröder, R.; Moore, A.W. Jr.; Ramsey, J.M. *Anal. Chem.* **1994**, *66*, 4127-4132.

9 Chiem, N.H.; Harrison, D.J. *Clinical Chemistry*, **1998**, *44:3*, 591-598.

10 Schultz, N.M.; Kennedy, R.T. *Anal Chem.* **1993**, *65*, 3161-3165.

11 Arentoft, A.M.; Frokiaer, H.; Michaelsen, S.; Sorensen, H.; Sorensen S. *J. Chromatogr., A.* **1993**, *652*, 189-198.

12 Shimura, K.; Karger, B.L. *Anal. Chem.* **1994**, *66*, 9-15.

13 Schmalzing, D.; Nashabeh, W. *Electrophoresis* **1997**, *18*, 2184-2193.

14 Rundlett, K.L.; Armstrong, D.W. *Electrophoresis* **1997**, *18*, 2194-2202.

15 Harrison, D.J.; Manz, A.; Fan, Z.; Lüdi, H.; Widmer, H.M. *Anal. Chem.* **1992**, *64*, 1926-1932.

16 Lee, W.E.; Jemere, A.B.; Attiya, S.; Chiem, N.H.; Paulson, M.; Ahrend, J.; Burchett, G.; Bader, D.E.; Ning, Y.; Harrison, D.J. *J. Cap. Elec. and Microchip Tech.* **1999,** *1/2,* 51-59.

17 Kohen, F.; De Boever, J.; Barnard, G. In *Immunoassay,* 1st ed.; Christopoulos, T.K., Diamandis, E.P., Eds.; Academic Press: San Diego, **1996,** 405-423.

18 Effenhauser, C.S.; Manz, A.; Widmer, H.M. *Anal. Chem.* **1993,** *65,* 2637-2642.

19 Shultz-Lockyear, L.L.; Colyer, C.L.; Fan, Z.H.; Roy, K.I.; Harrison, D.J. *Electrophoresis* **1999,** *20,* 529-538.

20 Culbertson, C.T.; Jacobson, S.C.; Ramsey, J. M. *Anal. Chem.* **1998,** *70,* 3781-3789.

21 Fan, Z.H.; Harrison, D.J. *Anal. Chem.* **1994,** *66,* 177-184.

22 Li, P.C.H.; Harrison, D.J. *Anal. Chem.* **1997,** *69,* 1564-1568.

23 Seiler, K.; Harrison, D.J.; Manz, A. *Anal. Chem.* **1993,** *65,* 1481-1488.

24 Simpson, P.C.; Roach, D.; Woolley, A.T.; Thorsen, T.; Johnston, R.; Sensabaugh, G.F.; Mathies, R.A. *Proc. Natl. Acad. Sci. USA* **1998,** *95,* 2256-2261.

25 Bruno, A.E.; Baer, E.; Völkel, R.; Effenhauser, C.S. *Proceedings of the MicroTAS Workshop,* Kluwer Academic Publishers, **1998**, 281-285.

26 Fluri, K.; Fitzpatrick, G.; Chiem, N.; Harrison, D.J. *Anal. Chem.* **1996,** *68,* 4285-4290.

27 Seiler, K.; Fan, Z.H.; Fluri, K.; Harrison, D.J. *Anal. Chem.* **1994,** *66,* 3485-3491.

28 *Handbook of Capillary Electrophoresis* , Editor, Landers, J.P., CRC Press, Boca Raton, 1996.

29 Ezan, E.; Tiberghien, C.; Dray, F. *Clin. Chem.* **1991**, *37*, 226-230.

# Chapter 5

# Design and Evaluation of Serial Dilution Component for Microfluidic Devices

## 5.1 Introduction

Many samples in their original form are too concentrated and must be diluted before being properly analyzed. Examples include the analysis of dissolved ore samples by flow injection methods, and immunoassays for drugs, where the antibody affinity constant is so large that samples require dilution to avoid saturation. Typically, the dilution factor for immunoassay is in the range of 50 to 1000. In microchip based systems, mixing and dilution of sample and reagent can be controlled by electrokinetic pumping in a valveless, integrated network of intersecting capillaries. Previous studies have demonstrated that dilution can be performed by varying the ratio of voltages applied to sample and buffer reservoirs, to give the desired dilution factor at the mixing intersection.[1] However, accurately performing the large dilution factors needed for immunoassays using electrokinetic pumping forces presents an almost impossible challenge for a single stage diluter.

Ramsey and co-workers have presented a study of parallel and serial mixing devices.[2] In those devices a one step dilution with a 0.16 sample fraction (dilution factor of 6.25) exhibited a 19 % deviation from the expected value, while a serial dilution with a 0.052 sample fraction (dilution factor 19.2) showed a 13 % deviation. Although encouraging, the largest dilution factor demonstrated in their studies is still not adequate for that typically required by many immunoassay experiments. In this chapter we report on devices capable of performing dilution factors of 32, 64 and 1024. The usefulness and performance of multi-step serial dilution devices are compared to single step dilution design.

## 5.2 Theory of multi-step dilution

The study by Jacobsen et al[2] illustrates that solvent flow proportioning within microfluidic devices may be imprecisely controlled by electrokinetic pumping. As developed below, variations in flow rate from the nominal value lead to concentration

errors, and these become more extreme as the magnitude of the dilution becomes larger. An analysis of these errors, and of their contribution to diluter design considerations, suggests that multiple serial dilution steps offer advantages over a single dilution step. However, in order to evaluate the errors, we must first obtain an understanding and an estimate of the magnitude of error that occurs at each electrokinetically controlled junction.

We define leakage at a junction in an electrokinetically controlled device to be flow that is not prescribed by the applied electric fields. Experimental reports have indicated that leakage from a floating side channel arranged in a T configuration is often in the range of 1-3 %[3] of the linear flow rate in the electrokinetically mobilized main channel. The exact magnitude depends on channel cross sections and lengths, and on the surface charge within each channel, and more extensive leakage is possible. This leakage arises from hydrodynamic effects, such as the viscous drag of the moving stream on a stagnant stream at a junction. Computational fluid dynamics modeling of electrokinetic flow at a T-junction also indicate the leakage from the floating side channel is proportional to the velocity in the main channel for a given channel geometry.[4] Even when all channel potentials are controlled these effects are still present, adding to the net flow in the channels whenever the flow rate from the two feed channels is not identical. Even when the flow rates are set to be the same, corresponding to 1:1 mixing, errors in device fabrication, differences in surface potential between channels, or undetermined hydrodynamic junction effects may lead to deviation from the nominal mixing value. From junction to junction these latter effects may vary randomly, although they may represent a constant bias for any given junction. Below we refer to this "built-in" error of any junction as the junction error.

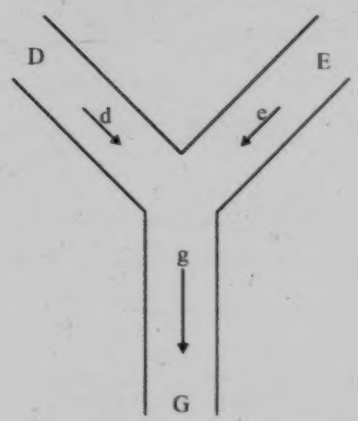


Figure 5.1 Schematic drawing of a Y mixing intersection. D, E and G are reservoirs and d, e and g are the volume flow rate in the channel.

Consider the intersection shown in Figure 5.1, to which voltages are applied between reservoirs D, E and G, such that solvent flows towards G, at volumetric flow rates d, e and g. Sample is taken to

be located in reservoir D, at a concentration $C_i$, and is mixed at the junction to produce a concentration $C_f$ downstream at G. The concentration can be expressed in terms of flow rates as,

$$C_f = C_i / F \tag{1}$$

where the nominal dilution factor, F, which has a junction error $\Delta F$, is given by,

$$F = g / d \tag{2}$$

Under conditions of extreme dilution the flow rate e will significantly exceed flow rate d, causing additional leakage of d at a flow rate of 1-3% of e. This same leakage will increase g, but the back pressure due to leakage at the junction will cause the flow rate e to decrease somewhat, resulting in g not increasing as much as d. Further, as the potential on D increases and d rises, the magnitude of difference between d and e will decrease, causing reduced viscous drag, and less leakage.[5] When d and e are equal, the leakage rate should be essentially zero. This qualitative analysis is supported by fluid dynamics modeling by Hu et al.[4,5] We can express these biases relative to the nominal flow rate using

$$F_{bias} = [g + \beta(e-d)]/[d + \alpha(e-d)] \tag{3}$$

where $\alpha$ is the proportionality constant between leakage flow in the side channel and flow in the main channel when D is floating, and $\beta$ ($\beta < \alpha$) is the proportionality constant for the increase in flow downstream of the junction under the same conditions. A simple linear model has been used to describe the decrease in leakage as the flow rates become equal.[5] Substitution of equation 3 into 1, instead of equation 2, provides an estimate of the concentration bias introduced by leakage when the flow rates are far from equal. Added to this bias would be any errors arising from the junction error $\Delta F$.

A device made with a sequence of serial diluters, each designed to perform a 1:1 dilution, should produce a minimum concentration bias according to equation 3. However, the variations in device geometry between junctions would still introduce errors. For a series of n 1:1 diluters, each with the same random variations in F, the error in final concentration, $\Delta C_f$ is given by,

$$\Delta C_f / C_f = \sqrt{n}\Delta F / F \tag{4}$$

Equation 4 assumes that errors in $C_i$ are negligible and the junction errors are random. This latter assumption will not be true for a given junction, but should be true for a random ensemble of junctions, such as those assembled in a multi-step diluter. The error is increased because of the number of junctions, but the lack of bias due to leakage should be a significant benefit of the multi-step design.

As an example to evaluate the magnitude of the biases that may occur, consider the case where $\alpha = 0.02$, $\beta = 0.01$, and $\Delta F/F = 0.02$. For a dilution factor F of 32 (d= 1, e = 31), equation 1 and 3 predict a 59 % bias to higher concentration, corresponding to a dilution factor of 20.2. A further ± 2 % error would be observed due to junction errors. In contrast,[6] for a 5-step, 1:1 diluter, propagation of the junction errors gives an RSD for the concentration of ± 4.5 %. For a dilution factor of 1024, performed in ten 1:1 dilution steps, the estimated RSD is 6.3 %. A single step dilution with d = 1 and e = 1023 would give a concentration bias of 21.2 times larger than the nominal value.

The model above is based upon a combination of experimental observation[1] and the prediction of models that successfully describe leakage at junctions.[4,5] We anticipate that it provides guidance as to the improved performance of serial diluters compared to single step diluters. However, since the model does not describe all leakage phenomena that have been observed[6] we do not expect this description to be quantitatively accurate.

We define the calculated concentration error as combined errors due to hydrodynamically induced leakage and junction error. In the case of 1:1 mixing, dilution error consists of only the junction error. We also define the observed variations in experimental data as the relative standard deviation (RSD). Finally, we will describe the difference between the nominal and observed dilution factor as the deviation.

## 5.3 Experimental

Devices were fabricated in 4x4 inch square, 600 µm thick Corning 0211 glass by the Alberta Microelectronics Center, as previously described.[3] Channels were 30 µm wide and 10 µm deep in devices shown in Figure 5.2, D32 and D1024. Channels in device D64 were 10.5 µm deep. The width of each of the diluting arms was 188, 84, and 33 µm, as indicated in the exploded view of Figure 5.3. Each of the diluting arms was connected to a 600 µm wide and approximately 1 cm long channel to the reservoir. Channels in

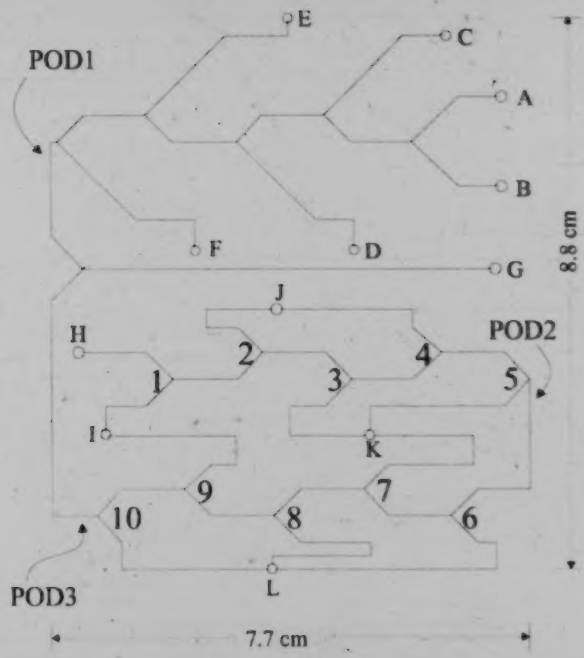


Figure 5.2 Two diluters integrated on a single wafer. The branched device on the top half is D32 while the more complicated device on the bottom half is D1024. The circles with alphabet labeling symbolize reagent reservoirs and the numeric characters label the intersections of D1024. Point of detection (POD) for various experiments were indicated. All channels were 10 μm deep and 30 μm wide. The overall dimension of the device is 7.7 cm x 8.8 cm. The shortest channel segment between reservoir H and intersection 1 is 1.6 cm.

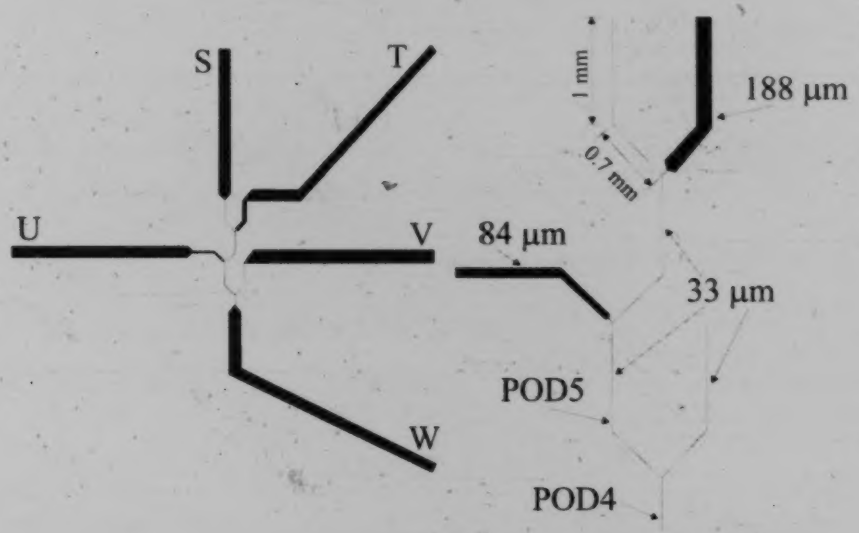


Figure 5.3 Diluter D64 with channel widths indicated in the exploded view. S, T, U and W represent reservoirs, and the location of the PMT is indicated as PODs. All channels were 10.5 μm deep. All the diluting arms contain the same length of channel segments, namely the1 mm and 0.7 mm, as indicated in the expanded view. The wide channels connecting the device to the reservoirs were 600 μm wide and ~1 cm long. The overall device, not including these wide channels, was ~ 3 mm x 5 mm.

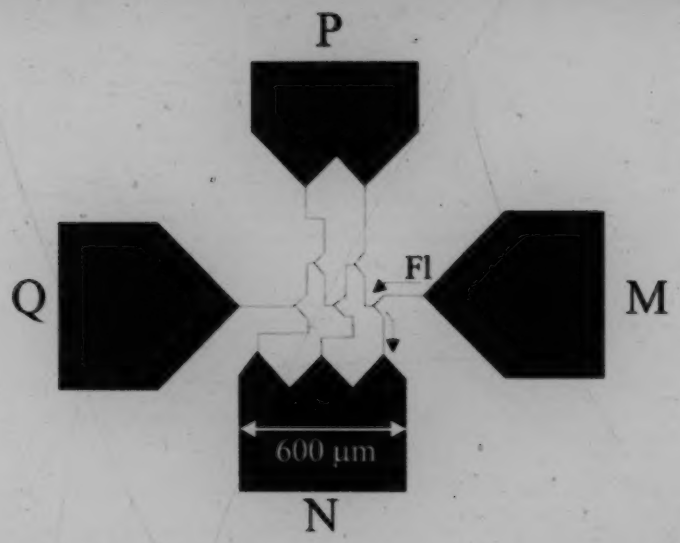


Figure 5.4 Expanded view showing the diluter D32S. The four wide channels extended approximately 1 cm to reservoirs labeled M, N, P and Q. All the narrow channels were 10 µm deep and 30 µm wide. The channels connecting the device to its respective reservoirs were 600 µm wide and extended approximately 1 cm long to the reservoirs. The whole device occupies less than 1 $mm^2$ area as indicated by the scale of the wide channel. Fluorescein sample was placed in reservoir M and buffer in all other reservoirs. Voltages of 200 V were applied to reservoirs M to P while reservoir Q was held at ground. Assuming voltage drop across the 600 µm wide channels are minimal, this applied voltage correspond to field strength of 1.7 kV/cm between reservoirs M and Q. Arrows indicate the observed flow direction of Fl sample placed in reservoir M when driven by electrokinetic forces as described in section 5.4.6 of text.

device D32S as shown in Figure 5.4 were 10 µm deep and 30 µm wide. Similar to D64, channels 600 µm wide and ~1 cm long were used to connect the reservoirs to the device. Top plates, into which 2 mm access holes were drilled, were vigorously cleaned[7] then thermally bonded to the etched plate at 600 °C for 6 hours, using the temperature ramp described previously.[8]

The buffer used primarily was a pH 8.5 Tris/Boric buffer made up of 50 mM boric acid and 50 mM tris(hydroxymethyl)aminomethane (Tris). In the ionic strength studies, the 50 mM Tris/Boric buffer was diluted to either 25 mM or 12.5 mM. Other buffer systems used in the ionic strength studies included 50 mM Tris/Boric with 10 mM KCl, and 25 mM Tris/Boric with 5 mM KCl. A 10 mM borate buffer was also used, which was adjusted to pH 8.2 with 1 M NaOH with 0.01% v/v Tween 20 (Aldrich, Mississauga, ON) added. Fluorescein (Fl) was from Sigma (Mississauga, ON). All solutions were prepared using ultra pure water (Millipore Canada, Mississauga, ON), and were filtered with 0.2 µm Nylon-66 membrane filters (Fisher, Edmonton, AB).

The computer controlled power supply and relay arrangement has been described previously, as well as the 488 nm argon ion laser source and detection system.[3] SPICE simulation was performed using DesignLab Evaluation Version 8 from MicroSim Corporation (Irvine, CA). Finite element simulations were performed using FlumeCAD version 4.8 from Coventor Technologies (Cambridge, MA).

## 5.4 Results and Discussion

There are two primary methods of varying the mixing ratio in an electrokinetically driven microfluidic device: namely the use of variable voltages to control the magnitude of dilution at each intersection, or the use of geometric control of flow resistance through the design of the channel dimensions.[1] Voltage controlled dilution, although allowing for flexible change of the dilution factor, typically requires the use of more power supplies and frequent voltage calibration. A geometrically controlled dilution device is easily designed through manipulating the length and/or the cross section of the mixing channels to obtain the desired overall dilution factor. However, the dilution factor cannot be changed once fabricated unless one makes changes in the voltages applied to each channel. For example, a dilution factor of 64 can be achieve with six steps of 1:1 dilution, three steps of 1:3 dilution, two steps of 1:7 dilution or a combination of 1:1, 1:3 and 1:7 dilution steps. The mixing ratio of 1:3 and 1:7 could be achieved by varying the length and/or cross sectional areas. We will first explore diluters we have named D32, D1024 and D32S, each of which exhibits a constant cross sectional area design. A preliminary evaluation of other mixing ratios will then be presented, based upon diluter D64.

Figure 5.2 illustrates the layout of two serial diluters named D32 and D1024, fabricated together on one wafer. D32, the branched structure covering the top half of Figure 5.2, was the simplest design. It performed five steps of 1:1 mixing to give an accumulated dilution factor of 32. It was designed to be large in order to allow observation at each mixing intersection. The bottom half of Figure 5.2 is the more complex device, D1024, which was designed with the added intention of reducing the number of access holes needed. With its ten 1:1 mixing intersections, D1024 can be used to perform dilution up to an accumulated factor of 1024. The diluter devices were

designed to operate with sample placed in reservoir A or H for D32 and D1024, respectively, and dilution buffer in all the other reservoirs. The application of positive high voltage from a single power supply to all reservoirs except G, which was held at ground potential (GND) caused dilution to proceed. Alternatively, a negative high voltage could be applied to reservoir G while all other reservoirs remain at GND. Similarly, device D64 shown in Figure 5.3, will require high voltages to be applied to reservoirs S, T, U and V while GND is applied at W. Although all the devices were designed with electrokinetic pumping in mind, they will still be operational under pressure driven flow since the geometrically controlled resistance works for both methods of pumping.

In order to evaluate the design and usefulness of the diluter devices, both relative and absolute methods of evaluating the dilution factors within each device were used. The relative method is typically performed by filling the device with buffer and then placing the same fluorescein (Fl) sample sequentially in each of the sample reservoirs, with high voltages applied to drive the solutions downstream to the point of detection (POD). This method will be referred to as the "individual reservoir method". For example, in the evaluation of D32, sample was first placed in reservoir A and the resulting signal was detected at POD1. Reservoir A was then replaced by buffer and the flushing step was also recorded. The process is then repeated for all the reservoirs. Alternately, the sample can be placed in all reservoirs simultaneously and the voltages are then applied. This method will be referred to as the "staircase method". The resulting

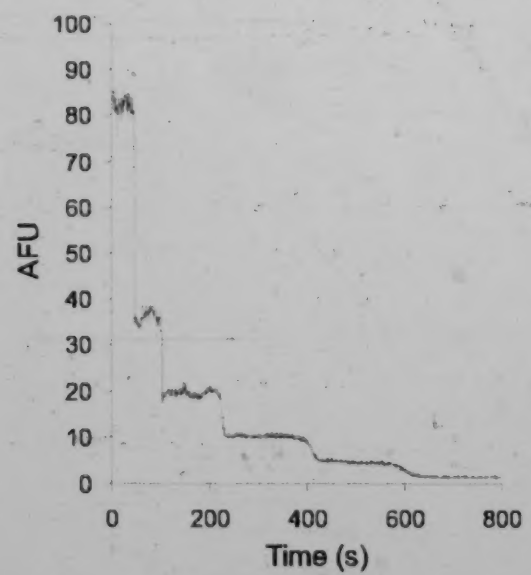


Figure 5.5 A "staircase buffer run" (see text) obtained when D32 was first filled with 5 nM fluorescein, and then all reservoirs were filled with 50 mM Tris/Boric buffer. Voltages of 9 kV were applied to reservoirs A to F and ground at reservoir G to drive the buffer into the diluter.

signal observed is an upward staircase trace as each reservoirs' contents reaches the POD (termed a "sample run"). A downward staircase trace, shown in Figure 5.5, was obtained when the contents of all the reservoirs were subsequently replaced with buffer (termed a "buffer run"). With the relative method, the signal for each observed dilution is ratioed to the lowest or highest concentration measured, in order to estimate the concentration change.

The absolute method of evaluating the diluter devices involves first constructing a calibration curve and then performing replicate dilution runs of a known concentration of sample. The dilution factor is then calculated for the sample using the calibration curve. The experimental dilution factor was then compared to the estimated dilution factor based upon the design of the device.

### 5.4.1 D32 device evaluation with relative method

For device D32, the "individual reservoir method" was used to evaluate the performance. A sample of 100 nM Fl was alternately placed in each reservoir with buffer in all the others. Voltages of 7 kV were applied to reservoirs A to F, while reservoir G was held at ground (GND). The PMT was located at POD1 as indicated in Figure 5.2. The final concentration of Fl at the detector is inversely proportional to the overall dilution factor. For example, when the 100 nM Fl sample is placed in reservoir D, the signal detected corresponds to an overall dilution factor of 8. The signal detected is directly proportional

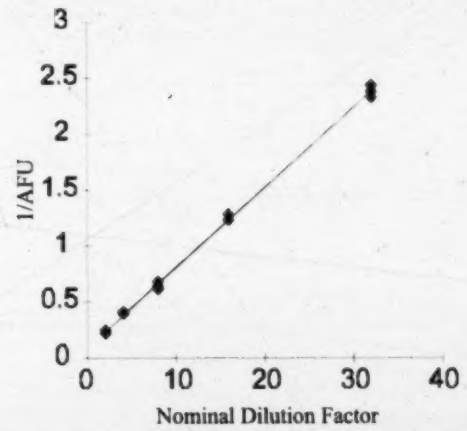


Figure 5.6 Plot of the inverse of arbitrary fluorescence units (1/AFU) versus dilution factor for D32, obtained using the "relative individual reservoir method" (refer to section 5.4.1 in text). 100 nM fluorescein sample and 50 mM Tris/Boric buffer were used. Voltages of 7 kV were applied to reservoirs A to F and ground at reservoir G. All three data points for each dilution factor were shown to indicate the reproducibility of replicate runs.

to $C_f$ and inversely proportional to F as indicated in equation 1. Figure 5.6 shows the inverse of signal detected at POD1 versus the nominal dilution factor for each of the possible dilution factors (assuming each intersection performed a 1:1 dilution). The good linearity indicates the diluter works as designed. The average RSD of signal for 3 replicate runs for each dilution factor measured is ± 2.4 %, indicating good dilution performance from the D32 design. Equation 1 can be expressed as

$$C_f = C_i/x^n \qquad (5)$$

where x is the average dilution factor of each intersection (nominally 2), and n is the number of dilution intersections. A plot of log signal versus n has a slope of –log x, and gave a value of 1.80 ± 0.02 for x. The total dilution factor for the design was thus 18.9 ± 0.5. Table 5.1 compares the average signal obtained for each of the dilution stages. The number appearing on the diagonal indicates the ratio of signal between any two adjacent intersections, providing individual experimental dilution factors. These ratios indicate that intersection 3 differed significantly from the others, all of which diluted with a factor around 1.9. The lower than expected dilution factor of 1.9 could result from a greater than 2 % junction error due to leakage at each intersection. For example, a 5 % junction error will cause x to be 1.90. Intersection 3 failed to dilute to the proper factor, significantly affecting the overall dilution. This is perhaps due to a partially plugged channel or to a significant difference in surface charge and electroosmotic flow rate in that channel. Nevertheless, the single serial step diluter can be seen to be less sensitive to poor behavior in one channel than a single stage diluter would be.

| Intersection Number | | | 1 | 2 | 3 | 4 |
|---|---|---|---|---|---|---|
| | Dilution Factor | | 2 | 4 | 8 | 16 |
| | | Average AFU | | | | |
| 1 | 2 | 4.70 | | | | |
| 2 | 4 | 2.51 | 1.87 | | | |
| 3 | 8 | 1.57 | | 1.60 | | |
| 4 | 16 | 0.80 | | | 1.95 | |
| 5 | 32 | 0.42 | | | | 1.91 |

Table 5.1 Comparison of the average signal obtained for each of the dilution stages. The numbers listed on the diagonal indicate the ratio of signal between that particular intersection and the signal level from the intersection immediately prior to it.

### 5.4.2 SPICE modeling and simulation

Previous studies have shown that the resistances of the channels of a microchip are proportional to the equivalent length of the channels.[1] The current flowing through each channel should be proportional to the flow in the channel, to a first approximation. In both D32 and D1024 designs, all of the channel's cross-sectional areas were kept constant, so that the only parameter available to control the resistance, and hence the mixing ratio at each intersection, is the length of each mixing channel. The diluter devices can be modeled as a network of parallel and serial resistors to evaluate the potential drop using SPICE simulation software. The channel length to cross-sectional area ratio is proportional to resistance,

$$R/\rho = l/A \qquad (6)$$

Where R is the resistance, l is the length in μm, A is the area in $\mu m^2$ and ρ is the solution resistivity in units of Ω·μm. When ρ is a constant in all channels we can use units of R/ρ in an impedance model of the flow channel circuit, and the resulting "current" will be in units of I·ρ,

$$V = I \cdot \rho \cdot R/\rho \qquad (7)$$

Inputting the ratio l/A as the lumped element model of a given channel segment resistance into a SPICE model of the fluid network gives I·ρ and the voltage at each junction as a result. The flow behavior of each device should be proportional to I·ρ so long as flow is controlled exclusively by electrokinetic forces. The ratio of currents is equal to the ratio of flow from each channel at an intersection, and thus the SPICE evaluated ratio should predict the dilution factors to a first approximation. This approach is particularly useful for understanding the flow behavior of device D1024, in which the resistor network is more complex, as shown by the circuit model in Figure 5.7. The modeling results are presented in Table 5.2 and 5.3. The l/A values for each channel segment were normalized to 1 kΩ for a 16 mm segment length. All other lengths are expressed as a resistance proportional to that length ratio. Since all channels have the same cross-sectional area for D1024 the resistances were input as the normalized length of channel in μm, so the current values in Table 5.3 thus have units of V·μm. Table 5.2 reports the estimated potentials at each intersection within the D1024 device, when 9 kV

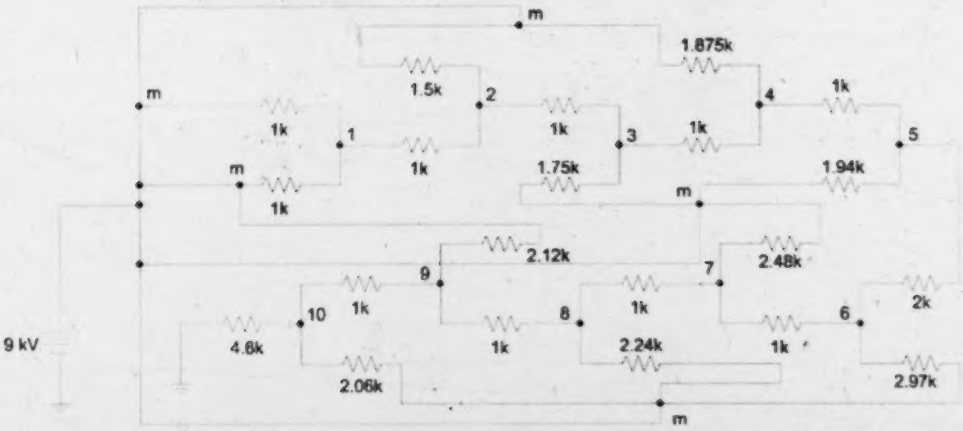


Figure 5.7 A network of parallel and serial resistors making up the equivalent circuit of diluter D1024. The value of each resistor is proportional to the length of the equivalent channel segment (16 mm of channel length is represented by 1 kΩ of resistance). The nodes indicated match the intersection numbering scheme in Figure 5.1. Connections between wires are indicated by dots.

| Node | Voltage | Node | Voltage |
|---|---|---|---|
| 1 | 8998 | 6 | 8852 |
| 2 | 8995 | 7 | 8752 |
| 3 | 8989 | 8 | 8552 |
| 4 | 8977 | 9 | 8152 |
| 5 | 8952 | 10 | 7353 |

Table 5.2 List of the SPICE simulated voltage at all the nodes as labeled in Figure 5.7.

| Current between Nodes (Refer to figure 5.6) per 1000 V applied | Relative current (V·μm) |
|---|---|
| m-1 | 0.95 |
| 1-2 | 1.89 |
| m-2 | 1.89 |
| 2-3 | 3.8 |
| m-3 | 3.79 |
| 3-4 | 7.59 |
| m-4 | 7.59 |
| 4-5 | 15.16 |
| m-5 | 15.16 |
| 5-6 | 30.33 |
| m-6 | 30.33 |
| 6-7 | 60.66 |
| m-6 | 60.66 |
| 7-8 | 121.33 |
| m-8 | 121.33 |
| 8-9 | 242.65 |
| m-9 | 242.65 |
| 9-10 | 485.31 |
| m-10 | 485.31 |

Table 5.3 Lists of current flowing through the channel segments represented by resistors in Figure 5.7.

was applied to the device. Table 5.3 lists the current flow through each resistor of the device, indicating that each intersection should give 1:1 mixing, even with the shared reservoir design used for this device.

In the case of D1024, using SPICE made clear a design flaw that prevented the diluter from working as it was intended. Experimentally, it was found that the time required for the sample to travel past the first few intersections was extremely long (several hours), so that the diluter was not practical. Table 5.2 clearly shows that this was due to the extremely small amount of driving force, only 2V, between the sample reservoir and the first intersection. In retrospect, it is clear that in order to perform a 1000X dilution, there must be a 1000 times voltage difference. For such a high dilution factor, the process must be broken up into sequential steps, such that the voltage difference required is manageable.

### 5.4.3 Evaluation of Device D1024 using relative method

The relative dilution method was also used with the D1024 device, to evaluate not only the dilution factor of each intersection, but also the efficacy of the "minimum access hole" design concept used for its layout. Using the bottom set of five intersections (intersections 6 to 10) of D1024, a sample of 5 nM Fl was placed in reservoir L while dilution buffer filled all the others. Voltages of 9 kV were applied to all reservoirs except reservoir G, which was held at GND. A detector was placed a POD3 as indicated in Figure 5.2. This "staircase method" leads to only three dilution steps being observed, giving dilution factors of 2, 8 and 32. A plot of AFU versus 1/F showed a linear relationship with $R^2 = 0.9998$. A plot of log signal versus n gave an average dilution factor of $1.93 \pm 0.02$ (n = 4) for each of intersections 6 to 10 and an overall dilution factor of $26.8 \pm 0.6$ (n = 4). The difference between 1.93 and the nominal 2 indicates an average of 3.6 % deviation per intersection.

**Using top half of D1024**

500 nM, $x = 1.97 \pm 0.07$
400 nM, $x = 2.27 \pm 0.06$
300 nM, $x = 2.15 \pm 0.09$
200 nM, $x = 2.30 \pm 0.04$
100 nM, $x = 2.08 \pm 0.11$

**Using bottom half of D1024**

$x = 1.93 \pm 0.02$

Table 5.4 Lists of average dilution factor obtained for the top and bottom half of D1024. Fluorescein samples with various initial concentrations were used in the top half of D1024 and the corresponding average dilution factors obtained were listed.

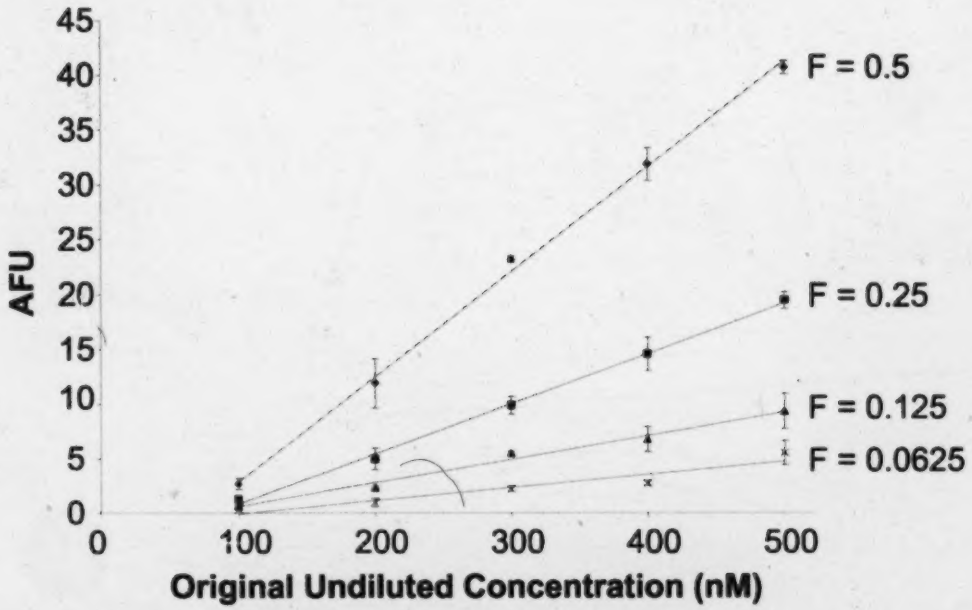


Figure 5.8 Plot of arbitrary fluorescence units (AFU) versus original concentration of fluorescein in the reservoirs. $R^2$ values are in the range of 0.998 for each line. Each vertical data set at a particular concentration corresponds to a single run using the "staircase relative method". The data was collected using the top half of D1024 with –10 kV applied to reservoir L, while reservoirs H to K were held at ground. 50 mM Tris/Boric buffer was used in this experiment.

The top set of 5 intersections of device D1024 was evaluated in a similar fashion, with a detector located at POD2. In addition, several samples of Fl were used to test the concentration dependence of the device. Table 5.4 lists the average dilution factor x obtained from the log signal versus n plot for intersections 1-5, evaluated using different concentrations of Fl. Those values range from 1.97 to 2.30 with relative standard deviations varying from 2 to 5 %. The average dilution factor was 2.15 ± 0.03. Figure 5.8 shows plots of AFU versus the original sample concentration for a series of dilution studies. Each vertical concentration line corresponds to a single "relative staircase method" study. The responses between each study are seen to scale linearly, however, an offset from the origin was observed. The linearity observed indicates that each of the intersections can reproducibly perform approximately 1:1 mixing and collectively gave the desired dilution factor regardless of the samples' concentration.

### 5.4.4 Evaluating D1024 with absolute method

Although the relative method gave a good indication of the performance of the diluter devices, an absolute method was needed to evaluate the accuracy of the dilution. Utilizing the top half of device D1024, a calibration curve was obtained by placing several different nM standard Fl solutions in reservoir K. A potential of 9 kV was applied to reservoir K with respect to reservoir L, while the other reservoirs were left floating, and the signal was detected at POD2. A 100 nM Fl solution was then placed in reservoir H, and dilution buffer in all the other reservoirs, in order to perform a dilution. Then 9 kV was applied to reservoirs H to K and GND to reservoir L, with the detector at POD2, performing a 32X dilution within the D1024 device. The result gave an overall dilution factor of 36.9 ± 0.5; 16% deviation from the nominal value of 32. The average dilution factor per intersection of 2.15, obtained from the relative method of evaluating the top half of diluter D1024, exhibits a 7 % junction error from the nominal dilution factor of 2. Based on this 7 % junction error, we can then propagate the error to find the range for the predicted dilution factor to be 32 ± 5. The experimental dilution factor is thus within the acceptable range of values for a diluter with a 7 % junction error. Further, the results of the relative method can be seen to be consistent with the results of the absolute calibration method.

SPICE simulations indicated that a dilution factor of 1024 is practically impossible to achieve in a continuous stream with the D1024 device. However, it is possible to perform the dilution in two stages. The first stage was performed in D1024's first five intersections, driving a sample placed in reservoir L to the channel section between intersection 5-6 and performing about a 32X dilution. This was then followed by the second stage, wherein the diluted sample was driven through the bottom set of five intersections to perform another 32X dilution, giving an overall dilution factor of 1024. Stage one was achieved by applying −11.5 kV at reservoir L while reservoirs H to K remained at GND for 800 s. It was then immediately followed by stage two, wherein the high voltage was switched to apply −10 kV at reservoir G and GND at all other reservoirs. The diluted Fl signal was detected at POD3 as indicated in Figure 5.2. A 3-point calibration curve was prepared with nM Fl standards placed in reservoir L, −10 kV at reservoir G, and all other reservoirs at GND. The on-chip diluted sample gave an

overall dilution factor of 907 ± 37. We can use the average dilution factor of 1.93, representing 3.6 % junction error for intersections 1-5, and a dilution factor of 2.15, representing 7 % junction error, for intersections 6-10, in order to evaluate the range for the overall dilution factor of D1024. Error propagation gave the acceptable range as 1024 ± 180, which the experimental value falls within. In fact the observed value was within 11 % deviation from the nominal 1024 factor, and the relative standard deviation in the dilution factor for three replicate runs was 4 %. These results show that the integrated serial diluter can achieve a large dilution factor with reasonable precision and accuracy. The observed deviation of 11 % from the nominal dilution factor of 1024 indicated a junction error of about 3.5 %, about twice the value of 2 % we assumed in the initial modeling of the errors in serial dilutions.

### 5.4.5 Effects of ionic strength on dilution

Real samples are frequently present in a much different matrix than that of the dilution buffer. Since the diluter devices in this project utilize electrokinetic pumping to mix and dilute the sample, a qualitative study was conducted to evaluate the performance of the diluter when the sample matrix had a different ionic strength than that of the dilution buffer. The experiment was performed using the top half of D1024 (detection at POD2) by applying –9 kV at reservoir L and GND to reservoirs H to K. The experiment gave a two-step staircase trace corresponding to dilution factors of 2 and 8. Six samples of 10 nM Fl in various buffers of different ionic strength were alternately placed in reservoir K. All other reservoirs contained 25 mM Tris/Boric as the dilution buffer. Table 5.5 lists the various buffers used in preparing the Fl sample and Figure 5.9 shows the bar graph of observed fluorescence signal for all the samples. Sample B was diluted in the same buffer as the running buffer and thus serves as the standard for comparison. Results from Figure 5.9 indicate that samples A, C and E gave similar signal to that of sample B within experimental error, while samples D and F showed a signal level almost doubled that of sample B. Due to the ion paring effects, the percent dissociation of ions in Tris/Boric buffer is rather low. Consequently ionic strengths were similar, so the flow behaviour in the mixing intersections were similar to those obtained when sample was in the 25 mM Tris/Boric running buffer. However, when 5 to 10 mM KCl was added to

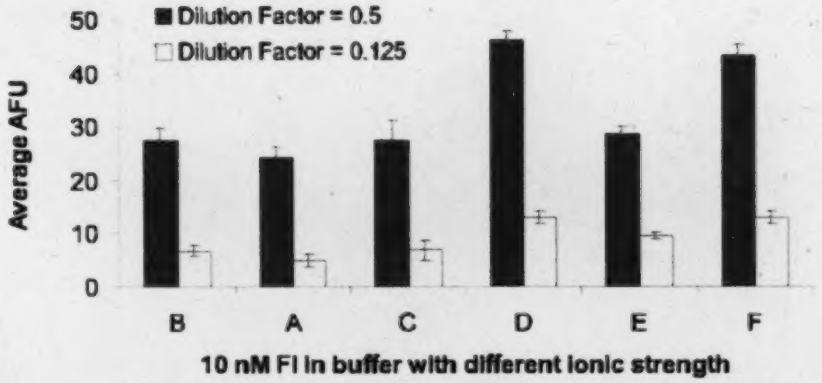


Figure 5.9 Bar chart showing fluorescence signal detected for six 10 nM Fl samples in different buffers. The letter code used for each buffer is identified in Table 5.5. The running buffer was 25 mM Tris/Boric buffer and the error bars indicate relative standard deviation for three replicate runs. Experiment was performed using the "staircase relative method" in the top half of D1024. Samples were alternatively placed in reservoir K and voltages of –9 kV applied to reservoir L while reservoirs H to K were held at ground.

| Sample | Description |
|---|---|
| A | 10 nM Fl in 50 mM Tris/Boric Buffer |
| B | 10 nM Fl in 25 mM Tris/Boric Buffer |
| C | 10 nM Fl in 12.5 mM Tris/Boric Buffer |
| D | 10 nM Fl in 50 mM Tris/Boric + 10 mM KCl Buffer |
| E | 10 nM Fl in 10 mM Borate with 0.01 % Tween 20 Buffer |
| F | 10 nM Fl in 25 mM Tris/Boric + 5 mM KCl Buffer |

Table 5.5 List of samples used in the test of effects of different ionic strength on dilution as described in section 5.4.5 of the text. Running buffer was 25 mM Tris/Boric buffer.

sample F and D, the amount injected was increased. Thus the signal detected for sample D and F were much higher, indicating less than 1:1 mixing at the dilution intersection. The results indicate that the diluter cannot tolerate much difference between the ionic strength of the sample and diluting buffer. This is not surprising, as it has been documented in the literature that dissimilar ionic strengths will cause unpredictable electroosmotic flow behavior.[6] We concluded that if the sample of interest is present in a matrix of different ionic strength than that of the dilution buffer, then at least the first step of dilution must be performed using pressure driven flow. It should be noted that the design of the D32 and D1024 diluters allows for either electrokinetic or pressure driven flow, since the constant cross sections mean that the length of the channels determines the resistance to flow for both methods of pumping.

### 5.4.6 D32S – A different method of "reservoir-sharing"

In the design of D1024, we have shown that connecting several different buffer channels to the same reservoir did not affect the diluter's ability to perform dilutions properly. Since the diluter is intended to be one of the many sample preparation steps integrated onto a microfluidic chip, the diluter will need to be smaller, so that in addition to occupying less wafer space, the speed of dilution can be reduced. However, as the size of diluter shrinks, the ease of connecting the small device to the macro world via independent fluid reservoirs decreases dramatically. Wide channels acting as delivering pipes to several channels simultaneously may be a way to address this problem. Figure 5.4 shows the close up view of a diluter design, D32S, occupying a region of merely 1 mm square. Four 600 μm wide, approximately 1 cm long channels were used to deliver sample and buffer to the diluter, each making connection to several of the buffer feed channels in the 1:1 diluter. Unfortunately, when the device was tested, it was found that the overall dilution factor was ~4.5, grossly deviating from the nominal value of 32. Further investigation revealed that when Fl sample was delivered into the diluter via reservoir M, the sample flowed out through the first diluting arm, as indicated by the arrows in Figure 5.4. This behaviour proved to be reproducible from day to day and chip to chip, and this flow was in the opposite direction to that intended. The point of application of the voltage at reservoir N was shifted closer to the narrow diluter channels by drilling a hole over the wide channel only 2 mm from the narrow channels. This change meant the Fl delivered from the sample reservoir M no longer flowed into the first buffer arm. However, the observed overall dilution factor of ~13 was still significantly different than that designed for. A larger design of D32S was also fabricated, in which all the narrow channels were ten times longer, and the device occupied a 5 x 5 $mm^2$ area. This larger device showed the same dilution factor and flow behaviour as D32S. This observation is consistent with the conclusion developed below that it was the contact channels that affected the performance, not the small dimensions used.

After the fact, we surmised that the unintended flow behaviour observed in D32S resulted from the use of common, large contact channels to connect several of the diluter channels together. We originally conceived of the contact channels as serving as

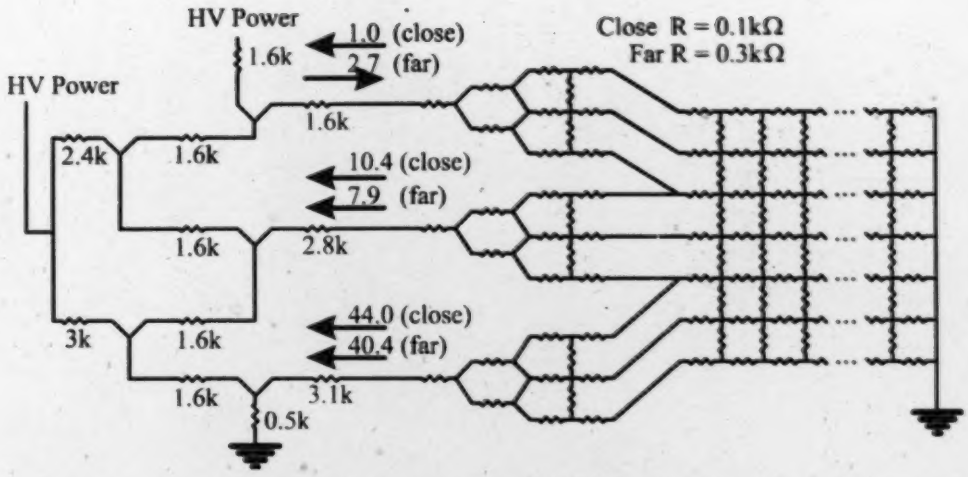


Figure 5.10 The diagram shows a circuit model of D32S with the wide channel connecting to reservoir N (refer to Figure 5.4) represented as a network of resistors. Resistor values of 0.3 kΩ were used to simulate placing the reservoir approximately 1 cm away from the narrow channels, and are denoted as "far". Each resistor value was changed to 0.1 kΩ to represent a reservoir located approximately 2 mm away from the narrow channels; denoted as "near". The arrows show the direction of current flow for both "near" and "far" simulation results, with the current magnitude indicated above the arrows. The model shows that current in the first buffer arm flows in the same direction as in experimental observation. When the length of wide channel at N is reduced by moving the voltage source closer to the diluter, the direction of current flow in the first buffer arm is reversed as was also observed experimentally (see Section 5.4.6 of the text).

electrical ground bus lines, sitting at a constant potential at any given cross section along the channel. This concept is equivalent to treating the contact channels as single lumped elements within an electrical impedance model of the device. However, electrolytes are fairly resistive conductors which can sustain potential differences across their cross section. This effect means the contact channels are better modeled as a network of small resistors, as illustrated in Figure 5.10 for one of the contact channels. The resistance used in Figure 5.10 is directly proportional to the length of each narrow channel segment, with an arbitrary proportionality constant of 8 Ω/μm for the lumped elements used to represent these segments. The values for the contact channel on the right were arbitrarily selected to be much smaller. The 1 cm long contact channel experiment was modeled with 160 contact resistor elements, each with a value of 0.3 kΩ. The direction of current flow is indicated by the arrow beside the word "far" in Figure 5.10. It can be seen that the current flow at the first dilution stage is in the opposite direction to that intended, consistent with the experimental observation. The 2 mm contact length was modeled by

reducing the network resistance in the contact channel to 0.1 kΩ. Figure 5.10 shows the currents for "close" contact are all in the originally intended direction, consistent again with experimental observations. The current flow into each diluter is not 1:1 even for the "close" model, which is consistent with the fact that D32S design never gave the intended dilution ratio.

FlumeCAD was used to verify the results obtained from SPICE. The device D32S was constructed as a finite element mesh with the exact physical channel dimensions. However, in the interest of computational time, only the wide arm connecting to reservoir N was included, and the other contacts were made directly at the end of the narrow channel segment. A coarse 2D extrude mesh of size 20 was first used for the simulation to ensure the parameters and boundary conditions were setup properly. A finer mesh size of 2 was then used to perform the final simulation result shown in Figure 5.11. The two results from different mesh sizes were qualitatively similar. Finer mesh size was not possible due to the limitation of our computer system. Figure 5.11 revealed that the potential at the first mixing intersection was higher than that at the first buffer arm, thus causing the flow to go in the opposite direction. This result is again consistent with experimental observation. The simulation gave an overall dilution factor of 4.1, compared to the experimental value of ~4.5. The difference between model and experimental is likely the result of the exclusion of the other wide channels in the simulation.

While D32S failed to provide the intended dilution ratio, the effort nevertheless revealed valuable insights. The first of these is that even when the large contact channels are significantly wider than the active, narrow channels, they are not readily approximated as ground plane busses in an impedance model. However, a networked resistance model, easily implemented in SPICE simulations, does provide a reasonable approximately of these wide channels' electrical characteristics. FlumeCAD simulation results agreed qualitatively with that of SPICE, indicating that either modeling method could prove useful for understanding the flow behavior within devices. The second result is that such small dimension diluters can be used to implement dilution, although quantitative assessment of their performance awaits the fabrication of a design that does not use the failed "ground bus plane" contact channel approach.

(a)

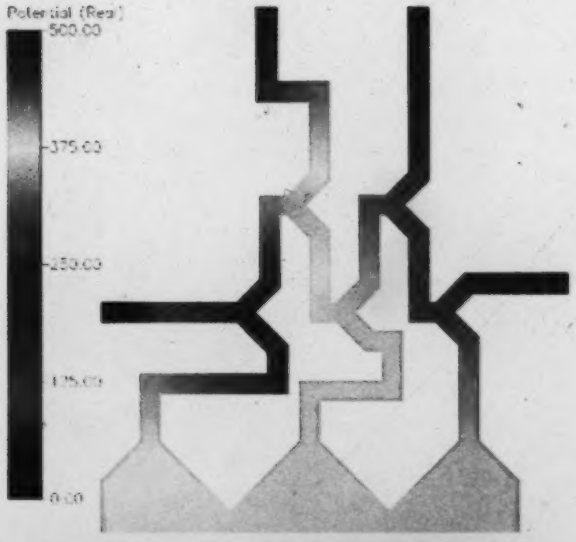


(b)

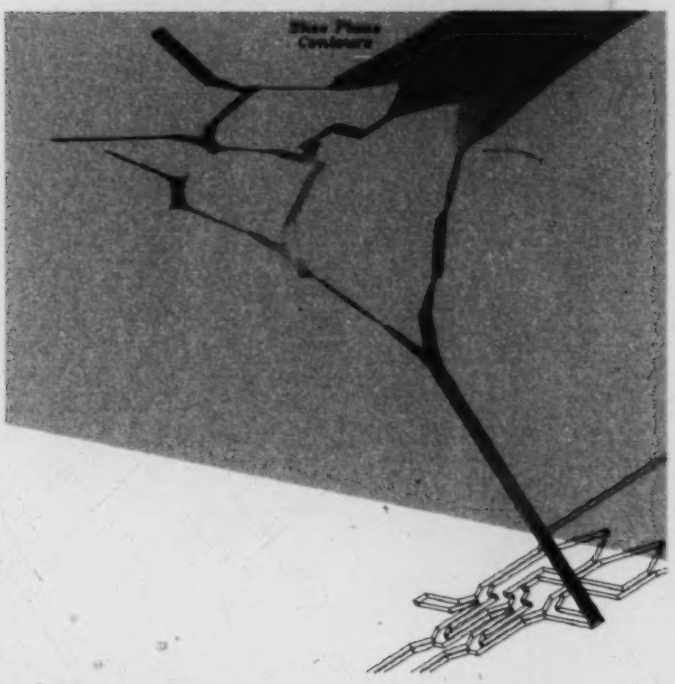

Figure 5.11 (a) FlumeCAD simulation results showing the potential drop in D32S. The narrow channels were 30 µm wide and the fat channel at the bottom was 600 µm wide and ~1 cm long. Other 600 µm wide channels were not included in the simulation (refer to Figure 5.4). 500 V was applied directly to reservoir each of the inlet arm, indicated by the red color and ground was applied at the outlet, indicated by the blue color. The potential at the first intersection (red) is larger than the 600 µm wide channel (orange) thus causing the flow of fluid into the wide channel as described in the text.

(b) The potential gradient diagram for D32S viewed as a 3-dimensional plot. The outline of the device is shown at the bottom right corner. The voltages are shown cascading down from the inlet to the outlet. Note that the channel connecting the first intersection to the wide channel has a downward slope indicating the voltage drop across that channel segment.

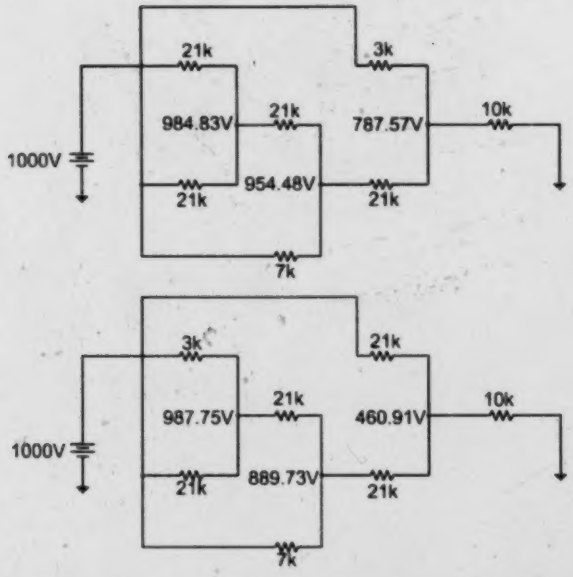


Figure 5.12 Two diluter circuits with different order of mixing steps. The top circuit diluted with the following sequence: 1:1, 1:3 and 1:7 while the bottom circuit diluted in the reverse order. The resistor values were arbitrary but the ratio of the resistor pairs gave the desired mixing ratio.

## 5.4.7 Preliminary study of varying cross section to vary dilution factor

### *5.4.7.1 Device Design*

In cases where design space and speed of performing dilution are more important than accuracy of the dilution factor, smaller devices with mixing ratios greater than 1:1 but less than 1:10 per intersection might be both desirable and functional. A set of three nominal dilution ratios, 1:7, 1:3 and 1:1 were combined together and tested in diluter D64. The layout is shown in Figure 5.3. Several issues, such as the order of the dilution steps needed to be addressed in the design of such a diluter. Figure 5.12 shows the equivalent circuit of D64 with two different arrangements. The simulated voltages at each node indicated that the configuration at the bottom was preferred, for it created a higher driving force at each intersection. We also decided to vary only the cross section of the channels and kept the lengths of each arm of the Y-shaped mixer pairs constant. The impedance and consequently, predicted flow rate through each channel was then controlled by the channel cross section. In order to calculate the mask widths required

for accurate cross sectional area after etching, we assumed the isotropic etch ratio was 1:1 and that the etched depth was 10 μm. By setting all the minimum channel mask widths to 10 μm, the calculated mask widths for the wider arm of the 1:3 and 1:7 mixers were 61 μm and 164 μm, respectively. These wider arms were tapered just before the Y intersections, to give a small segment ~120 μm long that matched the width of the other arm, as shown in Figure 5.3. This segment was intended to keep the channel cross section at each intersection constant, in order to give a constant surface area for any induced pressure forces to act upon and to keep leakage effects to a minimum. D64 occupied a region of 3 mm x 5 mm, although the overall dimensions were 1 inch square, in order to allow electrical contact via the individual long, 600 μm wide channels to the reservoirs. These 600 μm wide channels were considered very low resistance element and were neglected in the calculation of the resistance of the mixing channels of the diluter.

The final design of the device was modeled using SPICE with the equivalent circuit shown in Figure 5.13. The model predicted theoretical dilution factors for each intersection to be 5.8, 4.1 and 2.3, with an overall dilution factor for the device to be 55. These factors correspond to 1:4.8, 1:3.1 and 1:1.3 mixing ratios. These values differed from the originally intended values of 8, 4 and 2 due to the narrow ~120 μm long segment at the Y intersections, whose effect was neglected during the design phase. In addition, FlumeCAD simulation was performed for the structure and the resulting predicted dilution factors were in agreement with those obtained with SPICE using the lumped element model.

### *5.4.7.2 Evaluation of D64*

The dilution factor of each intersection was evaluated experimentally. By rearranging equation 1, we can express

$$F = C_f/C_i \qquad (8)$$

A calibration curve was obtained by placing various nM Fl standards in reservoir S to V, the detector at POD4, and applying 1 kV to those reservoirs, with GND at reservoir W. Assuming little voltage drop in the 600 μm wide channels, the electric field strength,

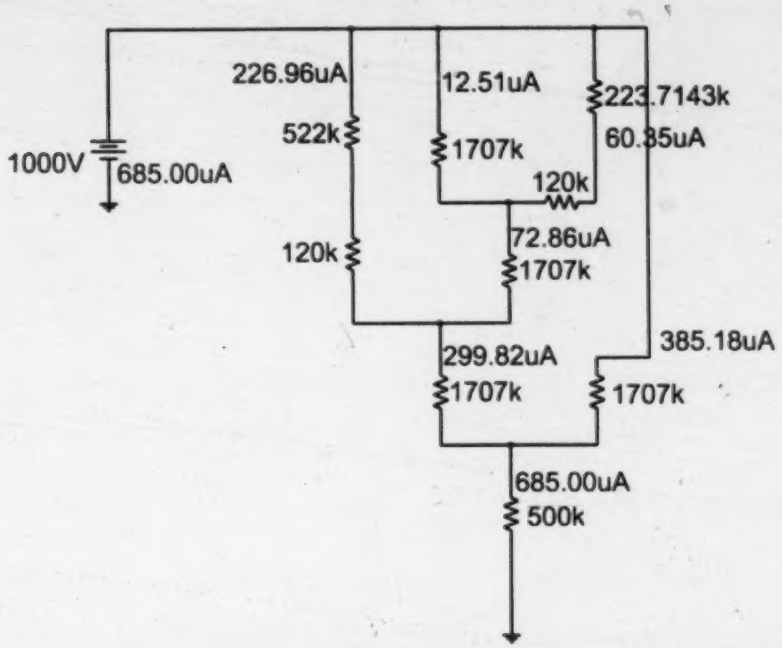


Figure 5.13 Equivalent circuit of diluter D64. Dilution factors calculated by the model for each intersection are 5.8, 4.1 and 2.3, which combined to give an overall dilution factor of 55. The resistances of each channel arm are input as the length ratio. The narrowest channel (33 μm) segments were entered as the length (1707 μm => 1707 kΩ) and the wider channels (84 and 188 μm) were entered as the ratio of channel length divided by its nominal area ratio to the 33 μm wide channel (for example, 223.7143 kΩ => 1566 μm/7 for the 1:4.8 dilution intersection).

based on 1 kV applied ranged from 1.8 kV/cm between reservoirs V and W to 4.5 kV/cm between reservoirs S and W. The nM Fl standards were then alternately placed in reservoir V, with buffer in all other reservoirs. This method is essentially the same as the "individual reservoir method" described earlier; however, several concentrations of Fl and only one reservoir was involved in this study. The signals detected were converted to concentrations using the calibration curve and the diluted concentration was plotted versus the original concentration, as shown in Figure 5.14 for the 1:1.3 dilution step. The inverse of the slope of the line corresponded to the dilution factor for the intersection linked to reservoir V. The dilution factor obtained in this case was 2.10 ± 0.01, a 9 % deviation from the theoretical value of 2.3. The other two intersections, with different cross sectional areas, were evaluated simultaneously, using the same method as above but a simpler procedure with one Fl standard. A 5 nM Fl standard was placed in reservoirs S, T and U, with detection at POD5 and 1.5 kV applied to reservoirs S through V and GND

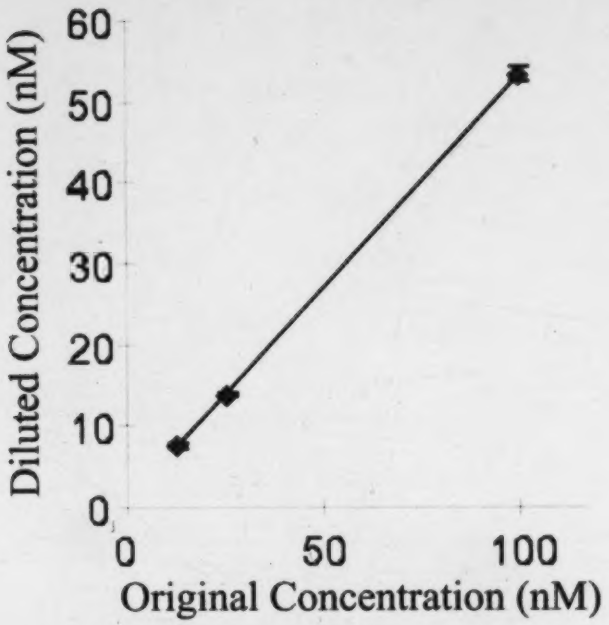


Figure 5.14 Plot of diluted Fl concentration versus the original Fl concentration for the 1:1 mixing step in diluter D64. Experiment was performed using a modified method based on the "relative individual reservoir method" as described in details in the text, section 5.4.7.2.

at W. This applied voltage corresponds to electric field strengths ranged from 2.7 kV/cm between reservoirs S and W to 6.8 kV/cm between reservoir V and W. This step provided the detector signal for the 5 nM Fl standard. The Fl standard was then alternately placed in only U, both S and T, only S or only T. Fluorescence signals obtained were plotted against the inverse of the corresponding theoretical dilution factor, as shown in Figure 5.15. The linearity of the plot indicated that the device performed satisfactorily. Further examination revealed that two of the lowest 1/F points deviated slightly from linearity, which translated to a rather large error in F, as indicated in Table 5.6 and 5.7. Table 5.6 lists the ratio of AFU of diluted Fl to that of the original undiluted Fl solutions. These experimental ratios are listed in the table along with the nominal values of 1/F. Table 5.7 summarizes the dilution factor of each mixing intersection for the diluter D64. The results show that for the dilution stages that nominally give a factor of 2.3 and 4.0 the experimental values matched within experimental error. Assuming a constant error per intersection of 7 %, we can expect the first 1:4.8 dilution intersection to contribute 34 % of overall error and the whole device involving all three dilution steps

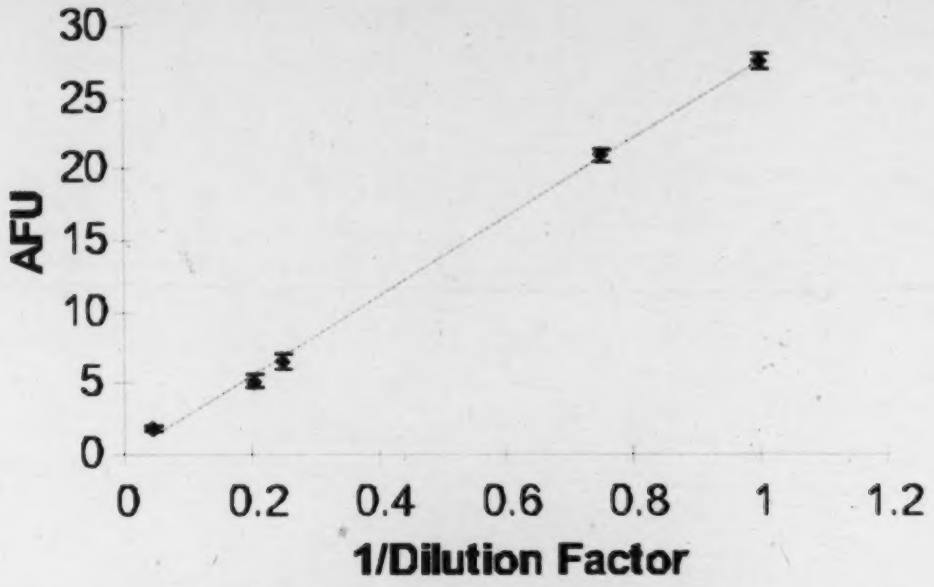


Figure 5.15 Plot of arbitrary fluorescence units (AFU) versus the inverse of dilution factor (1/F) with $R^2 = 0.998$. Experiment was performed as described in section 5.4.7.2 of the text.

| 1/F | Average AFU | Ratio of AFU to AFU initial |
|---|---|---|
| initial | 27.5 ± 0.6 | |
| 0.752 | 20.9 ± 0.4 | 0.76 ± 0.02 |
| 0.248 | 6.5 ± 0.5 | 0.24 ± 0.02 |
| 0.203 | 5.1 ± 0.5 | 0.19 ± 0.02 |
| 0.045 | 1.8 ± 0.2 | 0.065 ± 0.006 |

Table 5.6 Ratios of AFU for various dilution stages to AFU of the initial Fl sample. See section 5.3.7.2 in the text for detail discussion of the experiment performed.

| Theoretical Dilution Factor | Experimental Result |
|---|---|
| 2.3 | 2.10 ± 0.01 |
| 4.1 | 4.1 ± 0.4 |
| 5.8 | 4 ± 1 |

Table 5.7 Comparison of theoretical dilution factor and experimental results based on ratios obtained from Table 5.6.

will result in a propagated dilution error of 41 %. For the 1:4.8 diluter stage (5.8 dilution factor) the experimental value of 4 indicated a 31 % deviation from the intended design. This deviation suggests that dilution error at this particular intersection is within the expected range. Using profilometer and electron microscopy measurements of the width

(188 and 84 μm) and depth (10.5 μm) of the channels, we recalculated the ratio of cross-sectional area of the Y mixer arms and found that they were 1:2.9 and 1:6.5 instead of the intended 1:3 and 1:7, respectively. When these new dimensions were used in the SPICE lumped element simulation, the resulting dilution factors were 5.7, 4.0 and 2.3 compared to the original 5.8, 4.1 and 2.3, respectively. Unlike D32 and D1024, in which all the channel's cross-sectional areas are the same, the variable cross-sectional areas in diluter D64 make it more vulnerable to fabrication process variables, such as the etch depth and etch ratio, which may deviate from the intended values. The study of diluter D64 has led us to conclude that the 1:1.3 and 1:3.1 mixing intersections performed satisfactorily, while the 1:4.8 mixing intersection cannot be relied upon for an accurate dilution. In addition, the study showed that the small dimensions of the diluter D64 resulted in a much faster dilution, as shown in Figure 5.16 for the typical "staircase sample run" and "staircase buffer run". The dilution was completed in ~60 s compared to ~650 s for D32 results shown in Figure 5.5.

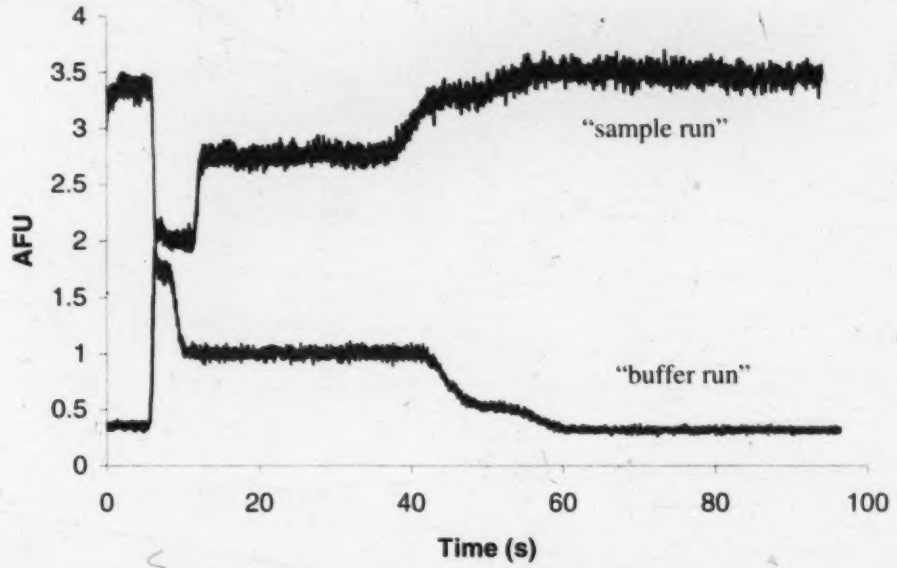


Figure 5.16 Plot of arbitrary fluorescence unit (AFU) versus time of a typical "buffer run" and a "sample run" performed using the "relative staircase method" in D64. 100 nM fluorescein sample and 50 mM Tris/Boric buffer were used to obtain the traces shown. Voltages of –3 kV were applied to reservoir W while reservoirs S to V were held at ground. The applied voltage gave field strengths ranged from 5.3 kV/cm between reservoirs S and W to 13.6 kV/cm between reservoirs V and W. Both traces indicated that dilution was completed in approximately 60 s.

## 5.5 Conclusions

This study has demonstrated that on-chip serial dilution to give a dilution factor as large as 1000 is possible, and that it can be performed with much better precision than with a single step dilution. SPICE simulation was found to be useful for modeling the diluter as a simple resistor circuit, such that a complex network design of channels can be analyzed prior to fabrication. However, for flow paths with multiple outlets such as D32S, a sheet resistor model or finite element simulation is needed for a more accurate description of the flow behaviour. The serial diluters presented in this study will provide foundation for another of the much needed sample preparation elements for a full μ-TAS device.

## 5.6 Reference


1. Seiler, K.; Fan, Z.H.; Fluri, K.; Harrison, D.J. *Anal. Chem.* **1994**, *66*, 3485-3491
2. Jacobson, S.C.; McKnight, T.E.; Ramsey, J.M. *Anal. Chem.* **1999**, *71*, 4455-4459
3. Fan, Z.H.; Harrison, D.J. *Anal. Chem.* **1994**, *66*, 177-184
4. Hu, L.; Harrison, D.J.; Masliyah, J.H. *J. Colloid Interface Sci.* **1999**, *215*, 300-312
5. Hu, L. *M.Sc. Thesis "Numerical model of electrokinetic flow"* **1997**, p. 94
6. Shultz-Lockyear, L.L.; Coyler, C.L.; Fan, Z.H.; Roy, K.I.; Harrison, D.J. *Electrophoresis* **1999**, *20*, 529-538
7. Chiem, N.H.; Harrison, D.J. *Clin. Chem.* **1998**, *44:3*, 591-598
8. Li, P.C.H.; Harrison, D.J. *Anal. Chem.* **1997**, *69*, 1564-1568

# Chapter 6
# Conclusions and Suggestions for Future Work

The purpose of this chapter is to summarize the main results from the previous chapters and to suggest further experiments and directions for the work presented. As stated in Chapter 1, the main objective of this work was to develop a multiplexed, automated Micro Total Analysis System (μTAS) using immunoassay (IA) as the vehicle.

One of the main challenges in μTAS is the detection scheme. The potential of integrating optical components with the fluidic channels for the purpose of multiplexing and further reducing the overall size of a μTAS is tremendous. In Chapter 2 we explored the use of an ion-exchange waveguide to guide an excitation source within a microfluidic chip. We successfully fabricated the ion exchange waveguide and used it to guide the laser source to the fluidic channel and excite the sample. However, the current method of waveguide fabrication and the specifics of the device design resulted in high propagation losses that ultimately made absorbance detection not possible in this work. Clearly, the waveguide fabrication needs more care to be applied. It takes good control over the physics and chemistry of the process to achieve consistently low loss waveguides with accurate dimensions and shape for matching to optical fibers,[1] and there are methods in the literature demonstrated to improve the losses of the waveguide.[2-4] This effort was not invested because we realized that the overall concept of including light pipes into the microfluidic chip might not offer as much advantage over the conventional lens and mirror setups as might be hoped. In fact, subsequent work by Salimi-Moosavi et al[5] in which a multireflection cell for enhanced absorbance detection was fabricated and used with conventional optics offered an easier solution. The main issue lies in that fact that we still cannot avoid some tedious alignment procedure in the coupling of the excitation source and the output light to and from the chip. The inclusion of translation stages, positioning equipment and some type of lens at some location within the overall optical system seems very hard to avoid. As a result, we concluded that integrated waveguides may not offer significant advantages for single flow manifold chips.

One possible future design for an absorbance detection scheme in microfluidic chips might be to fabricate a 3-dimensional device such as is illustrated in Figure 6.1. The detection method in this setup will be similar to those in conventional absorption spectrometry. The center layer of the 3-wafer stack will be micromachined with flow channels on both surfaces and a small diameter through-hole will be drilled to connect the channels on the top surface to those on the bottom surface, as illustrated in Figure 6.1. Any difficulty will lie in getting the through-hole to match the dimensions of the channels, so that separation efficiency is not compromised. Although 200 μm holes have been shown to be achievable on a routine basis,[6] those are still far too large when compared to the channels dimensions, which are typically 30-50 μm wide and 10-20 μm deep. Smaller through holes might be achieved in glass using 25 μm diameter drill bits from Minitool Inc. (Los Gatos, CA).

Corners or turns in separation channels represent a unique feature of microchip

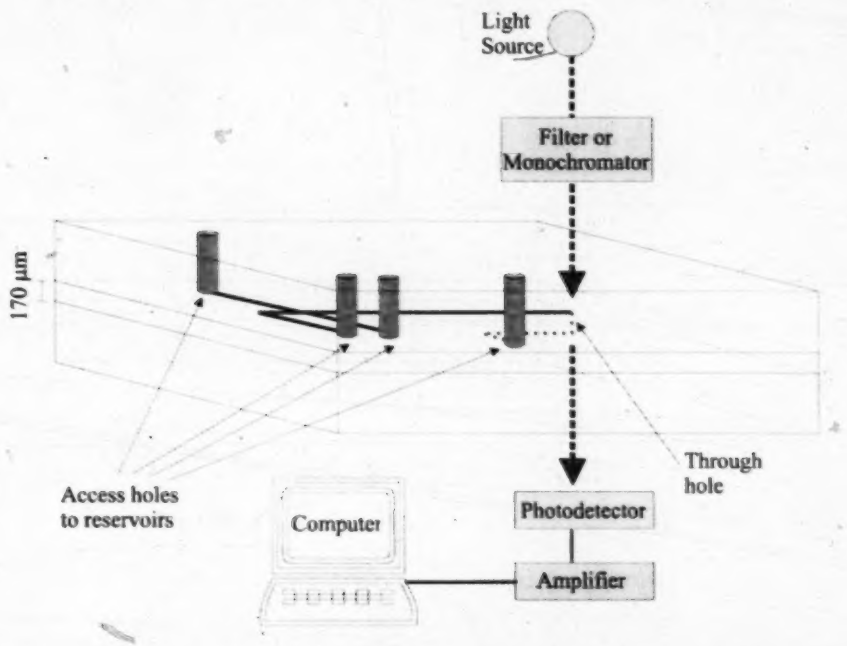


Figure 6.1 Cartoon of an absorbance detection scheme in microfluidic chip. The flow channels are fabricated on both the top and bottom surface of the glass substrate which is sandwiched between two cover plates. The channels on the two surfaces are connected by a small through hole drilled into the glass substrate. The light source is passed through the through hole that serves as the detection cell for the absorbance measurements.

based capillary electrophoresis (CE). Chapter 3 proposed a simple model based on Taylor dispersion and the empirical evaluation of some parameters in order to predict the effect of a corner on band broadening. The model's prediction agrees well with the experimental results. This model will be a useful tool for researchers in the field of microchip based CE to analyze the efficiency of separation and to estimate the band broadening contribution from corners. The experiments performed in Chapter 3 showed little band broadening effect due to corners when using a small molecule with a fairly high diffusion coefficient. However, the model predicted that band broadening will be more profound when the molecular diffusion coefficient is small, as in the case of DNA. Although corner induced band broadening has been observed in the case of DNA,[7] more experiments need to be performed in order to quantify the amount of such band broadening and compare it to the model's prediction so such studies will test the robustness of the model.

The lesson learned in Chapter 3 was applied in the design and layout of the multichannel device used in the work presented in Chapter 4. The work presented is the first demonstration of a fully integrated sample preparation and analyses device in which sample analysis is multiplexed. On-chip mixing, reaction, and separation for performing immunoassays were accomplished simultaneously in six separation sample manifolds within the device. The speed of analysis, including calibration and sample analysis was under 60 s, illustrating the power of multiplexing. Factors important for obtaining high quality, quantitative measurements within a multichannel device were identified. The work sets the foundation for future development of more complicated multichannel devices. More detailed conclusions are described in Section 4.4 of Chapter 4.

The scanning detector used in the multiplexed immunoassay study proved to be quite effective. It could have further applications in kinetic studies, allowing probing upstream and downstream of an event induced by some specific chip element. Future work for this project includes improvement of the detection design, improvement of the compactness and portability of the overall system, development of a more convenient sample introduction method and integration of other sample preparation components onto the device.

The detection design could be made such that no moving parts are involved, thus increasing the robustness of the system. A Dammann grating could be used in place of the galvo mirror, to split the laser beam into the desired number of spots so that all channels can be excited simultaneously.[8] In addition, the use of micro-optics[8-10] might further reduce the bulk of the current detection scheme. Alternatively, a more ambitious approach would be to integrate optical components such as a grating coupler, splitter and waveguides onto the multichannel microfluidic device. However, in light of the potential difficulties experienced in Chapter 2, it is this author's recommendation that such an undertaking should be attempted with the collaboration of a research group with more experience in integrated optics.

The bulk of the power supply interface could be reduced, thus making the whole "Lab-on-a-Chip" unit portable.[11] The coupling of the device to a more conventional microtitreplate will further allow the system to be automated. Finally, other components such as a diluter required for a specific IA need to be integrated so that less human involvement is needed. The design and performance of various diluters was demonstrated in Chapter 5. The work presented the first novel serial dilution device for μTAS applications. We have also demonstrated the largest on-chip dilution factor, up to 1000 times, with respectable accuracy and reproducibility. Future work will include integration of the diluter to other components, such as a filtering device, a mixer, reactor and separation column, so that a "real" sample can be introduced directly into the microchip without human manipulation. In addition, the diluter can be used as a routine self-calibration device for an automated instrument.

Clearly much more work is needed for the construction of a truly automated μTAS with high sample throughput. The work in this thesis has moved us one step closer to such a system. Although the IA was the focus goal for this thesis work, many components of it could be applicable to other applications.


1. Albert, J in *Introduction to Glass Integrated Optics*, Najafi, S.I. (Ed.), Artech House, Boston, 1992, pp. 8
2. Stewart, G.; Laybourn, P.J.R. *IEEE J. Quantum Electron.* **1978**, *QE-14*, 930-934

3. Ingenhoff, J.; Lefebvre, P.; Zhang, W.G.; Li, C.Y.; Roβ, L.; Najafi, S.I. *Proc. SPIE* **1994**, *2401*, 188-196
4. Findakly, T.; Garmire, E. *Appl. Phys. Lett.* **1980**, *37(10)*, 855-856
5. Salimi-Moosavi, H.; Jiang, Y.; Lester, L.; McKinnon, G.; Harrison, D.J. *Electrophoresis* **2000**, *21*, 1291-1299
6. Bings, N.H.; Wang, C.; Skinner, C.D.; Colyer, C.L.; Thibault, P.; Harrison, D.J. *Anal. Chem.* **1999**, *71*, 3292-3296
7. Paegel, B.M.; Hutt, L.D.; Simpson, P.C.; Mathies, R.A. *Anal. Chem.* **2000**, *72*, 3030-3037
8. Bruno, A.E.; Baer, E.; Völkel, R.; Effenhauser, C.S. *Proc. μTAS Workshop*, Kluwer Academic Publishers, **1998**, 281-285
9. Bruno, A.E.; Barnard, S.; Rouilly, M.; Waldner, A.; Berger, J.; Ehrat, M. *Anal. Chem.* **1997**, *69*, 507-513
10. Roulet, J.C.; Fluri, K.; Verpoorte, E.; Völkel, R.; Herzig, H.P.; de Rooik, N.F.; Dändliker, R. *Proc. μTAS Workshop*, Kluwer Academic Publishers, **1998**, 287-290
11. Lee, W.E.; Jemere, A.B.; Attiya, S.; Chiem, N.H.; Paulson, M.; Ahrend, J.; Burchett, G.; Bader, D.E.; Ning, Y.; Harrison, D.J. *J. Cap. Elec. aNd Microchip Tech.* **1999**, *006:1/2*, 51-59